Hydrogen Production in a Radio-Frequency Plasma Source Operating on Water Vapor

by

Son-Ca Viet Thi Nguyen

A dissertation submitted in partial fulfillment
of the requirements for the degree of
Doctor of Philosophy
(Aerospace Engineering)
in The University of Michigan
2009

Doctoral Committee:

Professor Alec D. Gallimore, Co-Chair
Associate Professor John E. Foster, Co-Chair
Professor Iain D. Boyd
Professor Ronald M. Gilgenbach

To my Mom and Dad,
Lam-Ngoc Thi Le and Truong-Son Viet Nguyen.
And in loving memory of my friend,
Mark de la Cruz Sarsoza.

Acknowledgements

This thesis would not have been possible without the support of my advisors, colleagues, friends, and family. I am humbled to have this opportunity to express my deepest gratitude for the guidance and encouragement that I have received over the years.

Foremost, I would like to thank my advisor, Dr. Alec Gallimore, for giving me the opportunity to fulfill my educational goal and the freedom to pursue my research interest. Dr. Gallimore allowed me to make my own mistakes and to learn from them, and he guided me in the right direction whenever I wandered off path. I value his advices, including those extended far beyond the subject of research. Without the support of Dr. Gallimore, this thesis simply would not have been possible. I owe my deepest gratitude to my mentor, Dr. John Foster, for many reasons: for introducing me to the field of plasma physics, for introducing me to Dr. Gallimore and encouraging me to pursue my doctoral work at the University of Michigan, and for our countless meetings where I always left learning something new. Our official mentorship ended many years ago after my internship at NASA concluded, but he has continued to serve as my mentor and role model throughout the years. I am forever indebted to him for his role in my education, and I thank him for showing me the humor in research, science, and life. I also wish to extend my warmest thanks to my other committee members, Dr. Iain Boyd and Dr. Ronald Gilgenbach, for reviewing my thesis.

From the aerospace engineering department, I wish to thank Cindy Enoch and Denise Phelps for sorting out my paperwork, and Thomas Griffin, David Mclean, and Eric Kirk for their help with my setup and in other numerous occasions. I thank Professor Bram van Leer for welcoming me to the department five years ago and continuing to be my confidant.

Research and collaboration are synonyms, and I would like to thank everyone at ElectroDynamic Applications, Inc. and the Hydrogen Energy Technology Laboratory for their collaboration and for loaning their equipment. I am also indebted to a number of agencies who have financially supported me: the National Science Foundation, Zonta International through the Amelia Earhart Fellowship, and the Gates Millenium Scholars Program. In addition, I am thankful for the many teaching opportunities that the Multicultural Engineering Programs Office offered me and in particular, I would like to thank Darryl Koch.

PEPL was a stimulating learning environment for me, mostly because I was surrounded by highly motivated colleagues who were always willing to help each other. In particular, I wish to acknowledge the following individuals for training me, for showing me the proper lab techniques and some short-cuts, and for their valuable input: Tim Smith, Joshua Rovey, Allen Victor, Jesse Linnell, Robert Lobbia, David Kirtley, Daniel Brown, Bryan Reid, and Kristina Lemmer. I am also very grateful to be in good company with Thomas Liu, Bailo Ngom, Ricky Tang, Rohit Shastry, Michael McDonald, Laura Spencer, Adam Shabshelowitz, Raymond Liang, David Huang, and Roland Florenz.

On a personal note, I would like to thank my friends, especially those I met in Ann Arbor, who have given me the necessary encouragement to finish my thesis and helped me achieve a balance between work and life through out my five years in graduate school. In particular, I would like to thank David, Caro, Serena, Cyril, Cecile, Jeff, Sebastien, Tosh, Tina, Kiran, Bryan, Arlyne, Nicolas, Andreja, Lisa, Mauricio, and Charleen. Above all, I would like to thank Pierre-Yves for his patience, humor, and kindness. Because of him, I am a much better person, and with him, life is more interesting and meaningful. I am fortunate to have him as a travel partner as we discover the world together. I would also like to extend my sincere thanks to Pilar, Mathieu, Jean-Philippe, and Marie-Christine for their encouragement. More importantly, I thank Pilar and Mathieu for bringing into this world the person with whom I am lucky to share my life. (En particulier, je souhaite remercier Pilar et Mathieu pour avoir mis au monde la personne avec qui j'ai la chance de partager ma vie.)

Lastly, I would like to thank my family for their continuous support: my parents, brother Vinh-Thinh, and sister Thu-Huong. Everything that I have accomplished was possible because of the opportunities that my parents have created for me through their sacrifices. The best way for me to express my gratitude to my parents is by repeating a Vietnamese proverb that I learned when I was a child, but only now understand its full meaning. It is loosely translated as: The work of a father is as significant as Mt. Thai Son, and the love of a mother is as bountiful as the spring water flowing from its source.

"Công cha như núi Thái Sơn,
Nghĩa mẹ như nước trong nguồn chảy ra."

Table of Contents

Chapter

Appendix

List of Figures

Figure

List of Tables

Table

List of Symbols

$\vec{a}$	Acceleration vector
a_{ij}	Stoichiometric coefficient of species i in reaction j
A_p	Surface area of the probe
A_s	Surface area of the sheath
D_i	Diffusivity of species i
$D_{a,i}$	Ambipolar diffusivity of species i
E	Electric field
E_A	Activation energy
$\vec{F}$	Force vector
f_{ij}	Returned fraction of species j as species i from the wall
H_j	Enthalpy of species j
k_j	Reaction rate coefficient for reaction j
L	Length of plasma discharge
M_i	Mass of species i
$\dot{m}$	Mass flow rate
N	Total number density
N_i	Number density of species i
n_e	Electron number density
n_i	Ion number density
P	Total pressure
p_i	Partial pressure of species i
P_d	Power deposited
R	Radius of plasma discharge
$\vec{r}$	Position vector
R_u	Universal gas constant
S_i	Reaction source term
T	Temperature
T_g	Gas temperature
T_e	Electron temperature

T_w	Wall temperature
t	Time
$\vec{V}$	Velocity vector
γ_j	Wall sticking coefficient of species j
$\gamma_s e$	Secondary electron emission coefficient
ϵ	Electron energy
κ	Thermal diffusivity
Λ	Diffusion length
λ_D	Debye length
ν_{mi}	Momentum transfer collision frequency between electrons and species i
σ	Electron impact cross section
τ	Mean time between collisions with neutral atoms
ω	Frequency of plasma oscillation

Physical Constants

k_B	Boltzmann constant, 1.3807×10^{-23} J/K
e, q	Charge of an electron, 1.6022×10^{-19} C
m_e	Mass of an electron, 9.1095×10^{-31} kg
ϵ_o	Permittivity of free space, 8.8542×10^{-12} F/m
μ_o	Permeability of free space, $4\pi \times 10^{-7}$ F/m
$\pi {a_o}^2$	Atomic cross section, 8.7974×10^{-21} m^2
N_A	Avogadro number (molecules/mole), 6.0220×10^{23}
R	Gas constant, 8.3144 J/(K mol)
AMU	Atomic mass unit, 1.6606×10^{-27} kg
T_o	Standard temperature, 298.15 K
P_o	Standard pressure, 1.0133×10^5 Pa

Acronyms

Btu	British thermal unit (1 Btu = 0.29 watthour)
CCP	Capacitively-coupled plasma
CF	Calibration factor
col	Collision
DC	Direct current
EEDF	Electron energy distribution function
ICP	Inductively-coupled plasma
HHV	Higher heating value

OECD	Organization for Economic Co-operation and Development
ppm	Part-per-million
RF	Radio-frequency

Chapter I

Introduction

1.1 Problem Statement

“Each day brings further evidence that the ways we use energy strengthen our adversaries and threaten our planet,” acknowledged President Barack Obama on the urgency and relevancy of the energy and climate challenges in his 2008 inaugural speech. All fossil fuels (natural gas, liquid petroleum, or solid coal) require hundreds of millions of years to form; hence, they are considered *non-renewable* natural resources when taking into account the relatively short time scale of the human race. Currently, the world relies on non-renewable fossil fuels to meet 85% of its energy demand [2] and the rate of world fuel consumption is expected to increase rapidly due to population and economic growth [3]. This summarizes the energy challenge.

At the same time, burning of fossil fuels introduces carbon dioxide gas (CO_2) into the atmosphere, raising the concentration of greenhouse gases. CO_2 is an essential by-product from combustion of fossil fuels, and its increasing concentration level has contributed to abnormal climate changes [1]. Consequently, the use of fossil fuels challenges the sustainability of our planet and the climate challenge is to reduce CO_2 emissions.

The energy and climate challenges are therefore deeply intertwined and they must be solved simultaneously. The increasing global energy demand and CO_2 emissions have motivated innovative techniques to satisfy demand while minimizing emissions. Many experts believe that the solutions to address the energy and climate challenges require a diversified portfolio of different methods, ranging from sequestration of CO_2 emissions to a variety of methods of alternative energy production. In the immediate future, fossil fuels will remain the main source of energy because of their availability and their high energy content. Consequently, additional emission of CO_2 is inevitable and some types of sequestration of CO_2 or other methods of CO_2 removal are necessary in addressing the climate challenge.

Ultimately, to address both the energy and climate challenges, humanity must be completely independent of fossil fuels. To date, there is not a perfect formula to address these intricate energy and climate issues. Nevertheless, the need to reduce consumption of fossil fuels and a transition into an economy less dependent on hydrocarbon is urgently necessary. On this quest to find alternative energy supplies, one solution is to use another secondary energy source other than electricity–hydrogen. As an energy carrier, hydrogen has the potential to address many aspects of the energy problem, particularly in the transportation sector. Hydrogen can be used in fuel cells or in combustion reactions.

One main attractive feature of hydrogen as an energy carrier is its potential to satisfy the need to fulfill some energy demand without further producing CO_2 emissions. But these energy and environmental benefits of hydrogen depend on how the gas is produced. If hydrogen is produced via renewable methods, those which neither emit CO_2 nor use current non-renewable resources (*e.g.* water), the potential benefits of hydrogen are realized. However, due to their high energy and conversion efficiencies, currently 95% of hydrogen produced in the United States is through steam-methane reforming, a non-renewable process [4]. Most of the other 5% of the hydrogen is produced primarily through conventional electrolysis. One main drawback with electrolysis is its requirement of a catalyst, which is often an expensive, rare resource such as platinum. Research is underway to find other and cheaper catalyst options to reduce the total cost, but it still remains an expensive option.

It is also argued that the widespread adoption of conventional electrolysis systems has a physical limitation. In these systems, hydrogen must diffuse in liquids, but their diffusion rate in a liquid is slower than their diffusion rate in a gas. As an alternative, hydrogen production via plasma electrolysis is investigated. However, many works in this area investigate the dissociation of liquid water [5–7], but the plasma processing of the liquid is localized in the region within the gas bubbles around the electrodes.

This work investigates a method of hydrogen production through the use of a high-density radio-frequency (RF) plasma source that operates in both capacitive and inductive modes to dissociate water vapor (as opposed to liquid water). Both experimental and computational works are carried out to assess the feasibility of this method. In addition to the main motivation, there are other needs for hydrogen gas and water plasma in general. For example, hydrogen is also needed in hydro-cracking, a process in which crude oil is mixed with hydrogen to produce many of the end-products that we use today, including gasoline [8]. Hydrogen is also used to produce chemicals such as ammonium and methanol [9] and to make hydrogenated oil [10].

In addition, the presence of energetic hydroxyl and oxygen in a water plasma offers many advantages in materials processing applications. Water plasma is being studied for a number of applications, including diamond film growth, ultraviolet light sources, and even medical applications [11–21]. A physical understanding of how a plasma source operates on water vapor offers insights into many areas of plasma chemistry research; yet, much of the plasma properties of a water vapor plasma have not been characterized. This work characterizes the properties of the water plasma, including electron density, ion density, electron temperature, floating potential, and plasma potential. The production of hydrogen is also quantified in this work. From these results, the main reaction mechanisms, especially dissociation mechanisms, in the water plasma source are identified. The experimental work in this dissertation is accompanied by a global kinetic simulation of the plasma discharge operating on water.

1.2 Aim of Project

The aim of this work is to evaluate the feasibility of hydrogen production through a method of dissociating water vapor in a RF plasma source. To reach this aim, the following steps are followed:

1. Generate a stable RF plasma discharge operating on water vapor. The main design of the plasma source–geometry of discharge, antenna configuration, and matching network design–follows closely with a similar setup from Professor Boswell's group at the Australian National University [22–24]. This RF plasma source was used

previously to simulate re-entry plasma conditions [25]. A water delivery system was designed to meter the amount of water injected into the chamber.

2. Develop diagnostic tools to characterize the water vapor plasma. The following diagnostics were used in this work: residual gas analyzer (RGA), Langmuir probe, and optical emission spectrometer. The RGA was used to identify the gas species in the plasma and to quantify hydrogen production. However, RGAs are designed to operate below 10^{-5} torr, much lower than the operating pressure of up to 500 mtorr in this experiment. A design of a differential pump system was required to operate the RGA. The Langmuir probe was used to characterize plasma properties. Finally, an optical emission spectrometer was used to identify species in excited states.
3. Apply a global kinetic model to simulate reaction kinetics and to study how dissociation of water molecules is affected by operating conditions including background pressure, RF power level, and water input flow rate.
4. Finally, with both experimental and theoretical results, infer the energy and conversion efficiencies of this method of hydrogen production, and provide directions for future work.

1.3 Thesis Outline

To achieve the aim discussed in the previous section, Chapter 2 begins with a description of the intertwined global energy and climate challenges. In this chapter, hydrogen is discussed as having a potential to satisfy some of the alternative energy needs. A survey of current conventional hydrogen production methods is listed. This survey shows that while the current methods of hydrogen production address some parts of the energy problems, they do not address the climate challenge. This leads to an overview of plasma. Chapter 3 first gives an overview of plasma physical processes in the water vapor discharge, and then lists the methods of plasma production and plasma sources. Finally, a literature review of water plasma studies and in particular hydrogen production methods from a plasma source is presented.

Chapter 4 shows the experimental setup and the diagnostics. The experimental setup section describes the main chamber, the water delivery system, and the radio-frequency plasma source. The diagnostics section describes the RGA, the Langmuir probe, and the spectrometer. Chapter 5 presents the experimental results. First, characterization of the plasma on argon is given and a comparison of plasma properties between an argon plasma and a water plasma is made. Electron density, ion density, electron temperature, plasma and floating potentials are characterized as functions of RF power, applied DC magnet current, and water vapor input flow rate. Lastly, hydrogen production is examined. In addition to experimental work, a global kinetic model, Global_Kin, is used to determine the theoretical energy efficiency as a function of water input mass flow rate and operating pressure in the regimes that are not currently experimentally accessible. Chapter 6 gives a description of this model and presents the computational results. Electron density and electron temperature are characterized, and the effects of water flow rate and background pressure on these two parameters are examined. Finally, conclusions on the feasibility of the proposed method are drawn in Chapter 7.

Chapter II

Background–Energy

The previous chapter summarizes the energy and climate challenges and motivates alternative energy research to address these problems. The aim of this chapter is to substantiate the energy and climate challenges by providing supporting evidence. In Section 2.1, a history and predictions of energy consumption and CO_2 emissions are presented. This section also explains the role of CO_2 in causing climate change. Section 2.2 outlines benefits and drawbacks of the proposed use of hydrogen to replace fossil fuels in the transportation sector. Section 2.3 lists current conventional hydrogen production methods.

2.1 Energy and Climate Challenges

2.1.1 Energy Challenge

The main cause of the energy problem is the world's dependency on fossil fuels as the primary energy source. All fossil fuels used today are formed from plants and animals that lived up to hundreds of millions of years ago, during the same time period when dinosaurs lived. The time span required to make fossil fuels therefore exceeds the relatively short time scale of the human race. As a result, fossil fuels are considered non-renewable natural

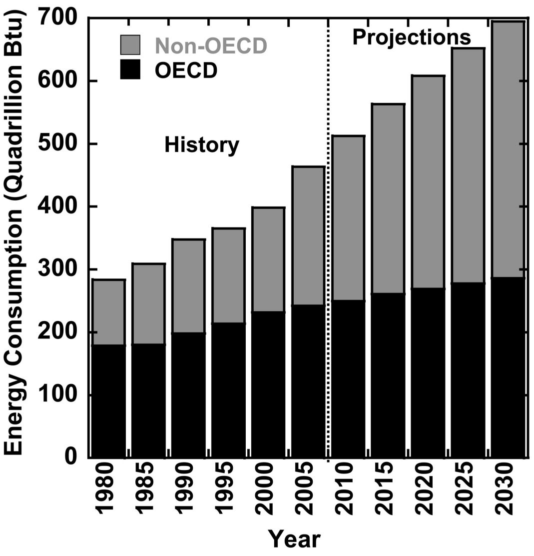

Figure 2.1: World energy consumption, 1980-2030 [2].

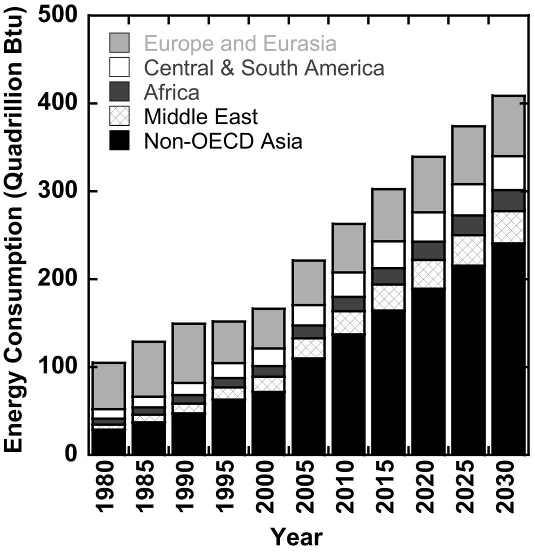

Figure 2.2: Total non-OECD energy consumption, 1980-2030 [2].

resources. On the other hand, economic growth and population increase necessitate an even higher energy demand in the future. The energy challenge is to address the future energy demand with limited supplies of fossil fuels.

Despite a limit in fossil fuel supplies, its demand is expected to grow. Even with a decrease in population growth rate in terms of percentages from 2% in the early 1960's to 1.2% in 2007, the world's population is estimated to reach over 9 billion in 2040 compared to 6.7 billion today [3]. Currently, 85% of the world's energy consumption comes from fossil fuels, and this dependency is expected to continue in the next several decades [2]. Figure 2.1 shows the total energy consumption from 1985 to 2005 and predictions up to 2030 in quadrillion (10^{15}) Btu per year (1 Btu = 1054 J) [2]. In 1980, the energy consumption was below 300 quadrillion Btu, but it is expected to reach 700 quadrillion Btu in 2030. These data substantiate the energy problem–the world continues to depend on non-renewable fossil fuel supplies.

In addition to population growth, economic growth also contributes to the increasing energy demand. In Figure 2.1, the histogram is divided into two groups: countries in the Organization for Economic Co-operation and Development (OECD) and those outside of OECD. The rate of energy consumption increase for non-OECD countries is much higher than that of OECD countries for the past several decades and this trend is expected to continue in the next several decades. Among those countries in the non-OECD group, India and China's predicted energy needs account for most of the energy demand increase. As shown in Figure 2.2, there is almost an indiscernible change in energy increase for non-OECD countries in the Middle East, Africa, Central America, South America, Europe and Eurasia. However, non-OECD Asian countries are predicted to double their energy consumption between now and the year 2030 [2]. As countries such as China are building more nuclear power plants, the future dependency on fossil fuels may reduce.

These predictions of significant increases in energy demand as shown in Figure 2.1 and Figure 2.2 will likely occur unless countries around the world drastically alter their energy consumption habits. However, primary energy sources still remain finite. Figures 2.3– 2.5 show proven reserves of oil, natural gas, and coal as of 2005 [26]. Even though finding more fossil fuel reserves is a possibility, the fact remains that fossil fuels are limited to finite quantities. This calls for urgent actions to reduce global energy consumption, to become less dependent on fossil fuels, and to find alternative sources of energy. These figures of proven reserves further illustrate an uneven distribution of current global energy supplies. The Middle East has most of the oil reserves and a large part of the natural gas reserves. Europe has a large share of the natural gas and coal. North America and Asia

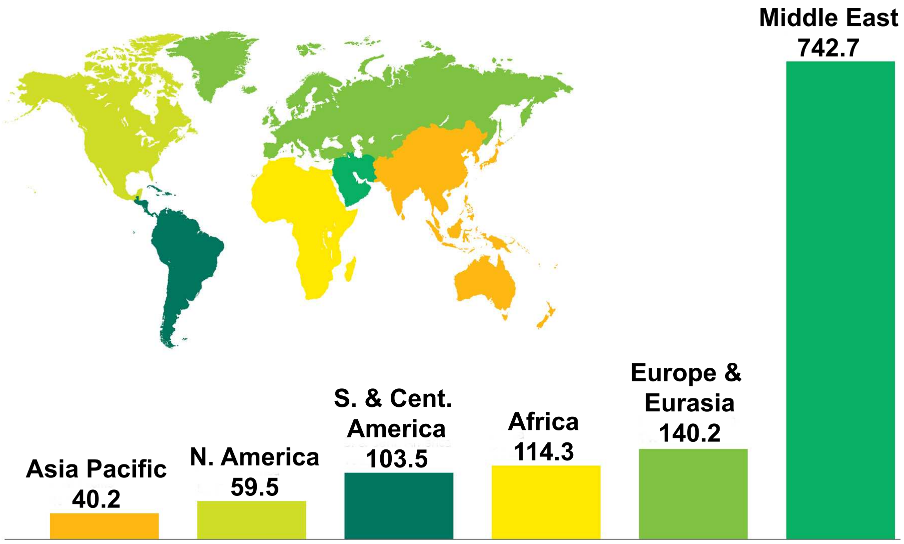

Figure 2.3: Distribution of proven reserves of oil at the end of 2005 in billion barrels [26].

Pacific has a large share of coal. For those countries that have direct access to reserves of fossil fuels from their own land mass or within their water boundary, finding alternative energy sources will ensure future energy security. For countries without a direct access to reserves of fossil fuels and therefore have to import them, finding alternative sources of energy has immediate economic and political benefits.

2.1.2 Climate Challenge

In addition to the energy challenge, the world also currently faces an equivalently grave problem–the climate challenge. There are still a few skeptics who attribute the recent observed global warming to the climate's natural cycle, but ample evidence has linked climate change to increased anthropogenic (man-made) CO_2 emissions. To understand this link, the greenhouse gas effect is examined.

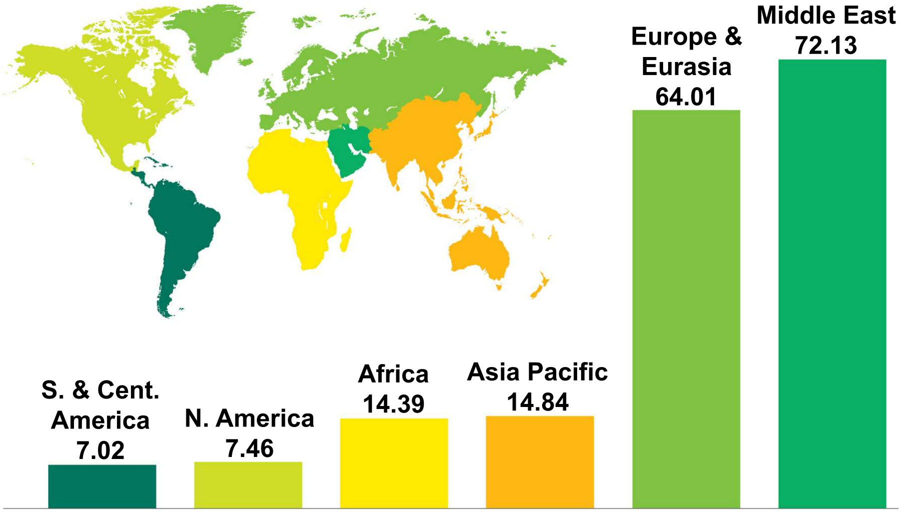

Figure 2.4: Distribution of proven reserves of natural gas at the end of 2005 in trillion cubic meters [26].

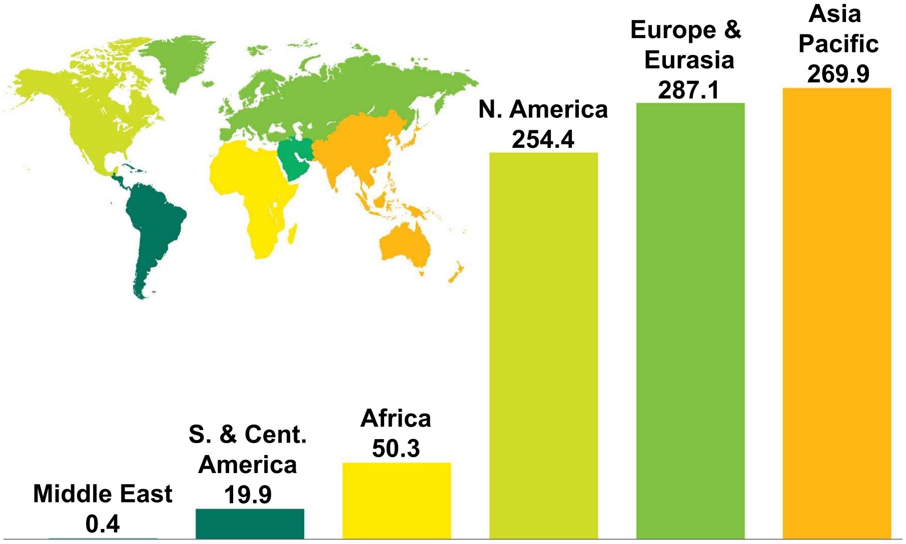

Figure 2.5: Distribution of proven reserves of coal at the end of 2005 in billion tons [26].

Earth can harbor human life because its temperature is between freezing and boiling point for water (its mean surface temperature is 287 K) [27], unlike Mars (186-268 K) [28] or Venus (729 K) [29]. The properties and the composition of Earth's atmosphere are different from its neighboring planets that allow human life to sustain. Earth's atmosphere uniquely acts as a blanket to retain some of the solar radiation through a natural greenhouse gas effect.

Figure 2.6 shows Kiehl and Trenberth's estimate of the energy balance [30]. Approximately 31% of the incoming solar radiation–mostly long wavelength in the infrared range–is reflected by clouds, aerosol, atmospheric gases, and the surface. The atmosphere absorbs 19% of the radiation and Earth's surface absorbs the rest of the 49% of the solar radiation, mostly short wavelength in the visible spectrum. Earth maintains an energy equilibrium by radiating infrared radiation. Without greenhouse gases, this radiation would be lost to space and Earth's temperature would be $\sim$ 30 K colder [31]. Therefore, greenhouse gases have a vital role in nature to maintain a comfortable range of temperature on this planet, making it a habitable place for human beings.

Since the industrial revolution, an increased use of fossil fuels has resulted in a significant increase in CO_2 emissions in the atmosphere. In fact, CO_2 makes up the largest portion of anthropogenic greenhouse gas. The sharp increase in the world's total CO_2 emissions from fossil fuels is shown in Figure 2.7. Even though greenhouse gases exist in nature and are needed to maintain a comfortable temperature range on Earth, an increased concentration creates an energy imbalance and causes climate change.

In addition to CO_2, other greenhouse gases include H_2O, O_3, CH_4, NO, and a trace

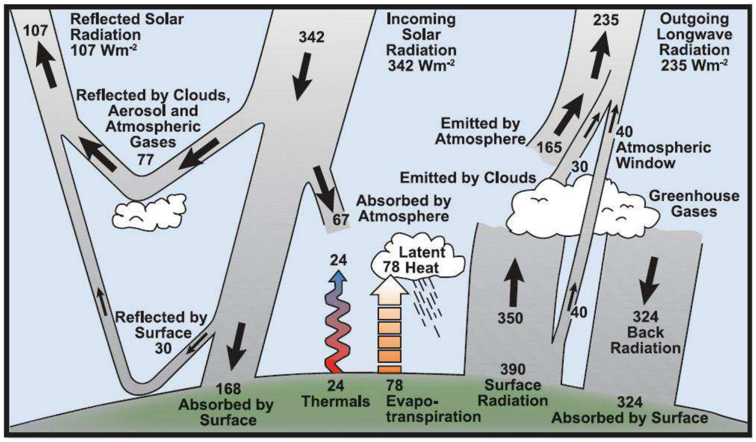

Figure 2.6: Annual global energy balance [30].

amount of other gases [1]. In any combustion process of fossil fuels (hydrocarbon), the following reaction takes place [33]:

$$C_nH_m + (n + \frac{m}{4})O_2 \rightarrow nCO_2 + \frac{m}{2}H_2O + heat \tag{2.1}$$

The burning of fossil fuels therefore necessarily emits CO_2, which explains why CO_2 is the largest anthropogenic greenhouse gas emissions. Similar to other greenhouse gases, CO_2 has a complex structure, which allows for excitation of asymmetric vibration modes. CO_2 is linear and it has four fundamental vibrations. Figure 2.8 shows three of the four modes of vibration: symmetric stretching, asymmetric stretching, and one bending. The fourth mode is another bending mode that acts exactly like case (c) but in the opposite direction. In symmetrical stretching of CO_2 (case (a)), the center of mass and center of charge do not change. Therefore, energy is conserved in symmetrical stretching and the band in the infrared spectra cannot be absorbed [34]. On the other hand, in asymmetrical

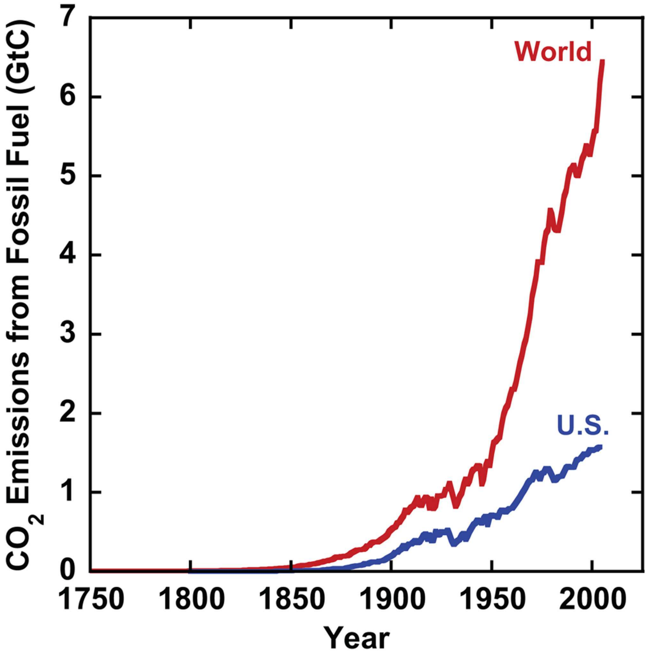

Figure 2.7: United States and total world's CO_2 emissions from fossil fuels [32].

stretching and bending vibrations, case (b) and case (c), the center of mass and the center of charge change, which creates a dipole moment. This dipole moment can be created by the absorption of infrared radiation by CO_2. The energy and momentum of the absorbed infrared photons are transferred to CO_2, resulting in asymmetric stretching and bending.

As the Earth's surface radiates long wavelength radiation back to space, CO_2 and other greenhouse gases absorb the infrared radiation and become vibrationally excited. When they relax, the total energy absorbed is released as infrared radiation in all directions, some is lost to space and some is directed back to Earth, thus warming it.

Evidence of climate change is widely observed. Figure 2.9 shows average global temperature normalized to the average temperature from 1961 to 1990. The figure illustrates two sharp temperature rise periods, one in the early 1900s and the most recent rise in the

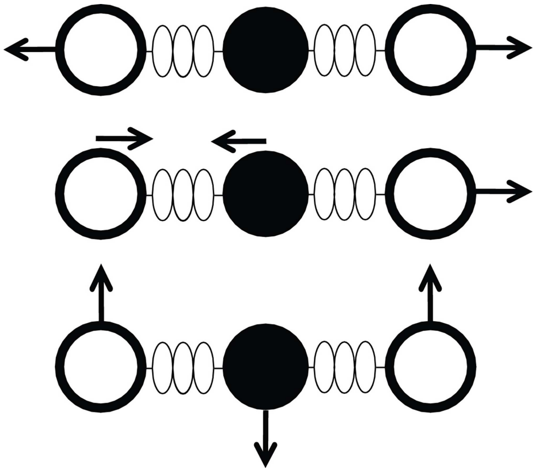

Figure 2.8: Vibration modes of CO_2: (a) symmetric stretching, (b) asymmetric stretching, (c) bending.

last several decades. The world has experienced drastic effects due to the climate change. According to the International Panel on Climate Change [1], CO_2 concentration had risen from 280 ppm (part-per-million) in the pre-industrial period to 379 ppm in 2005. This value is the highest concentration in 650,000 years. This panel blames the rise in atmospheric CO_2 concentration for the increase in global average air and ocean temperature, melting of snow and ice, and the rise in the global average sea level, as shown in Figure 2.10.

In conclusion, the world's dependence on fossil fuels as the primary energy source presents a problem that is twofold. First, fossil fuels are available in finite supplies, and they cannot address increasing future energy demand. Second, burning of fossil fuels has an indirect consequence of causing climate change through the emission of CO_2. Therefore, to solve both the energy and climate challenges, the world must alter our energy consumption habits and must get rid of our dependency on fossil fuels.

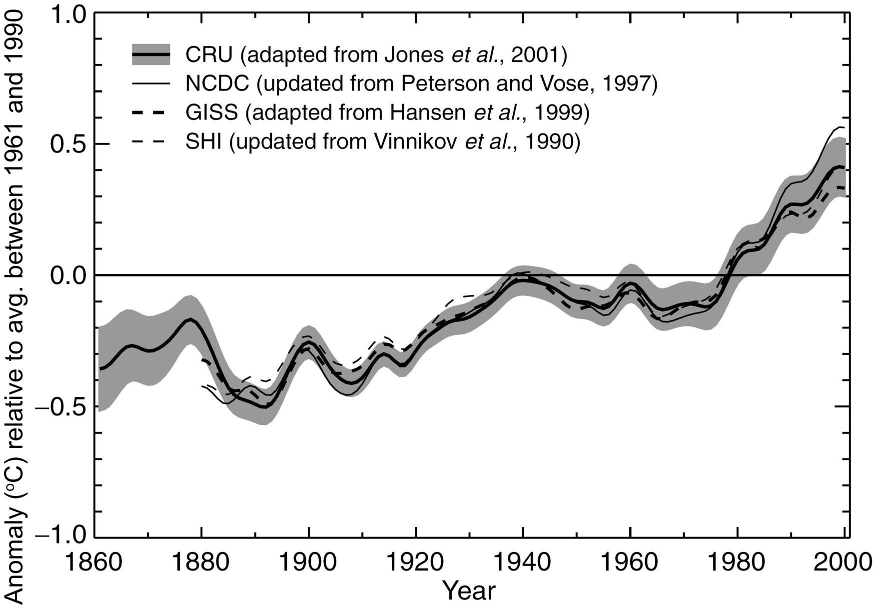

Figure 2.9: Temperature anomaly relative to the mean temperature between 1961 and 1990 [1].

2.1.3 Case Study: United States

In the previous sections, the energy and climate challenges are presented from a global perspective. These challenges have different levels of impact on individual countries. This section examines the impact on one specific country–the United States (U.S.). In the case of the U.S., finding solutions to the energy and climate challenges is also important for the country's foreign relations and thereby improving its national security.

Similar to other nations, the U.S. heavily relies on fossil fuels. Figure 2.11 shows the distribution of energy consumption in the U.S. in 2007: 84% fossil fuels (petroleum, natural gas, and coal), 8% nuclear electric power, and only 7% renewable energy [35]. Note that 34% of the renewable energy comes from hydroelectric power. Alarmingly, the U.S. consumes 25% of the world's energy. Figure 2.7 shows the U.S. emission of CO_2 com-

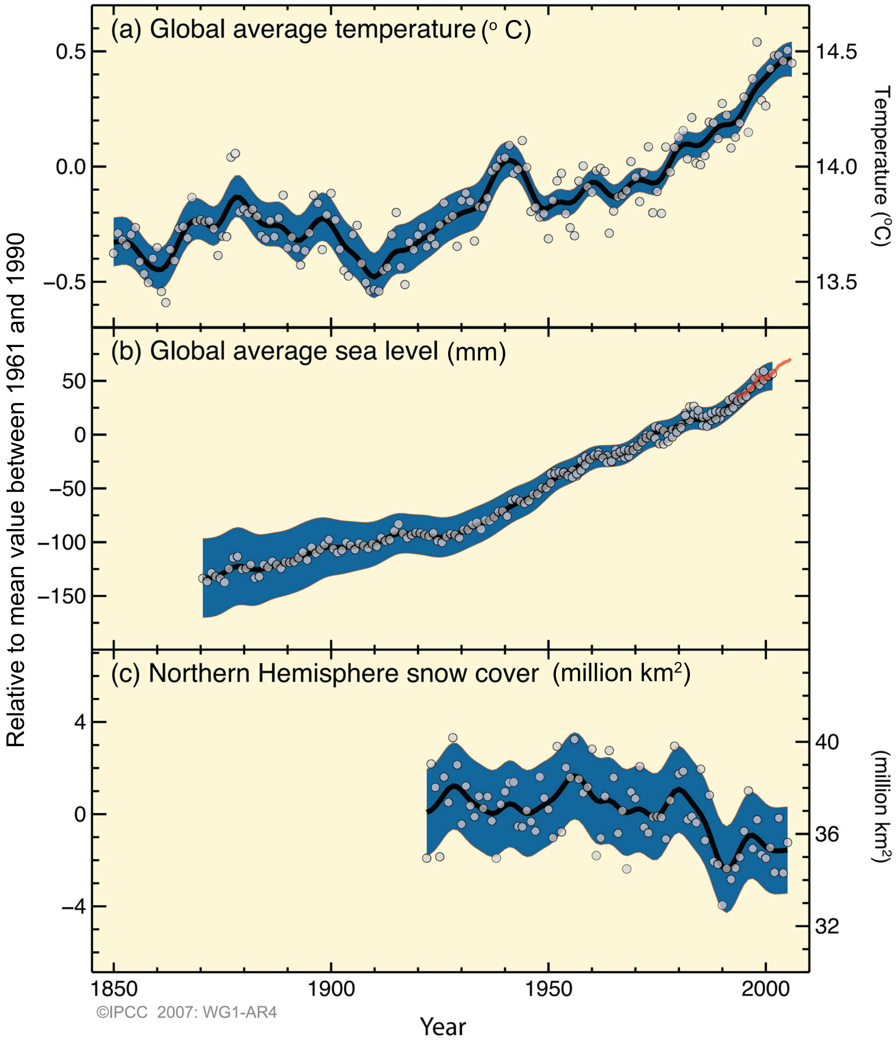

Figure 2.10: Rise in global average temperature and sea level and decrease in area of snow cover in Northern Hemisphere [1].

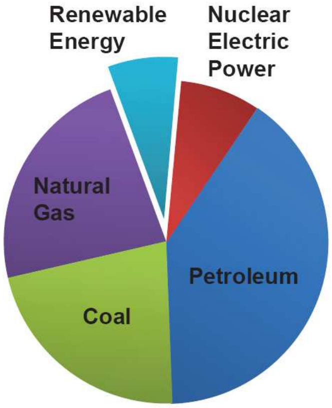

Figure 2.11: Distribution of energy consumption in the US in 2007 [37].

pared with the world's emission. In 2005, the United States emitted 25% of the world's CO_2 emission, 87% of which was related to energy consumption [36]. Among emissions from fossil fuels consumption in the U.S., 44% of emission comes from petroleum, 20% from natural gas, and 36% from coal [36]. For a country with only 4.5% of the world's population, the U.S. is a major consumer of non-renewable energy and contributor of anthropogenic CO_2 emissions.

The need to reduce fossil fuel consumption, and therefore CO_2 emission, to address the energy and climate challenges is clear. In addition, the health of the American economy depends on its access to energy. From production of domestic goods to all technological innovations, the U.S. economy cannot thrive if the country does not have access to energy, and this is true for all nations. Figure 2.12 shows current maps of the world based on land distribution along with those based on population distribution, fuel import, and fuel export. As shown, the size of the U.S. based on land distribution is similar to that based on population distribution. However, the size of the US based on fuel import is significantly

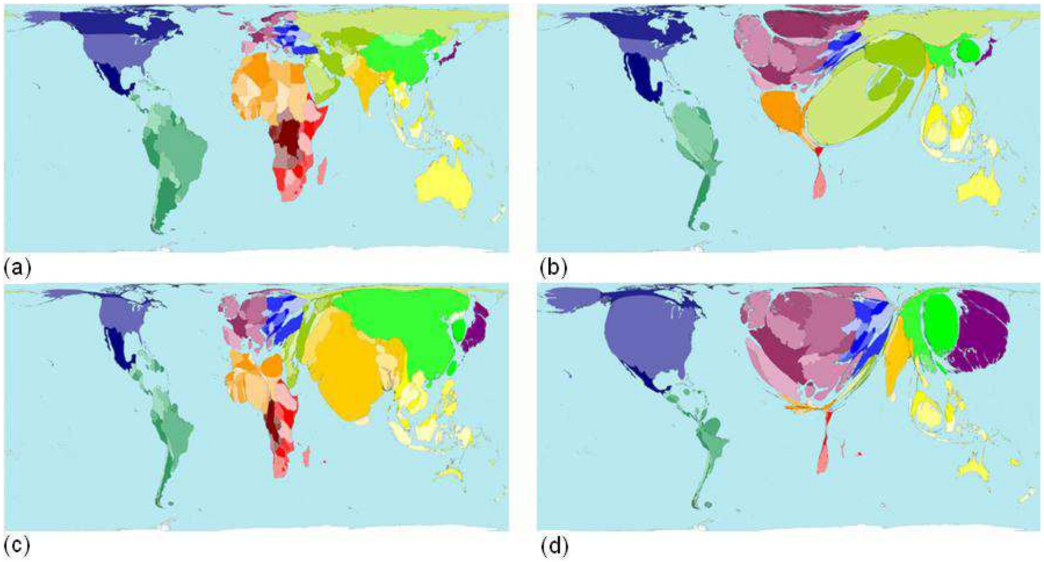

Figure 2.12: World maps reflecting (a) land distribution, (b) energy export, (c) population, and (d) energy import [38].

larger than that of fuel export.

In the last two decades, the consumption of petroleum (processed from crude oil) in the U.S. has increased while its production has decreased. This imbalance in fuel import and export requires a continuous increase in petroleum import to satisfy the country's energy demand. As an example, according to the Department of Energy's Annual Energy Review in 2008 [39], the U.S. produced 4.96 million barrels (0.789 million m^3) of crude oil per day, but it imported 9.76 million barrels (1.55 million m^3) per day mostly from Canada, Saudi Arabia, Mexico, Venezuela, Nigeria, Iraq, and Russia. With regard to natural gas, the U.S. withdrew 26.05 trillion ft^3 (0.737 trillion m^3) while importing 3.96 trillion ft^3 (0.112 trillion m^3) and 90% of natural gas imports were from Canada. Coal is the only type of fossil fuel where the U.S. has a surplus. In 2008. it produced 1062 million metric tons, imported 31.0 million metric tons, and exported 73.9 million metric tons to mostly Canada, Netherlands, Brazil, United Kingdom, France, Italy, and Belgium. From these figures, it is clear that the U.S. strongly depends on import of foreign oil.

As illustrated in Figure 2.3, most of the oil reserves are located in the least politically stable part of the world; the Middle East has 67% of the world's oil reserve. The ten countries that have the most oil in reserves as of January 2006 in descending order are: Saudi Arabia, Canada, Iran, Iraq, Kuwait, United Arab Emirates, Venezuela, Russia, Libya, and Nigeria [40]. According to a report by the Council on Foreign Relations [41], there are national security consequences of U.S. oil dependency. First, countries with a control over large oil revenues have the flexibility to adopt policies that oppose U.S. interests and values; Iran's program for nuclear weapons is an example. Second, oil dependency has forced current allies of the U.S. to realign their political partnerships with other oil-rich countries, and these realignments affect the U.S. in forming its partnerships. For example, many countries within the European Union are forming relationships with Russia and Iran because of their dependency on imported oil and gas, and these new realignments reduce the political influence that the U.S. can have in those regions. Third, due to high oil prices, some countries invest in oil-rich regions, where new relationships may pose a problem for the U.S. One example is China's investment in the Middle East and Africa. Fourth, the revenues from oil in some countries can undermine local governance, favoring totalitarian governments, such as those in Sudan. And finally, because the U.S. is dependent on foreign supplies of oil, any significant interruption in oil supply can cause adverse political and economic consequences in the U.S. For example, this had happened recently to several European countries during a dispute between Russia and Ukraine on oil prices, and as a result, Ukraine did not allow natural gas to flow from Russia into Europe.

For these reasons, reducing dependency on foreign sources of non-renewable energy is important for U.S. foreign relations. But the U.S. foreign relations are also affected by other countries' dependency, and therefore, the U.S. must also encourage others to reduce consumption of non-renewable natural resources. The U.S. should lead by example, but it is currently the highest consumer of non-renewable energy and contributor of emissions. In summary, finding alternative sources of energy to reduce dependency on limited supplies of fossil fuels and to reduce emissions is a paramount task that the world faces. To maintain continued global economic growth and to sustain this planet, the world has to find solutions to the energy and climate challenges.

2.2 Hydrogen: Benefits and Drawbacks

To address the energy and climate challenges, several alternative energy sources are investigated. One proposed solution is to use a secondary energy source–hydrogen–as an energy carrier to replace some of the fossil fuel consumption, especially in the transportation sector.

Hydrogen is the most abundant element in the universe, but it is not available in its natural form on Earth. Hydrogen must be produced from a feedstock that contains its molecules, such as natural gas, petroleum, and water. Therefore, hydrogen is considered a secondary energy source, similar to the case of electricity. There are a number of hydrogen production methods. As discussed previously and shown in Figures 2.3 - 2.5, oil, natural gas, and coal are not available as natural resources in all regions. Further, in many cases, only a few countries have ownership of much of the world's non-renewable resources. On the other hand, hydrogen can be more widely accessible because hydrogen can be produced anywhere water and power are available. With the ability and flexibility to be a decentralized source of energy, hydrogen is an attractive option.

When hydrogen is used with oxygen in fuel cells, the only by-product is water. That is, the use of hydrogen as an energy carrier in the transportation sector is completely emission-free. Recently, the Energy Information Administration (EIA) estimates that petroleum consumption in the transportation sector can be reduced between 37.1 and 84.1% of the current consumption rate and CO_2 emission can be decreased between 8.8 and 83.8% from the current emission rates when hydrogen-powered fuel cell vehicles enter the market in 2050 [42]. The actual petroleum and CO_2 emission reduction will depend on the actual level of fuel cell vehicle penetration rate and fuel economy. Nevertheless, hydrogen-powered fuel cell vehicles are a good example of the potential benefit of hydrogen to replace fossil fuels.

Hydrogen shows a great promise to address the energy and climate challenges; still, there are some drawbacks. Mainly, hydrogen is not a primary energy source. As such, it is only as clean of an energy carrier as its method of production. To produce hydrogen by a clean method has many technical challenges, which explains why 96% of hydrogen is still produced from non-renewable resources such as methane and coal worldwide [43]. In these processes, CO_2 emission presents a problem as well. Further, hydrogen production from non-renewable resources does not solve the original problem, which is to reduce our dependency on fossil fuels. Most of the remaining 4% of hydrogen is produced from conventional electrolysis [43]. In electrolysis, the energy efficiency is still lower compared to other non-renewable methods [44]. The maximum energy efficiency of the steam methane reformation method is 70-85% and for electrolysis is 40-70% [45].

Beyond the technical challenges in hydrogen production, the costs of transportation and storage are two major drawbacks. Hydrogen is the lightest gas, with a density approximately 7% that of air [46]. In addition, the condensation temperature of hydrogen at atmospheric pressure is 20 K [46]. These two characteristics pose some difficulties in transportation and storage of hydrogen. These are the current challenges that need to be addressed before hydrogen can be applied as intended. The following section outlines the main methods of hydrogen production.

2.3 Hydrogen Production Methods

Steam methane reformation (SMR), partial oxidation of heavy hydrocarbons, and coal gasification are current methods employed to produce approximately 96% of hydrogen worldwide and most of the other 4% is produced via conventional electrolysis [43]. Hydrogen when used with oxygen addresses the energy and climate challenges by reducing the consumption of fossil fuels and by reducing CO_2 emission. However, the first three methods listed below do not fully address these challenges. Non-renewable resources are used to produce hydrogen, and in many cases, CO_2 emission is a by-product in these processes.

2.3.1 Natural Gas Reforming

Methane gas makes up 95% of natural gas. Globally, 80% of hydrogen is produced from SMR, and this process accounts for 95% of the hydrogen produced in the U.S.

Steam methane reformation:

$$C_nH_m + nH_2O(+heat) \Longrightarrow nCO + (n + 0.5m)H_2 \tag{2.2}$$

In this endothermic process, heat is added to initiate the reaction. Methane is subjected to a high-temperature steam (700-1000 C) under a pressure between 300 kPa to 2500 kPa to produce a syngas, which contains a varying amount of CO and H_2 [4]. In the SMR process, a catalyst (typically nickel because of its low cost) is introduced to the system [47]. The CO product from the SMR process is often used to further produce hydrogen in what is called the water gas shift (WGS) reaction:

$$H_2O + CO \Longrightarrow H_2 + CO_2(+heat) \tag{2.3}$$

In WGS reaction, H_2O and CO with the help of a catalyst react to produce H_2 and CO_2 and a small amount of heat. SMR is currently the most cost-effective and energy-efficient method of hydrogen production, with an energy efficiency up to 85% [45,48]. In addition, the natural gas pipeline already has an established infrastructure, and this makes SMR the method of choice for hydrogen production. However, the U.S. currently imports 15% of its natural gas, and therefore, this method of hydrogen production does not address the desire of the U.S. to reduce gas imports from foreign sources. CO_2 emission is also another concern.

2.3.2 Partial Oxidation of Methane

Similar to the SMR method, partial oxidation of methane is also another hydrogen production method where the product mixture contains a syngas, which undergoes a WGS reaction to further produce H_2 from CO.

Partial Oxidation of Methane:

$$C_nH_m + nO_2 \Longrightarrow nCO + 0.5mH_2 + heat \tag{2.4}$$

This is an exothermic process, but its energy efficiency (70-80%) is less than what can be achieved with SMR. Therefore, this method is not pursued commercially.

2.3.3 Gasification

In the process of gasification, solid coal is first gasified and then it reacts with water to produce a syngas, similar to the SMR method. Hydrogen is extracted from this syngas. This method of hydrogen production is more costly than the SMR method, and has a lower energy efficiency (63%) [48]. Despite the higher cost and lower energy efficiency, this method of hydrogen production is under consideration by the U.S. Department of Energy because the U.S. currently has a supply of coal that will last for more than 250 years, the only type of fossil fuel for which the U.S. has a surplus. The reactions for this method are:

$$2C + O_2 \Longrightarrow 2CO \tag{2.5a}$$

$$C + H_2O \Longrightarrow CO + H_2 \tag{2.5b}$$

$$C + CO_2 \Longrightarrow 2CO \tag{2.5c}$$

2.3.4 Conventional Electrolysis

Methods of hydrogen production previously discussed dominate the world market or are under consideration, but they can only serve as a transition stage for hydrogen production. In order to realize the full benefits of hydrogen as a "clean" energy carrier, the process in which it is produced must have minimal CO_2 emissions and must not rely on non-renewable natural resources. The method of electrolysis is one such example–it uses an electric current to split water into hydrogen and oxygen in what is known as an electrolyzer [49]. This method is considered renewable if the electricity comes from a clean source. However, currently 43% of electricity in the United States is generated from coal [39]. That, however, does not limit the usage of renewable electricity generated from wind, solar, biomass, *etc.* When electricity is obtained from renewable or nuclear sources, then the energy cycle is sustainable. The total reaction for electrolysis is as follows:

$$2H_2O + electricity \Longrightarrow O_2 + 2H_2 \tag{2.6}$$

There are several types of electrolyzer: alkaline electrolyzer, polymer electrolyte mem-

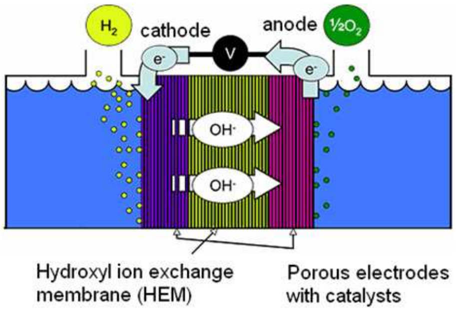

Figure 2.13: Schematic diagram of an electrolysis system, courtesy of Sandia National Laboratory.

brane (PEM), and solid oxide electrolyzer. The alkaline electrolyzer is widely available commercially. A diagram of the alkaline electrolyzer is shown in Figure 2.13.

In an alkaline electrolyzer, the electrolyte is an alkaline solution (sodium or potassium hydroxide). The reactions at the anode and cathode are:

At the anode:

$$2OH^- \Longrightarrow \frac{1}{2}O_2 + H_2O + 2e^- \tag{2.7}$$

At the cathode:

$$2H_2O + 2e^- \Longrightarrow H_2 + 2OH^- \tag{2.8}$$

The PEM electrolyzer is similar to the alkaline electrolyzer, except that the electrolyte is a solid specialty plastic material [4]. A schematic diagram of a PEM electrolyzer is shown in Figure 2.14

At the anode, the water reacts with the material of the anode to form oxygen and positively charged hydrogen ions. When an external source is connected to the electrolyzer, the electrons flow through the external circuit and hydrogen ions move to the cathode through

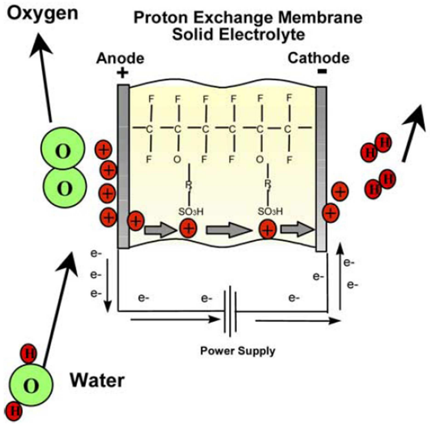

Figure 2.14: Schematic diagram of the PEM electrolyte, courtesy of F. Barbir [50].

the PEM. Hydrogen is created when hydrogen ions and electrons combine. The reactions are summarized as:

At the anode:

$$H_2O \Longrightarrow \frac{1}{2}O_2 + 2H^+ + 2e^- \tag{2.9}$$

At the cathode:

$$2H^+ + 2e^- \Longrightarrow H_2 \tag{2.10}$$

Alkaline and PEM electrolytes function very similarly, and they operate in relatively low temperature ranges: 100-150 C for alkaline electrolyzers and 80-100 C for PEM electrolyzers [4]. Solid oxide electrolyzers are different from these two types, mainly because they operate at a much higher temperature range, between 500 and 800 C. The electrolyte for these systems is a solid ceramic material.

In addition to the need of an electrolyte, catalysts are also required. The most commonly used catalysts are platinum or platinum alloys–a rare and expensive metal [50]. This is one disadvantage of the electrolysis method of hydrogen production. The electrolyzer energy efficiency ranges from 40-70% [45], but the overall efficiency is from 13 to 24% assuming that the efficiency of electricity generation is 33%. As a comparison, SMR method has an energy efficiency up to 85%. Currently, hydrogen can be produced through the method of electrolysis in small amounts of 0.45 kg/hr to as much as 434 kg/hr [44].

2.4 Conclusion

Hydrogen has an enormous potential to address the challenges that we face today. Because of its low density, hydrogen has an energy density of 120 MJ/kg compared to 42.7 MJ/kg and 41.9 MJ/kg for gasoline and diesel. Even when produced from SMR, gasification, or oxidation, hydrogen used in fuel-cell powered vehicles is a good transition stage as explained in a 2002 technical report on guidance for transportation technologies.

> “Fuel cell vehicles running on hydrogen produced from natural gas would use less energy and emit less carbon than a conventional internal combustion engine, even when considering the full fuel cycle from energy source to production to end-use.” [51]

Nevertheless, there is still a need to reduce our dependency on non-renewable natural resources, and therefore non-renewable methods of hydrogen production are not acceptable in the future. Thus, the renewable electrolysis method is possibly the best candidate but the cost of hydrogen production through electrolysis is high and this process also requires a rare resource, primarily platinum metal. In addition to the methods listed above, a number of other approaches are under investigation. For example, hydrogen is produced from water using sunlight and specialized microorganisms in a photobiological water splitting process, and hydrogen is also produced from water using sunlight in conjunction with photoelectrochemical materials in what is known as photoelectrochemical water splitting [4]. The list of hydrogen production methods under investigation further includes direct biomass gasification, sulfur iodine cycle, and many other derivatives of the methods aforementioned [48]. Among those novel approaches is plasma electrolysis, the use of a plasma source to directly dissociate water molecules into hydrogen and oxygen. This is the topic of this dissertation and the subject of plasma is introduced in the next chapter along with a literature review on current water plasma research.

Chapter III

Background–Plasma Overview

A review of existing hydrogen production methods in Chapter II reveals that current methods employed to produce more than 96% of hydrogen do not directly address the energy and climate challenges. Hydrogen production from electrolysis with the use of "clean" electricity is the primary renewable hydrogen production method. Conventional electrolysis, however, has some drawbacks, and plasma electrolysis–the subject of this dissertation–is argued to have the potential to address some of these drawbacks. First, Section 3.1 provides an overview of plasma physical processes in a water vapor discharge. Then Section 3.2 explains the methods of plasma generation. Section 3.3 lists some examples of plasma sources, and finally Section 3.4 provides a literature review of the water plasma studies.

3.1 Overview of Plasma Physical Processes in Water Vapor Discharge

3.1.1 Collisional Phenomena in Plasmas

Before a discussion on how a plasma is generated, the structures of an atom and a molecule need to be examined. A thorough treatment is given in References 52 and 53.

Only a brief description is given in this section to serve as background information for the discussions in the upcoming sections.

For atoms, collisions with electrons can result in elastic scattering in which the total kinetic energy is conserved but the momentum of the electron is changed, or in inelastic processes including electronic excitation and ionization in which the total kinetic energy is not conserved. A collision between an atom and an ion can result in an elastic scattering, where the momentum and energy of the two species are exchanged [52]. However, the structure of a molecule is more complex due to a higher number of degrees of freedom it possesses. Unlike an atom, a molecule has vibrational and rotational motions. Within each electronic states, there are discrete vibration and rotation energy levels. The Born-Oppenheimer Approximation assumes that the electronic motion and the nuclear motion in molecules can be separated. The nuclear motions (vibration and rotation) are slow compared to the electronic motions [52], and therefore, we can draw potential energy curves for the electronic states of a diatomic molecule as shown in Figure 3.1. The diagram shows the potential energy versus the internuclear distance, each representing quantized electronic level for a frozen set of nuclear positions [52].

In the ground electronic state, the minimum potential energy must have a value that represents the intermolecular distance R. For higher electronic states, the minimum potential energy can shift [52]. This observation is important in future discussions on different dissociation mechanisms.

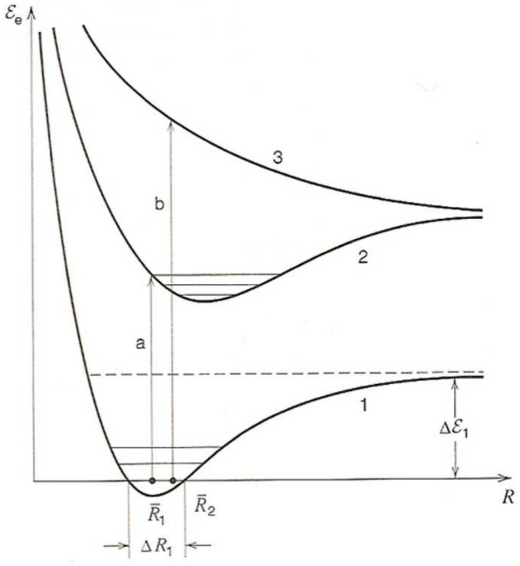

Figure 3.1: Potential curve for a molecule AB [52].

3.1.2 Mechanisms of Electron and Ion Creation

Generating and sustaining a plasma require production of electrons and ions, which is accomplished through ionization processes [52–54]. Ionization is a result of an inelastic collision. If most of the products of such collisions are positive ion and electron pairs, then the plasma is an electropositive plasma. All noble gases, such as argon and xenon, produce electropositive plasmas. However, a neutral gas particle can also become a negative ion, instead of a positive ion, if the gas has a high electron affinity. Electron affinity is the difference in energy between a neutral atom and its negative ion; it is the energy released when an electron combines with a neutral to become a negative ion [55,56]. Note that the electron affinity is positive if the negative ion has a lower energy than the neutral atom (*e.g.* O_2, Cl_2, and F), and is negative if the negative ion has a higher energy than the neutral atom (*e.g.* noble gases such as Ar and Xe) [55]. A plasma is then an electronegative plasma if the majority of the ions are negative ions. In this section, three main ionization processes are discussed: direct ionization by electron impact, stepwise ionization by electron impact, and ionization by collision with heavy particles [54]. All of these processes result in a production of positive ion and electron pairs.

Direct Ionization by Electron Impact

Direct ionization by electron impact is among the most common ionization processes in many plasma sources–including the water plasma source investigated in this work. In the direct ionization by electron impact for an atom, a positive ion and electron pair is created. Ionization occurs if the electron's energy exceeds the ionization energy of the state of the atom–the energy required to remove an outermost electron from an atom or molecule. The reaction equation for this process is shown in Equation 3.1(a). For the molecules, the direct ionization by electron impact can result in two outcomes. First, non-dissociative ionization produces a molecular ion and electron pair as shown in Equation 3.1(b), similar to the case of an atom. However, for molecules, there is also another possibility; *i.e.* dissociative ionization, as shown in Equation 3.1(c).

$$e + A \rightarrow A^{+} + e + e \tag{3.1a}$$

$$e + AB \rightarrow AB^{+} + e + e \tag{3.1b}$$

$$e + AB \rightarrow A + B^{+} + e + e \tag{3.1c}$$

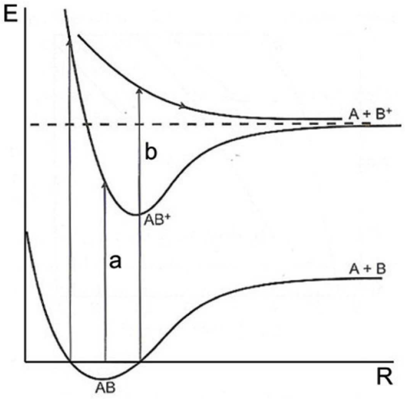

Figure 3.2: Potential curve for a molecule AB, showing dissociative ionization of molecule AB [52, 53].

The Franck-Condon Principle is introduced to explain the dissociative ionization process. Inside a molecule, the fastest internal motion of atoms is molecular vibration, but the time scale for molecular vibrations is still much longer than the time scale for the interaction between the electrons and the molecules [53]. Therefore, the atoms inside a molecule are considered being frozen when a molecule, stimulated by electron impact, becomes electronically excited [52, 53], and this is known as the Franck-Condon Principle. This principle allows for the potential energy curves representing the potential energy versus internuclear distance of the molecule to be drawn. Figure 3.2 shows the potential energy curves for molecule AB. Vertical line a shows the case for non-dissociative ionization, in which the molecule is excited into a high quantum number bound vibration state. Vertical line b shows the case of dissociative ionization, where the dissociation of the molecule is energetically permitted because the molecule is excited to a vibrationally unbound state [52, 53].

Table 3.1: Ionization potential energy [52, 54]

Atom or Molecule	**Energy (eV)**
Ar	15.8
H	13.6
O	13.6
OH	13.2
O_2	12.2
H_2O	12.6

Table 3.1 gives a list of ionization energies for atoms and molecules in a water plasma and for argon gas. As noted, ionizing noble gases such as argon is harder than ionizing gas species present in a water plasma. References 54, 57–59 and 52 provide detailed physical insights on this topic.

Stepwise Ionization by Electron Impact

Stepwise ionization by electron impact is similar to direct ionization, but this process occurs particularly when the plasma density is high. In a high density plasma, the collisional frequency between electrons and neutrals is increased, but the energy transferred from the electrons to the neutrals is not necessarily high enough to cause ionization. In many cases, the neutral particles become excited neutrals through an inelastic collision with electrons; however, this means the density of excited neutral is also high. Therefore, ionization is possible when an electron of sufficient energy collides with an excited neutral. Effectively, the neutrals are ionized in two steps: excitation and then ionization. The net ionization energy in this process is equal to that in the direct ionization process, but stepwise ionization rate is higher than direct ionization [54] because collisional frequency is higher in dense plasma.

Ionization by Collision with Heavy Particles

In general, heavy particles by nature are massive and usually do not possess enough energy to create ionization. However, ionization is possible if the heavy particles are in excited states. When a metastable atom A^* collides with another atom B, if the excitation energy of A^* exceeds ionization potential of B, ionization occurs. This is known as Penning ionization [54].

Penning ionization:

$$A^* + B \rightarrow A + B^+ + e \tag{3.2}$$

In addition, a collision between a pair of heavy particles can also result in a charge-exchange process. When an energetic ion hits a cold neutral, the products of this collision can be a cold ion and an energetic neutral [60]. Take argon as an example, the charge-exchange process is:

$$Ar^+(fast) + Ar(slow) \rightarrow Ar(fast) + Ar^+(slow) \tag{3.3}$$

The list of ionization processes discussed above is not complete, but these are the main processes in most plasmas.

3.1.3 Mechanisms of Electron and Ion Destruction

The previous section outlines important ionization processes in which electrons and positive ions are created. In this section, the main mechanisms of electron and ion losses are examined. The main loss mechanisms for positive ions and electrons are through recombination processes [52, 54]. But electrons can also be removed through several attachment processes in a plasma when species with high electron affinity are present [52, 54]. The processes to be discussed are: electron-ion recombination, electron attachment, detachment processes, ion-ion recombination, and surface recombination .

Electron-Ion Recombination

In electron-ion recombination, an electron and positive ion pair recombines to produce a neutral atom for the case of an atomic ion. For the case of a molecular ion, the recombination can result in either a production of a neutral molecule or dissociation into multiple neutral atoms. For both cases, either electron-atomic ion or electron-molecular ion recombination, the process is exothermic.

For atomic ions, the first electron-ion neutralization process is a three-body electron-ion recombination, which is important in a high-density plasma:

Three-body electron-ion recombination:

$$e + e + A^{+} \rightarrow A^{*} + e \tag{3.4}$$

Here one electron acts as a third-body partner and the atomic positive ion becomes an excited neutral after the recombination. Any excess energy from this recombination goes into the kinetic energy of the free electron [53]. This three-body electron-ion recombination process dominates in most density regimes. But in the case of a relatively low-density plasma, another process can compete with this three-body electron-ion recombination process, and that is the radiative electron-ion recombination. Here, the excess energy is converted into radiation [53].

Radiative electron-ion recombination:

$$e + A^{+} \rightarrow A^{*} \rightarrow A + \hbar\omega \tag{3.5}$$

The above two processes are described for a recombination between an electron and an atomic ion. For an electron-molecular ion pair, the most common recombination is dissociative electron-ion recombination.

Dissociative electron-ion recombination:

$$e + AB^{+} \rightarrow (AB)^{*} \rightarrow A + B^{*} \tag{3.6}$$

This process can be best described using the potential curves shown in Figure 3.3. When an electron and molecular ion (AB^{+}) recombine, the electron is captured, and therefore the electron does not have a means of carrying away a part of the reaction energy [52]. The molecular ion AB^{+} after the recombination with an electron has acquired an additional energy equal to ϵ_d or $\epsilon_{d'}$ as shown in Figure 3.3, which results in a repulsive state of A and B^{*}. Because the potential curve for AB^{+} is always above the repulsive state of AB, the electron-molecular ion recombination in this case can never result in ground states of A and B [52].

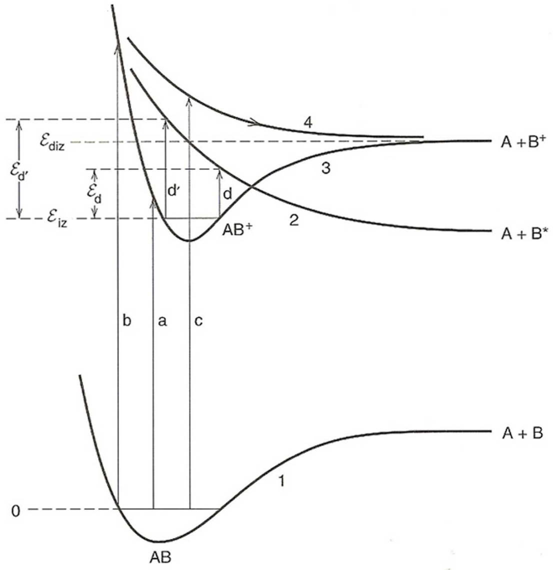

Figure 3.3: Potential curve for a molecule AB, showing dissociative recombination of molecule AB [52].

Note that for an electron-molecular ion pair, radiative electron-ion recombination is also possible. However, the rate constant for radiative recombination for an electron-molecular ion pair is between three and five orders of magnitude lower than that for dissociative recombination [52].

Electron Attachment

Through a collision between an electron and a neutral, one possible outcome is ionization as discussed in Section 3.1.2. But when the neutral (or one atom within the molecule) has a positive electron affinity, which can be thought of as an ability to form stable negative ions, then the outcome of such collision is electron attachment–not ionization. Electron attachment processes include dissociative electron attachment and three-body electron attachment to molecules. Similar to the case of dissociative electron-ion recombination, in

Table 3.2: Electron affinity [54]

Atom or Molecule	**Energy (eV)**
$H^- = H + e$	0.75
$O_3^- = O_3 + e$	2.0
$OH^- = OH + e$	1.8
$O^- = O + e$	1.5
$O_2^- = O_2 + e$	0.44
$HO_2^- = HO_2 + e$	3.0

dissociative electron attachment the molecule AB acquires energy when it recombines with an electron. In the case of dissociative recombination, the products are A and B*, but in the case of dissociative electron attachment, the electron is attached to one of the atoms (A or B) that has a positive electron affinity.

Dissociative electron attachment:

$$e + AB \rightarrow (AB^-)^* \rightarrow A + B^- \tag{3.7}$$

This electron attachment can only occur if the atom has a positive electron affinity. For example, electron dissociative attachment is possible for O_2 or H_2O because both H and O have positive electron affinities. But electron dissociative attachment is not possible for N_2 because the electron affinity for N is negative (-0.07 eV) [55]. Note again that the electron affinity is positive if the negative ion has a lower energy and is negative if the negative ion has a higher energy than the neutral atom.

Dissociative electron attachment is an important process in water plasmas because its molecular fragments have positive electron affinities, shown in Table 3.2. Table 3.3 shows the relevant dissociative electron attachment processes in a water plasma.

Table 3.3: Dissociative electron attachment [54].

$e + O_2 \rightarrow O^- + O$
$e + H_2 \rightarrow H^- + H$
$e + H_2O \rightarrow H^- + OH$
$e + H_2O \rightarrow O^- + H_2$
$e + H_2O \rightarrow H + OH^-$

Table 3.4: Three-body electron attachment [54].

$e + O_2 + O_2 \rightarrow O_2^- + O_2$
$e + O_2 + H_2O \rightarrow O_2^- + H_2O$
$e + O_2 + H_2 \rightarrow O_2^- + H_2$

In addition to dissociative electron attachment, three-body electron attachment is another process in which negative ions are formed. This three-body reaction is only dominant at high pressures (p $>$ 0.1 atm) [54] and similar to the process discussed above, one of the particles must have a high positive electron affinity.

Three-body electron attachment to molecules:

$$e + A + B \rightarrow A^- + B \tag{3.8}$$

Here A and B can be a molecule, but the energy of the electron is not high enough to cause dissociative electron attachment as in the previous case. An excellent example of this process takes place in an oxygen plasma at high pressure (atmospheric): $e + O_2 + M \rightarrow O_2{}^- + M$. The third body (M) is needed in this process to carry away the excess energy from the colliding two-body system (e + O_2) in order to satisfy the conservation of momentum and energy [61]. Table 3.4 shows examples of electron attachment to oxygen in three-body electron attachment processes.

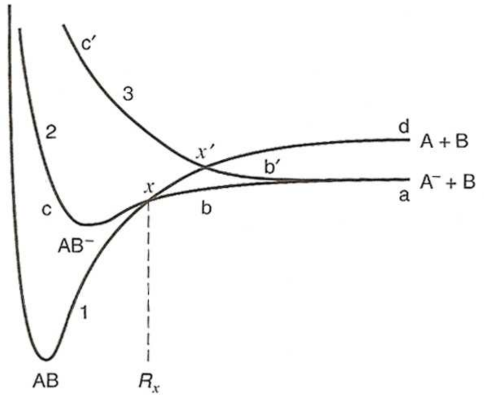

Figure 3.4: Potential curve for a molecule AB, showing dissociative detachment of molecule AB [52].

Detachment

In addition to the loss of electrons through attachment, there are recombination mechanisms that result in the loss of negative ions. Some of those include associative detachment and electron impact detachment.

The first process, associative detachment, is the reverse process of dissociative attachment. Figure 3.4 illustrates the potential energy diagram and is shown to accompany the explanation of this process.

Associative detachment:

$$A^- + B \rightarrow (AB^-)^* \rightarrow AB + e \tag{3.9}$$

When A$^-$ and B interact, they can follow the path a-b-c labeled in Figure 3.4 to become an unstable AB$^-$ and after which, the electron detaches carrying excess energy so that the unstable AB$^-$ relaxes into the AB ground state 1 at c [52]. Table 3.5 shows possible

Table 3.5: Associative detachment [54].

$H^- + H \rightarrow H_2 + e$
$H^- + O_2 \rightarrow HO_2 + e$
$O^- + O \rightarrow O_2 + e$
$O^- + O_2 \rightarrow O_3 + e$
$O^- + H_2 \rightarrow H_2O + e$
$OH^- + O \rightarrow O_2 + e$
$OH^- + H \rightarrow H_2O + e$

associative detachment processes in water plasmas.

Similarly, electron impact detachment is also an important process and it is analogous to the process of direct impact ionization of neutrals.

Electron impact detachment:

$$e + A^- \rightarrow A + e + e \tag{3.10a}$$

$$e + AB^- \rightarrow AB + e + e \tag{3.10b}$$

This process occurs in both negative atomic or molecular ions. In the case of direct impact electron-neutral ionization, the neutral is ionized if the electron colliding into the neutral has a potential greater than the ionization potential energy of the neutral. Here, impact detachment occurs if the electron colliding into the negative ion (either atomic or molecular) has an energy higher than the electron affinity of A or AB [52].

Ion-Ion Recombination

Ion-ion recombination processes remove negative and positive ions in both binary and three-body collisions. These processes are usually dominant at high pressures, in tens of torr. Because the work of this dissertation investigates only a low-pressure plasma (p $<$ 1 torr), these processes are not dominant, but are listed here for future works that may consider operating at higher pressures.

First, it is important to note that these processes require the presence of both negative and positive ions. Therefore, in the absence of negative ions, these processes do not take place. Binary ion-ion recombination occurs at lower pressure (p $<$ 20 -30 torr) and three-body ion-ion recombination requires a higher pressure (p $>$ 20-30 torr) [53].

Binary ion-ion recombination:

$$A^- + B^+ \rightarrow A + B^* \tag{3.11}$$

Three-body ion-ion recombination:

$$A^- + B^+ + M \rightarrow A + B + M^* \tag{3.12}$$

In a binary collision, the excess energy goes into exciting one of the neutrals. For the three-body ion-ion recombination, the excess energy is absorbed by the third-body (M) [52]. Table 3.6 lists some examples of ion-ion recombination processes.

Table 3.6: Ion-ion recombination [54].

Reactions	**Released Energy**
$H^- + H^+ \rightarrow H + H$	12.8
$O^- + O^+ \rightarrow O + O$	12.1
$O^- + O_2^+ \rightarrow O + O_2$	11.6
$O_2^- + O^+ \rightarrow O_2 + O$	13.2
$O_2^- + O_2^+ \rightarrow O_2 + O_2$	11.6

Surface Recombination

Similar to Section 3.1.2 on plasma generation mechanisms, this section on loss mechanisms has not exhausted the list of all possible recombination processes, but has described the relevant ones in water plasmas. The last process to be discussed is most dominant in low-pressure plasmas, which is the regime of this investigation. In low-pressure plasmas, the main loss mechanism is not necessarily through the interactions between neutrals, electrons, and ions, but is due to wall-surface recombination. Electrons or charged particles when colliding onto the wall surface either recombine or react with the wall material. This is the main concern for the water plasma because hydrogen, being a very low-mass particle, can easily be lost to wall-surface recombination.

3.1.4 Dissociation of Molecules

The previous two sections describe some electron and ion generation and destruction processes. There is another important process that does not fall into the above categories but is an important process in a plasma with a molecular gas; *i.e.* electron impact dissociation. For direct dissociation, the reaction is:

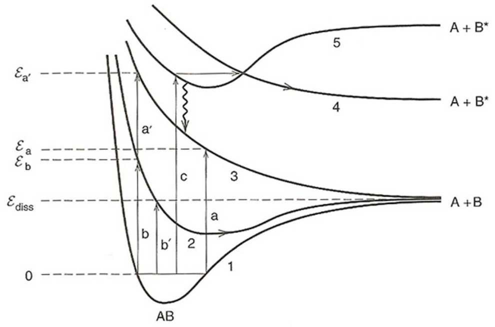

Figure 3.5: Potential curve for a molecule AB, showing dissociation processes of molecule AB [52].

$$e + AB \rightarrow A + B + e \tag{3.13}$$

Figure 3.5 shows the energy potential curves that can result in electron impact dissociation. The dissociation of molecule AB is possible if through a collision, the ground state of AB is excited to a repulsive state of AB, shown as reaction a and a' in Figure 3.5 [52].

3.2 Methods of Plasma Production

Plasma as an ionized medium has competing processes for the loss of electrons and ions. The rate of electron and ion losses, usually via recombination, is dependent on a number of factors including operating pressure, electron number density, gas properties, and electron temperature. In ionization processes, the presence of electrons and collisions between those electrons and other species in the discharge are necessary. This section describes how the electrons gain their energy in a plasma source; *i.e.* electron heating mechanisms. These electron heating mechanisms are: Ohmic or Joule heating, secondary electron emission heating, stochastic heating, and wave-particle interaction heating. Note that for any particular discharge, a combination of several heating mechanisms is possible in order to generate and sustain the discharge.

3.2.1 Joule Heating

Joule heating, also known as Ohmic heating, is the most common electron heating mechanism in most plasma sources. Electrons, in the presence of an electric field (DC or RF), experience an electric force and accelerate in the direction opposite of the electric field:

$$\vec{F} = m\vec{a} = e\vec{E} \tag{3.14}$$

where $\vec{F}$ is the force acting on the electron, m is the electron mass, $\vec{a}$ is the acceleration of the electron, e is the electron charge, and $\vec{E}$ is the electric field.

Independent of the presence of the magnetic field and whether or not the electric and magnetic fields are uniform, in the absence of collisions, electrons will accelerate and gain kinetic energy in response to an electric field. When an accelerating electron collides into another particle, possible outcomes include both elastic and inelastic collisions. In elastic collisions, the sum of kinetic energies are conserved, but particles can exchange their kinetic energies. In this case, some of the kinetic energy of the electron is transferred to the other particles and the electron loses its direct motion and travels in a random motion.

In inelastic collisions, the kinetic energy of the particles can convert into other forms of energy such as excitation or ionization of a particle. Joule heating, therefore, refers to the process in which electrons gain kinetic energy in an electric field and transfer some of their kinetic energy to other species in the plasma through collisions. The power transferred to the electron from the electric field in the presence of collisions in a weakly ionized gas is [53, 54]:

$$P = \sigma E^2 = \frac{n_e e^2 E^2}{m \nu_{en}} \tag{3.15}$$

where P is the power density transferred from the electric field to plasma electrons (in W/m^3), σ is the electron conductivity, ν_{en} is the electron-neutral collision frequency. Again E, n_e, and m are the electric field, electron density and mass, respectively.

The relationship established in Equation 3.15 is derived from the fact that power dissipated is a dot product of current and electric field:

$$P = \vec{J} \cdot \vec{E} \tag{3.16}$$

and a substitution of Ohm's law ($\vec{J} = \sigma \vec{E}$) is made and assuming that the electron-neutral collision frequency is constant. The electron conductivity is:

$$\sigma = \frac{n_e e^2}{m \nu_{en}} \tag{3.17}$$

.

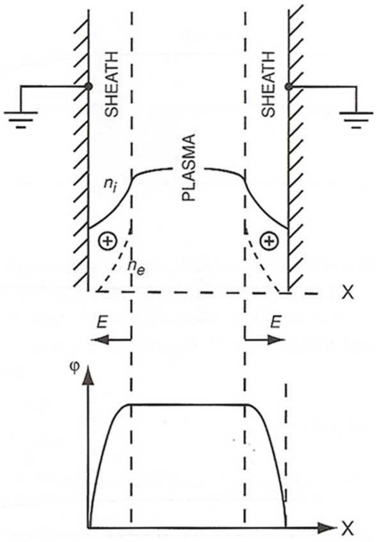

Figure 3.6: Plasma sheath in a DC plasma discharge [52].

3.2.2 Secondary Electron Emission Heating

Plasmas are quasineutral ($n_i \approx n_e$); however, this is only true in the bulk of the discharge. Eventually, the plasma comes into contact with the wall of the discharge. In a layer that typically has a length (known as a sheath thickness) equal to a few Debye lengths, quasineutrality is not maintained. This layer is referred to as the sheath. Quasineutrality cannot be maintained in the sheath because electrons, being low-mass particles, are much more mobile than the ions. The electron's thermal velocity is larger than the ion's by a factor of $\sqrt{(T_e M)/(T_i m)}$, where T_e and T_i are the electron and ion temperature, respectively, and m and M are the electron and ion mass, respectively. Typically, this value is on the order of 1000 [53]. An illustration of the plasma with two sheaths are shown in Figure 3.6.

Secondary electron emission heating occurs in the cathode sheath, where there is a sharp potential drop as seen in Figure 3.6. As a result of this potential hill, an ion at the edge of the plasma sheath is accelerated toward the cathode or the wall at ground potential as is the case shown in Figure 3.6. Without collisions, the ion, when it strikes the cathode, has an energy equal to the initial sheath potential energy. If this energy is high enough, a secondary electron is released from the cathode. In the presence of a strong electric field in the sheath, the secondary electron gains kinetic energy as it travels up the potential hill. If the secondary electron collides with a gas particle, ionization can occur if the electron's energy is sufficiently large [52].

3.2.3 Stochastic Heating

Another heating mechanism is stochastic heating, also known as collisionless heating; it is unique to RF plasma sources. In RF discharges, the sheath edge oscillates in response to the oscillating applied electric field as shown in Figure 3.7. The ion density is taken to be constant across the sheath assuming that the ion mass is large and therefore the ions do not respond to the instantaneous potentials. On the other hand, electrons are assumed to respond to the instantaneous potentials and that the electron density is zero in the sheath [52]. This is only a simplified model, but is sufficient to apply to describe stochastic heating.

When electrons in the bulk plasma impinge on the oscillating sheath edge, they suffer a change of velocity. If the sheath moves into the bulk plasma, the electrons impinging the sheath are reflected and their velocities are increased by approximately twice that of the sheath edge velocity [52, 54, 59]. This process is analogous to a low-mass ping pong ball hitting a moving wall. If the sheath moves away from the bulk plasma, the electrons

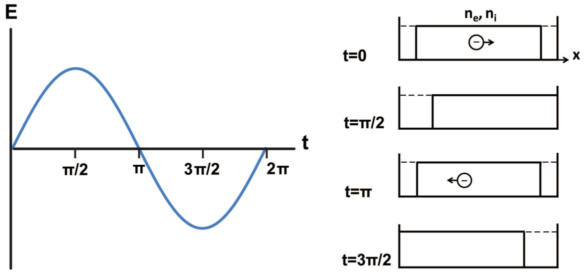

Figure 3.7: Plasma sheath in a RF plasma discharge.

impinging the sheath lose some of their energy in order to follow the sheath. On average, if the net electron flux to the boundary moving from the electrode equal that moving to the electrode, the electron would have a net zero energy gain over one cycle. However, the electron flux to the boundary moving from the electrode is higher than that moving to the electrode; therefore, energy is transferred to the electrons [54].

A simplified equation similar to Equation 3.15 can be derived for stochastic heating. Assuming that the ion density is uniform in the sheath and that the electrons at the sheath edge have a Maxwellian distribution function, the stochastic electron power for each sheath is [52]:

$$\bar{S}_{stoc} = \frac{1}{e}\frac{m\bar{v}_e}{e^2 n}{J_1}^2 \tag{3.18}$$

where $\bar{S}_{stoc}$ is the stochastic electron power per unit area and J_1 is the current density, which is entirely due to conduction inside the plasma.

3.2.4 Resonant Wave-Particle Interaction Heating

Despite the high densities that can be achieved by an inductive plasma source–10^{17} to 10^{18} m^{-3}–there are applications in which an even higher density is desired. For example, water molecule dissociation in the discharge relies on electron-impact reactions. The higher electron density increases the rate of these reactions. However, inductively-coupled plasma sources have a physical density limitation [52]. The desire for creating higher plasma density discharges motivates the work in the design of plasma sources where the electron heating mechanism involves the interaction between waves and particles. Such heating mechanisms occur in electron-cyclotron resonant (ECR) and helicon plasma sources. In ECR sources, a right-hand circularly polarized wave are resonantly absorbed by electrons in the presence of the magnetic field if the RF frequency is approximately equal to the electron cyclotron frequency ($\omega_{RF} \approx \omega_{ce}$).

3.3 Plasma Sources

The previous section outlines the main methods of plasma production by discussing different types of heating mechanisms. Several common types of plasma discharge are presented in this section: direct current (DC), capacitively-coupled, inductively-coupled, and helicon plasma sources. This section provides basic descriptions of these sources and explains the benefits of using the helicon plasma source for the work of this dissertation for dissociating water molecules through direct electron-impact reactions.

3.3.1 Direct Current Plasma Sources

In a direct current (DC) plasma source, the main electron heating mechanisms are described previously: Ohmic heating and secondary electron heating. Ohmic heating occurs in the bulk of the plasma and secondary electron heating occurs in the cathode sheath. A typical DC glow discharge plasma source consists of two electrodes connected to a DC power supply. In a positive column discharge, the potential decreases continuously at a constant rate in the direction from the anode to the cathode [52], establishing a constant electric field. An electron in the positive column accelerates in the presence of the electric field, and Ohmic heating is achieved through collisions between electrons and other particles in the bulk discharge. In the cathode sheath, secondary electrons are emitted from the cathode surface or from the wall via ion bombardments and secondary electron heating occurs due to the presence of a strong electric field within the sheath.

In both cases–Ohmic heating and secondary electron heating–gas pressure strongly affects the ionization rate. In Ohmic heating, if the pressure is too high, the mean free path of the electrons are too short for them to gain enough energy from the electric field to cause ionization. However, when the pressure is too low, not enough collisions occur to generate substantial ionization. Likewise, there is an optimum pressure in the cathode sheath to achieve secondary electron emission. If the pressure is too high, the ions will lose energy through collisions before they reach the cathode.

3.3.2 Capacitively-Coupled Plasma Source

The capacitively-coupled plasma source is the first of the three RF plasma sources to be discussed in this section. A capacitively-coupled plasma is sustained by RF currents and voltages directly applied to the electrodes and the electrodes are placed either directly inside the plasma or outside the chamber. Typically, RF plasma systems are driven by a 50-Ω RF power source that operates at 13.56 MHz frequency. A matching network is needed to match the impedance of the RF power supply output to the impedance of the plasma load. Unlike a DC discharge, a capacitive plasma discharge has stochastic or collisionless heating that results from the interaction of the RF sheath and bulk plasma. Essentially, as the electrons oscillate with the time-varying electric field, they impart some of their energy through collisions with other particles in the bulk discharge. At the same time, depending on the gas pressure, Ohmic heating is also taken place in the bulk discharge if the pressure is high enough such that there are sufficient electron-neutral collisions.

3.3.3 Inductively-Coupled Plasma Source

In the capacitively-coupled plasma sources, in general, the electromagnetic fields are applied directly to the electrodes. For inductively-coupled plasma source, the electromagnetic field is induced by an inductive coil [54], which can be planar or cylindrical. Compared to capacitively-coupled plasma, the inductively-coupled plasma discharges can reach high antenna currents, high electric conductivity, and high electron density at relatively low values of electric field and voltage [54]. The inductive coil can be considered as a transformer, where the coil represents the primary windings and the plasma the secondary winding. Therefore, the coil can effectively increase the current going into the plasma discharge. It is this effective coupling between the inductive coil and the plasma that allows the inductively-coupled plasma to achieve as much as 10 times higher in electron density compared to the capacitively-coupled plasma [54]. Further, an inductively-coupled plasma source is electrodeless and does not have any issues relating to contamination of the electrode.

In an inductive source, RF current and voltage are usually applied to a planar or cylindrical coil outside the discharge. The RF power is coupled to the plasma through a dielectric window or wall. Due to the time-varying current applied to the coil, it generates an inductive magnetic field and electric field inside the discharge. The electric and magnetic fields can only penetrate into the plasma within a distance from the surface of the discharge in what is known as the skin layer. The thickness of this layer is known as the skin depth. The skin depth δ is the inverse of the spatial decay constant α within a plasma for an electromagnetic wave normally incident on the boundary of a uniform density plasma [52]:

$$\alpha = \frac{1}{\delta} = -\frac{\omega}{c} Im {K_p}^{1/2} \tag{3.19}$$

In Equation 3.19, ω is the applied RF frequency, $c = \sqrt{1/(\mu_o \epsilon_o)}$ is the speed of light, and K_p is the relative plasma dielectric constant, which is:

$$\kappa_p = 1 - \frac{\omega_{pe}^2}{\omega(\omega - j\nu_m)} \approx -\frac{{\omega_{pe}}^2}{\omega^2(1 - j\nu_{en}/\omega)} \tag{3.20}$$

where ν_{en} is the electron-neutral collision frequency. For the collisionless regime, where $\nu_{en} \ll \omega$, and substituting the expression for electron plasma frequency, the skin depth is:

$$\delta = \sqrt{\frac{m}{e^2 \mu_o n_s}} \tag{3.21}$$

The skin depth thickness is therefore inversely proportional to the square root of the electron number density. For example, if the density is 10^{16} m^{-3}, the skin depth thickness is 5 cm, but if the density is one order of magnitude higher at 10^{17} m^{-3}, the skin depth thickness is 1.7 cm.

The collisionless assumption made in deriving Equation 3.21 is valid only for the low pressure regime in this experiment. For higher pressures where $\nu_{en} \ll \omega$ condition no longer holds, the collisional skin depth thickness is:

$$\delta_c = \delta \sqrt{\frac{2\nu_{en}}{\omega}} = \sqrt{\frac{2}{\omega \mu_o \sigma_{dc}}} \tag{3.22}$$

where σ is the electron conductivity, which is proportional to the electron number density. For 250 mtorr and 13.56 MHz, the collisional skin depth is greater than the value of the collisionless skin depth by a factor of 2-3. In both collisionless or collisional regimes, power from the electric field can only be transferred to the plasma electrons within this skin depth layer near the plasma source. The plasma density, therefore, is concentrated in this layer. The layer thickness can be controlled by the frequency, but at the same time, is affected by the electron number density. Higher electron number density reduces the skin depth thickness.

Lastly, it is important to note that even if an inductive mode is excited, there is always some capacitive coupling [52]. At high plasma densities, the skin depth thickness is small, and inductive coupling dominates. But at lower densities, the skin depth thickness can be large (for example, 5-10 cm) and power deposition through capacitive coupling can be significant.

3.3.4 Helicon Plasma Source

The plasma source employed for the experimental part of this dissertation was a helicon-type plasma source. Helicon waves were first researched in the early 1960s but it was not until 1970 that Boswell's dissertation work led to a discovery that a high, dense plasma source could be generated by exciting helicon waves [62,63]. Since then, numerous experimental and computational investigations of the properties and physics of helicon plasma sources have been studied [22, 25, 64–70]. A helicon plasma source has advantages similar to an inductive plasma source (electrodeless system and high density plasma), but its density does not have the same limitation as an inductive plasma source ($10^{17} - 10^{18}$ m^{-3}). In addition, in contrast to ECR sources, a helicon plasma source does not require a high magnetic field.

Chen [64] derived the dispersion relation for helicon waves as follows. From linearized Maxwell's equations, in particular:

$$\nabla \times \vec{E} = -\frac{\partial \vec{B}}{\partial t} \tag{3.23}$$

$$\nabla \times \vec{B} = \mu_o \vec{J} \tag{3.24}$$

and

$$\vec{E} = \vec{J} \times \frac{\vec{B}_o}{en_o} \tag{3.25}$$

where all the values without a subscript ($\vec{E}$, $\vec{B}$, and $\vec{J}$) are perturbed values, and n_o and $\vec{B}_o$ are equilibrium values. Chen arrived at the dispersion relation for the helicon waves after solving the Besel's function for m=1 mode as:

$$\frac{B_o}{n_o} = \frac{e\mu_o R}{3.83}\left(\frac{\omega}{k}\right) \tag{3.26}$$

where R is the radius of the discharge, and k is the wave number. In arriving at this dispersion relation, it was assumed that $\omega_{LH} \ll \omega \ll \omega_{ce}$, where ω_{LH} is the lower hybrid frequency. By assuming that $\omega_{LH} \ll \omega$, the ion motion is neglected. And by assuming $\omega \ll \omega_{ce}$, the electron cyclotron motion is also neglected because it is too fast compared to the operating frequency. Equation 3.26 reveals an important relationship between the dimensions of the discharge and the magnetic field required and the wave number (therefore wavelength). This relationship can be used to design a helicon discharge.

In a helicon plasma discharge, low-frequency whistler waves are confined to an insulating cylinder with an applied DC magnetic field. In addition to collisional heating, Landau damping and Trivelpiece-Gould modes coupling have been attributed to the efficient transfer of the wave energy to the electrons [65, 67]. Although the exact mechanism of energy transfer is still a subject of debate, it is believed that electrons gain energy from the helicon mode as it propagates along the column by collisional or collisionless (Landau) damping [52]. Collisional heating takes a more significant role only at higher pressures. In Landau damping, the energy of a wave is transferred to electrons which have velocities near the phase velocity of the wave [52, 66].

3.3.5 Benefits of Radio-Frequency Plasma Sources

Sections 3.2 and 3.3 describe the methods of plasma production and some main types of plasma discharges. The RF plasma sources (capacitive, inductive, and helicon) in general can produce higher plasma density, and at a higher efficiency than DC plasma sources. Within the choices of RF plasma sources, inductive sources can produce higher plasma density than capacitive sources, but helicon plasma sources can produce an even higher density and more efficiently. The selection of the discharge for this dissertation work depends on several criteria and a helicon-type discharge was chosen due to its versatility. A helicon-type discharge can operate in capacitive, inductive and/or helicon modes and furthermore, it was chosen for the following reasons:

Electrodeless: A radio-frequency plasma source as used in this work is an electrodeless system. In a water plasma source, presence of highly reactive radicals and water molecules can destroy the electrode. Thus, an electrode-less system is necessary for this application.

High n_e*:* Radio-frequency plasma sources are known to produce among the highest electron number densities. As this method of hydrogen production relies on electron impact

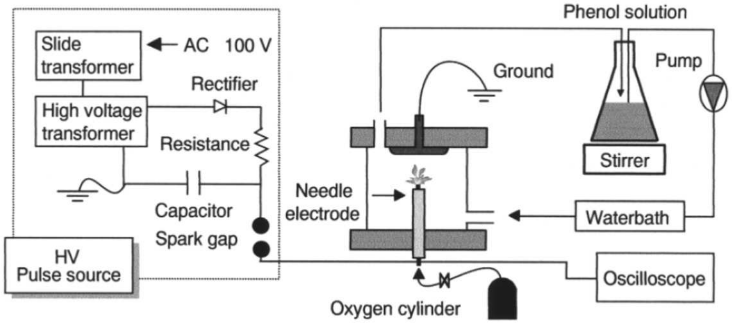

Figure 3.8: Experimental setup to study decomposition of phenol solutions [12].

collisions, higher electron density is favorable.

Efficiency: Radio-frequency plasma sources, particularly those operated in inductively-coupled or helicon modes can generate high plasma density very efficiently.

3.4 Water Plasma Studies

Water plasmas have gained widespread utility in many fields. This section reviews applications of water plasmas in a variety of areas including for hydrogen production.

3.4.1 General Applications of Water Plasma

Plasma discharges operated on water–in either liquid or vapor form–can be used in a wide range of applications [11–21]. For example, the decomposition of organic contaminants in waste water, such as phenol, into more benign byproducts first started by seminal work by Clements [11]. For example, Figure 3.8 shows a setup of an experiment to study the decomposition of phenol solutions in a water plasma.

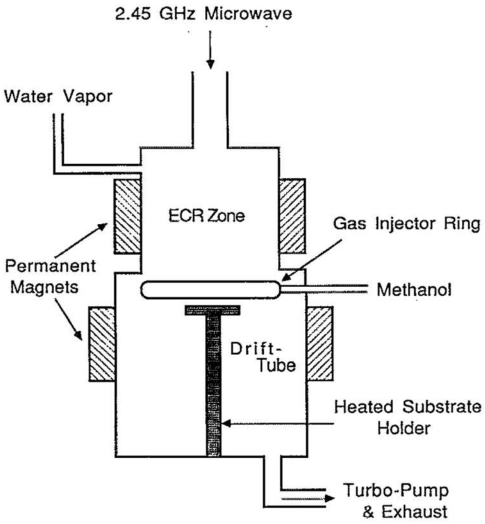

Figure 3.9: Experimental setup to study diamond growth in a water plasma source [17].

In addition to directly generating a discharge in liquid water, one can also generate a plasma from water vapor. In the intermediate pressure regime between tens of mtorr to one torr, water vapor plasmas are now widely used in plasma-assisted chemical vapor deposition for diamond film formation. Currently, CH_4 and H_2 are injected into a plasma chamber to fabricate diamond films [16, 17]. When O_2 is introduced, the presence of O_2 and OH radicals is stipulated to increase the rate of diamond growth. Instead of injecting O_2 and H_2 separately, other researchers have shown that the addition of H_2O vapor in the main gas feed favorably contributes to diamond growth rate. Furthermore, water is easier to handle and is essentially cost-free. Figure 3.9 shows an experimental setup of a work led by Singh [17] in which water with the addition of methanol is used to study diamond growth.

Ultraviolet (UV) light source plasma is another example of an application of water vapor plasma. UV light sources have widespread applications. As an example, Hg vapor is the current working gas in fluorescent lamps to produce UV radiation. UV lamps are also used to sterlize tools in laboratories and hospitals. However, the current method uses Hg vapor to generate the UV light source. Water vapor plasma as UV light sources can replace current Hg lamps, mainly because water vapor is easier to handle than Hg. Also, water vapor does not have the harmful effects that Hg vapor has on human. Recently, Oh *et al.* investigated the potential application of water vapor plasmas excited by microwaves as a UV light source [20].

Lastly, water plasma is observed to have played an important role in an emerging field of plasma medicine where an interest in applications of non-thermal (non-equilibrium) plasma is growing [21, 71]. In plasma medicine's nascent stage, reactive oxygen species (O and OH) are shown to have the ability to inactivate various organisms. This can be applied in sterilization of medical instruments [71]. For example, one can envision that after medical instruments are washed, they can be placed directly into a plasma discharge. The working gas of this discharge would be the water that remained on the wet instruments. For this application to be utilized, the cost of the system must be reduced. In particular, the plasma source must be able to operate at atmospheric pressure to reduce any pumping systems, hence additional cost. In addition, biological systems are composed of water, and therefore a plasma can be produced within these environs. Water plasma has many potential applications and is emerging rapidly in the medical plasma research community because it contains an abundance of reactive species such as OH^-, $O_2{}^-$ and H. A good review of current research in plasma medicine is given in References 53 and 21.

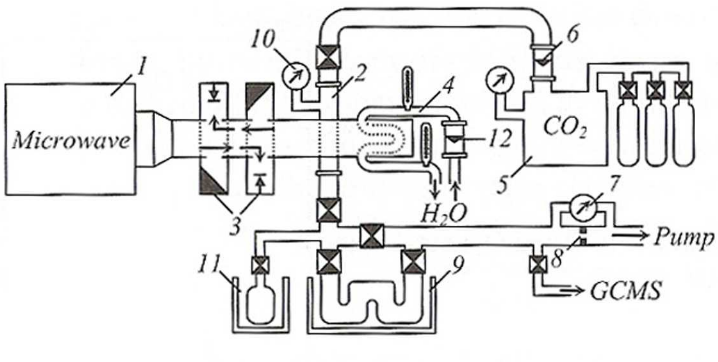

Figure 3.10: Experimental setup to study CO_2 dissociation [53].

3.4.2 Plasma Electrolysis

There are other plasma methods for hydrogen production, such as plasma catalytic reforming of natural gas [72,73]. However, this literature review only focuses on applications of plasma to directly dissociate water molecules for hydrogen production.

For direct dissociation of water molecules for hydrogen production, the first known published work is by V.K. Givotov from I.V. Kurchatov Institute of Atomic Energy in 1981 from Moscow [74, 75]. Initially, this group investigated the direct dissociation of CO_2 in a microwave plasma discharge as shown in Figure 3.10. The plasma discharge operated typically at 2.4 GHz at 1.5kW, and the diameter of the quartz tube was 28 mm [53]. The typical pressure was 50-100 torr. This plasma source was later used to study water dissociation with a flow rate of 0.05–0.6 g/s (4–48 slm).

The energy efficiency achieved from this work was reported to be 30–40% [74]. This group also investigated dissociation using other discharge methods. The glow discharge was used and the energy efficiency reached 12–20%, lower than the microwave discharge.

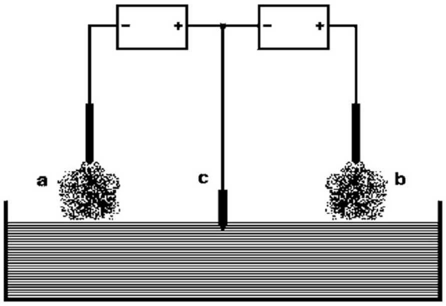

Figure 3.11: Experimental setup to study hydrogen production in a water plasma source [5].

In addition, a glow discharge with a hollow cathode was also used, with an energy efficiency of 2%. The power level was 1–300 W and the pressure range was 0.4–4 torr.

In addition, Chaffin *et al.* dissociated water by placing electrodes above a liquid water surface, as shown in Figure 3.11 [5]. Chaffin's method mimics electrolysis, but uses electrodes that are conventionally used in a plasma discharge instead of using a membrane separation method.

Chaffin argues that the widespread adoption of conventional electrolysis systems has a physical limitation. In these systems, hydrogen must diffuse in liquids, but its diffusion rate in a liquid is slower compared to its diffusion rate in a gas [5]. Chaffin suggested that in using plasmas, the cost of electrolytes and catalysts required in conventional electrolysis can be removed and attributed the presence of high-energy electrons as the key in electrolyzing water.

3.5 Summary

In summary, this chapter begins with an overview of the plasma physical processes in water vapor discharge. Then, the method of plasma production and several types of plasma sources are discussed. Lastly, a survey of water plasma studies are provided, first with the general applications followed by electrolysis applications of water plasma.

Chapter IV

Experimental Setup and Diagnostics

This chapter describes the experimental set-up including the vacuum chamber, the water feed system, and the plasma discharge. It also describes the diagnostics employed in this work: residual gas analyzer (RGA), Langmuir probe, and optical emission spectrometer.

4.1 Experimental Setup

4.1.1 Vacuum Chamber

Testing of the water vapor RF plasma source was performed at the Plasmadynamics and Electric Propulsion Laboratory (PEPL) in the Cathode Test Facility (CTF). The vacuum facility was a cylindrical aluminum chamber that is 2.44 m in length and 0.61 m in diameter. An Edwards XDS 35i dry scroll pump was used to evacuate the chamber. Unlike oil-based vacuum pumps, dry scroll pumps are essentially oil-free and can therefore be operated in water vapor-rich environments. With a maximum pumping speed of 35 m^3/hr on N_2 [76], the base pressure achieved was below 3 mtorr. The plasma source was attached to a 15-cm-

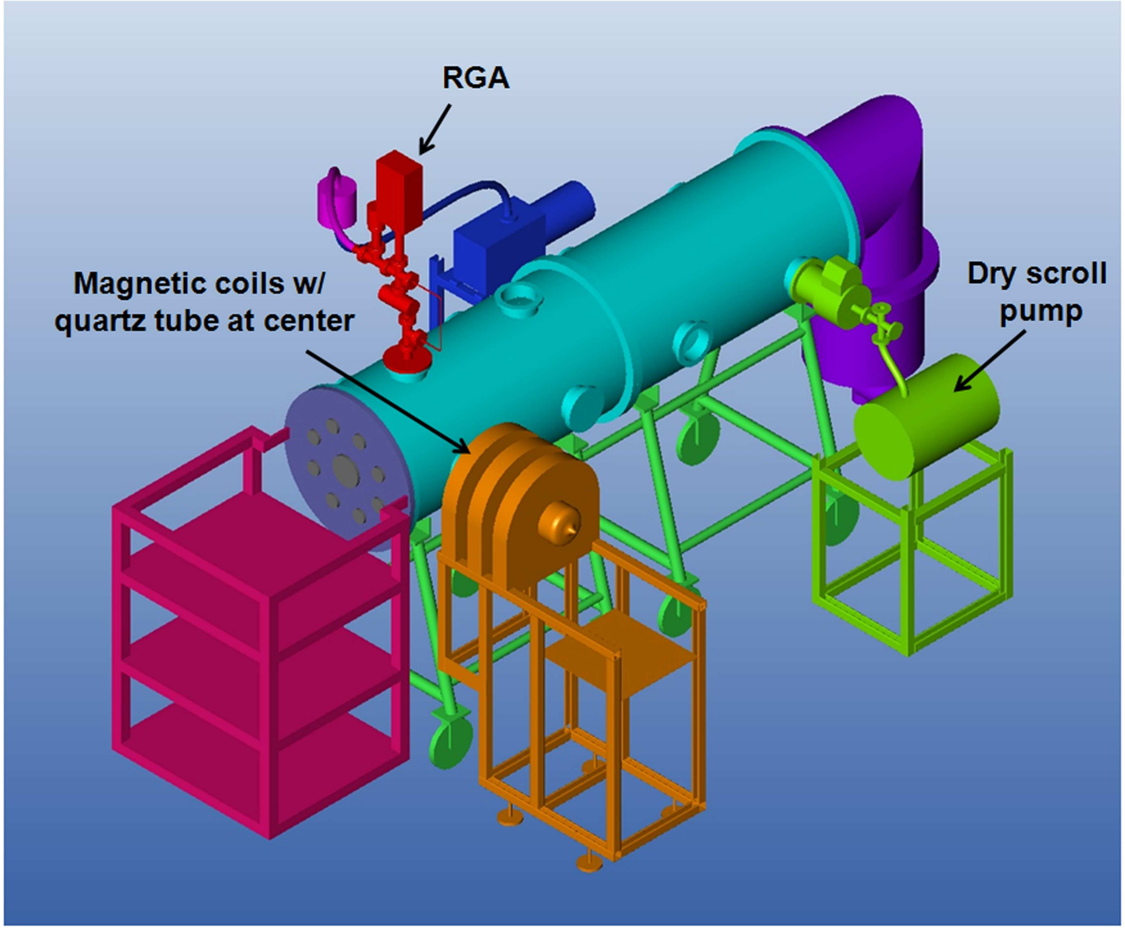

Figure 4.1: Drawing of vacuum facility

diameter side port on the CTF. A CAD drawing of the vacuum facility is shown in Figure 4.1.

In addition, the vacuum facility is also fitted with a CVI model CGR 411-LS cryogenic pump that can achieve a base pressure below 10^{-6} torr. For gases such as argon, within a reasonable flow rate these cold surfaces can maintain a temperature approximately 14-20 K and the cryopump can run for hours. When water vapor is introduced into the chamber, water vapor contaminates the charcoal surface of the cryogenic pump and light gases such as hydrogen can no longer be pumped.

4.1.2 Plasma Source

Figure 4.2 shows a photograph of the plasma source assembly and Figure 4.3 shows a photograph of the plasma source. The source consisted of a 15-cm-diameter quartz tube that was 50 cm in length. Three magnetic coils connected in series to a Lambda EMI-EMS 40-V, 60-A DC power supply produced a peak axial magnetic field on axis of approximately 200 G and 400 G at 30-A and 60-A magnet current, respectively. The magnetic field was measured by a 3-axis Hall probe that was connected to a 3-channel Gauss meter from Lakeshore (model 460). The mapping was achieved by placing the Hall probe on three-axis motion control system. Figure 4.4 shows the mapping of the magnetic field for the 60-A magnet current setting in the horizontal plane of the quartz tube at the centerline, with an outline of the quartz tube and the flange that is used to connect the quartz tube to the CTF vacuum chamber. The magnetic field mapping for a magnet current of 30 A is exactly identical to that at 60 A, with the exception that the magnetic field strength is reduced in half.

A double helical (m = 1 mode) antenna circumscribed the quartz tube, and was sandwiched between the quartz tube and the magnetic coils, as shown in Figure 4.5. A PlasmaTherm 13.56-MHz RF power supply was used to excite the antenna up to 1.5 kW. A π-style, water-cooled, 5-kW matching network purchased from Manitou Systems Inc. was employed to match the impedance of the RF power supply output with the impedance of the plasma, reducing the reflected power to less than 5% of input power for all conditions investigated. More details on the plasma discharge can be found in Reference 25.

The assembly, as shown in Figure 4.2, was housed in a Faraday cage including the en-

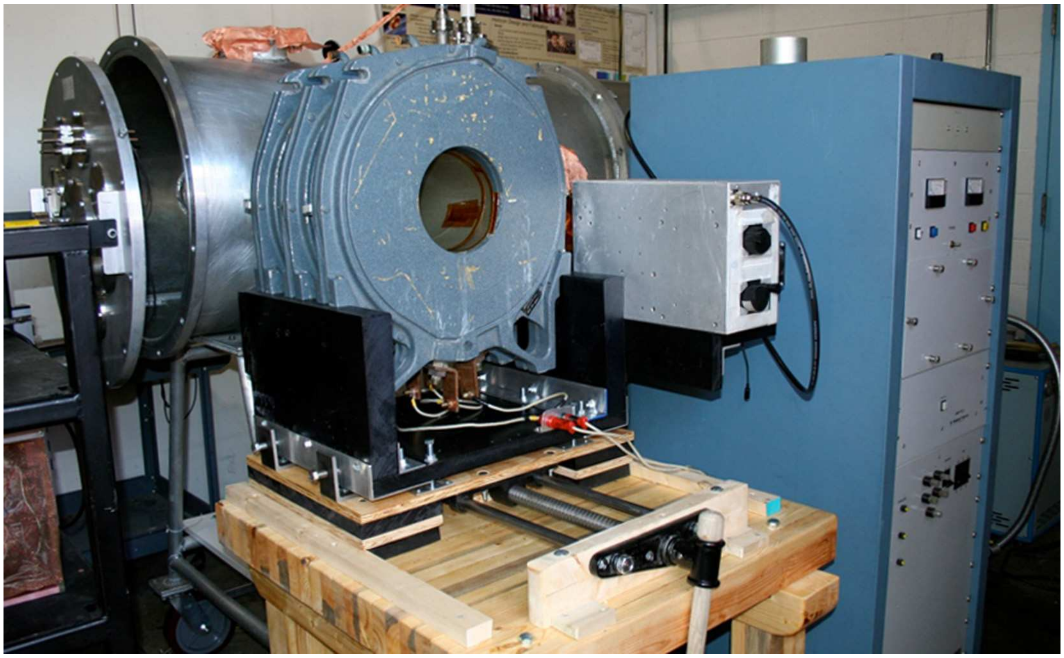

Figure 4.2: Photograph of setup including the magnetic coils, matching network, and the RF power supply

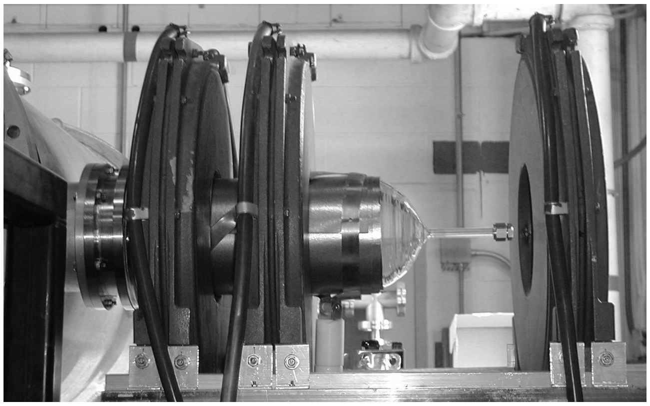

Figure 4.3: Photograph of plasma source at PEPL. Plasma source shown attached to the CTF vacuum chamber at PEPL with one magnet pulled away to show antenna and quartz tube.

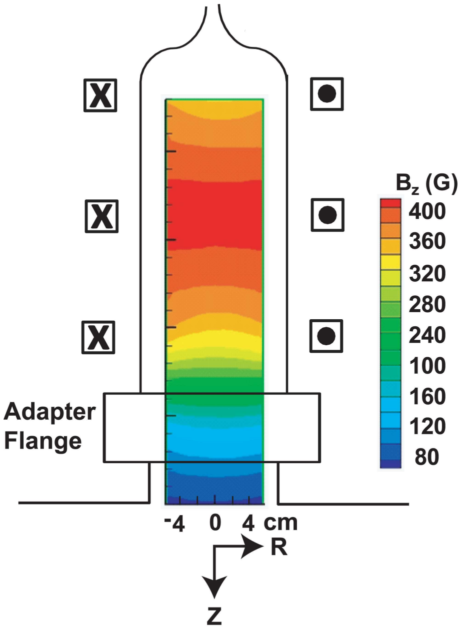

Figure 4.4: Mapping of magnetic field at 60-A magnet current with an outline of the quartz tube and an adapter flange.

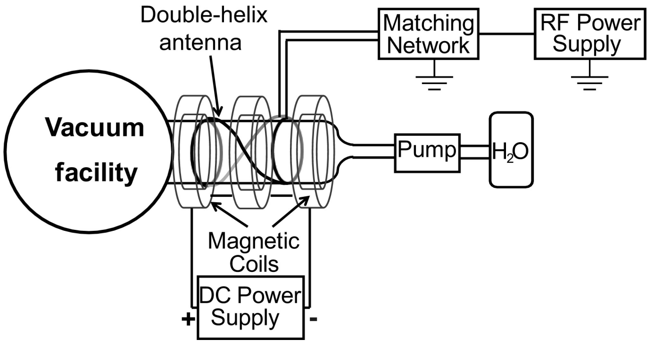

Figure 4.5: Schematic diagram of plasma source.

tire RF system: the quartz tube, the magnetic coils, the matching network, and importantly the RF power supply. The Faraday cage was built from very fine copper mesh with a hole size of a few mm to prevent RF interference on diagnostic sensors and computer systems throughout the lab.

4.1.3 Water Feed System

An Eldex water pump–a positive displacement, reciprocating piston pump–with a flow rate range of 12.5 sccm - 25,000 sccm H_2O was used to meter liquid water into the plasma source. A back pressure regulator from Upchurch Scientific was placed in the gas line between the water pump and the vacuum chamber to maintain a pressure of 250 psi. In this work, the vacuum chamber background pressure ranged between 50 and 500 mtorr. In this pressure range and at room temperature, water is in the vapor phase. Therefore, a small amount of liquid water (up to 125 sccm) injected into the plasma discharge was immediately vaporized. Nonetheless, the line between the water pump and the quartz tube was heated with heating tape up to 400 K to ensure that water molecules were not condensed onto the metal surface of the feed line and that water remained in vapor state upon entry into the plasma source. De-ionized water was used. The water passed through a 10-μm filter before reaching the pump. The filter was used as a precaution to prevent any particulate from entering the gas line. Figure 4.6 depicts the layout of the water delivery system. As shown, water delivery system was placed outside of the Faraday cage, and was connected to the quartz tube inside the cage via a ceramic-to-metal adapter to electrically isolate the gas feed lines from the RF system.

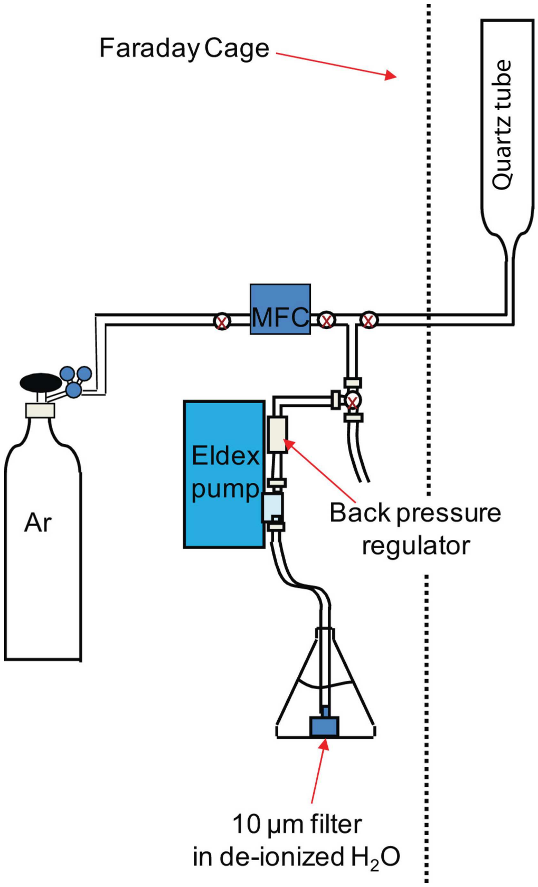

Figure 4.6: Schematic diagram of water delivery system.

In addition to the water pump, a low-flow 10 sccm Celerity (UNIT 7300 model) and a high-flow 2 slm Celerity (also UNIT 7300 model) mass flow controllers were used to regulate flow of argon, hydrogen, and oxygen gases when flow of those gases were needed. The need to flow argon and the process of calibrating the RGA using hydrogen and oxygen gases are discussed in Section 4.2.1.

4.2 Diagnostics

In this investigation, Langmuir probe data were used to determine plasma properties for both argon and water vapor discharges. The optical emission spectrometer was used to identify the presence of excited hydrogen and hydroxyl in the discharge to confirm water dissociation. The RGA was also used to identify, as well as, to make quantitative estimates on the concentration of hydrogen, oxygen, hydroxyl, and water in the discharge.

4.2.1 Residual Gas Analysis System

A commercial residual gas analyzer–Stanford Research Systems RGA100–was used in this work to identify gas species inside the chamber. The residual gas analyzer (RGA) system as shown in Figure 4.7 is a mass spectrometer consisting of an ionizer, quadrupole probe, and an electronic control unit. When gas molecules enter the RGA, some are ionized by the ionizer. A combination of RF and DC voltages are applied to the quadrupole probe to select ions with a certain mass-to-charge ratio to pass through the probe system. The RGA varies the RF and DC applied to the quadrupole rods to sweep through the entire spectrum of mass-to-charge ratio which ranges between one and 100 AMU (Atomic Mass

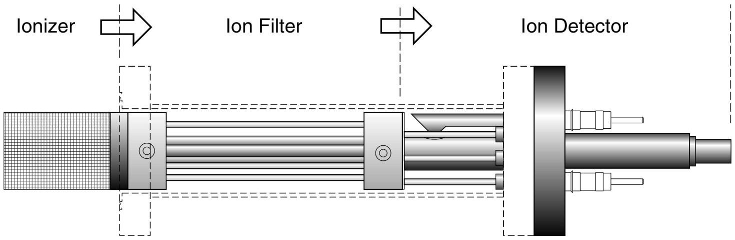

Figure 4.7: Components of the RGA, courtesy of SRS [77].

Unit). After passing through the probe filter, the ions are focused on an ion detector, and an electrometer is used to measure the analog current.

The RGA was designed to operate with a maximum allowable pressure of 10^{-5} torr, significantly lower than background pressure of up to 500 mtorr in this experiment. Therefore, a differential pump system was utilized to reduce the pressure to allow for RGA operation. Figure 4.8 depicts the layout of this system. A variable leak valve isolated the RGA chamber from the plasma chamber. A 70-l/s Varian turbopump was used to evacuate the RGA chamber to achieve a base pressure below 10^{-7} torr. The turbopump was backed by a mechanical pump from Edwards, E2M30 [78].

Without a proper calibration, the RGA only yields qualitative information, such as the presence of certain gas species in the plasma. To quantitatively estimate the amount of hydrogen, oxygen, and hydroxyl produced in the plasma, the RGA was calibrated for each gas individually by injecting a known amount (10 sccm) of argon and a varying amount of the gas of interest; *i.e.* hydrogen or oxygen. For example, to calibrate hydrogen, a mass flow controller was used to meter the flow rate of hydrogen into the chamber while a different mass flow control was used to meter a fixed (10 sccm) flow rate of argon. The partial pressures of argon and hydrogen were recorded for each flow rate setting of hydrogen.

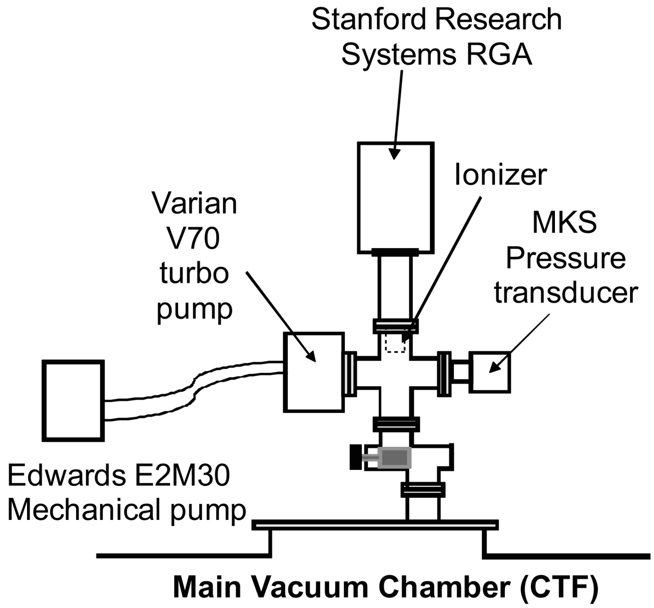

Figure 4.8: Differential pump system for the RGA including a variable leak valve, 70 l/s turbo pump, and pressure transducer.

A calibration factor (CF) (Equation 4.1) relating the ratio of the partial pressure of the gas of interest to the partial pressure of argon could therefore be obtained from the ratio of the flow rates of the two gases.

$$\frac{P_i}{P_{Ar}} = CF\frac{\dot{m}_i}{\dot{m}_{Ar}} \tag{4.1}$$

where P_{Ar} is the partial pressure of argon, P_i is the partial pressure of the gas of interest, $\dot{m}_{Ar}$ is the known mass flow rate of Ar, and $\dot{m}_i$ is the rate of production of the gas of interest.

The same procedure was followed to calibrate the oxygen and water flow rates detected by the RGA. Figure 4.9 shows the calibration curves of hydrogen, oxygen, and water. The pressure ratio varies linearly with mass flow rate ratio as expected. Note that even though the flow rate of water vapor injected into the system was known, this calibration was later

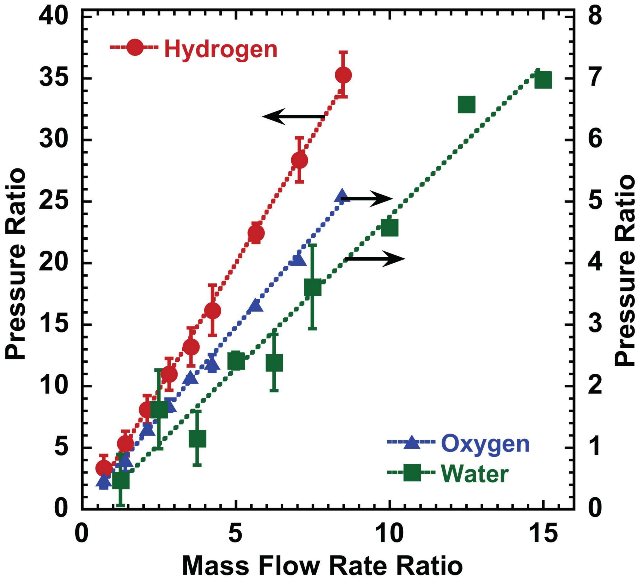

Figure 4.9: Calibration curves for hydrogen, oxygen, and water relating the RGA partial pressure ratio to the flow rate ratio.

used to determine the quantity of undissociated water molecules in the discharge. When two gases were being injected into the system, the water pump as shown in Figure 4.6 was replaced by a mass flow controller.

With CF known for each gas, the mass flow rate of a gas of interest produced in the water vapor plasma source is estimated following Equation 4.2.

$$\dot{m}_i = \frac{\dot{m}_{Ar}}{CF} \frac{P_i}{P_{Ar}} \tag{4.2}$$

As shown, the mass flow rate of the gas of interest can be determined if a known amount of argon is injected into a multiple species plasma. The mass flow rate of a gas is determined when the CF and the mass flow rate of argon are known and the partial pressures of the gas of interest and of argon are obtained from the RGA.

Unlike the case of hydrogen or oxygen, hydroxyl (OH) is highly reactive and short-lived, and therefore it is not a commercially available gas that can be used to calibrate the production of hydroxyl in the plasma discharge. To estimate the flow rate of OH produced in the plasma, the calibration factor for O_2 was used. Between the three choices of calibration factor that are available (hydrogen, oxygen, and water), hydroxyl most closely resembles oxygen. The hydrogen gas is too low-mass and the water vapor is not as reactive as the hydroxyl. Therefore, a choice was made to use the calibration factor of oxygen because they both are reactive and have the same order of magnitude in mass. As a consequence, the OH production rate reported in this work is only used to study the trend in OH production, not necessarily to assess its precise production rate.

Effects of the addition of argon to the plasma properties and hydrogen production was also studied. The addition of 10-sccm Ar to calibrate the RGA is shown to have a negligible effect on the plasma. As can be seen in Figure 4.10, the rates of hydrogen production for the addition of 5-sccm and 10-sccm Ar are almost identical at all RF power levels except for 750 W. Even at this power level, however, the two results are within the uncertainty of the measurement technique. Furthermore, Figures 4.11 and 4.12 illustrate the invariance of electron density, ion density, plasma potential, and floating potential with argon flow rate.

For the RGA results, the sample size is four sets of three spectra, and the error bars also represent one standard deviation of spread in each set of measurement. Based on the calibration of the RGA, the error for determining hydrogen and oxygen production is 5–10%, and for determining water vapor flow rate is 10–20%.

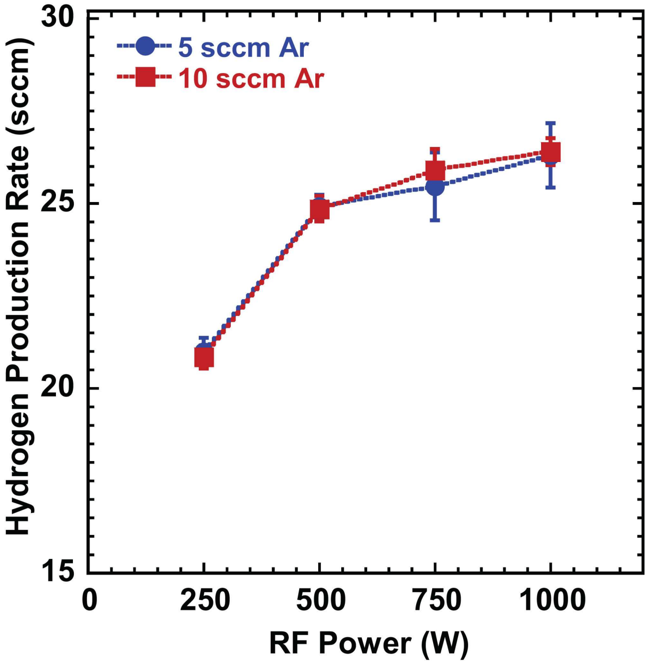

Figure 4.10: Effect of argon flow rate on hydrogen production for 75-sccm H_2O with 5-sccm and 10-sccm Ar operating with 30-A magnet current.

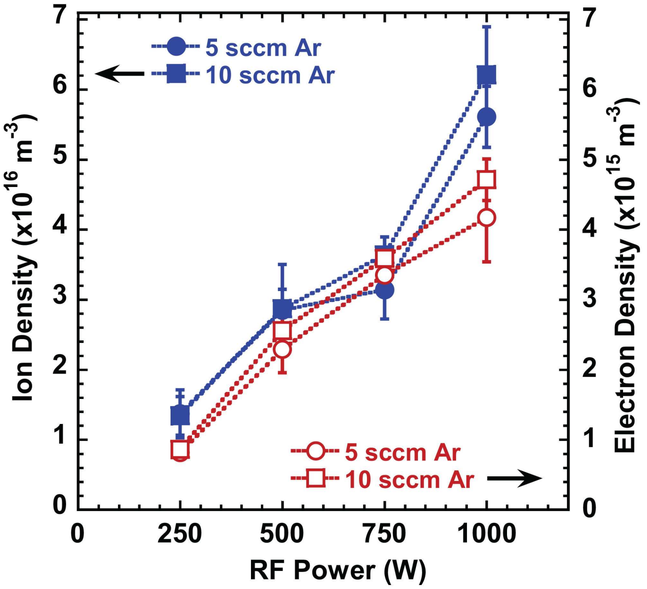

Figure 4.11: Effect of argon flow rate on ion and electron densities for 75-sccm H_2O with 5-sccm and 10-sccm Ar operating with 30-A magnet current.

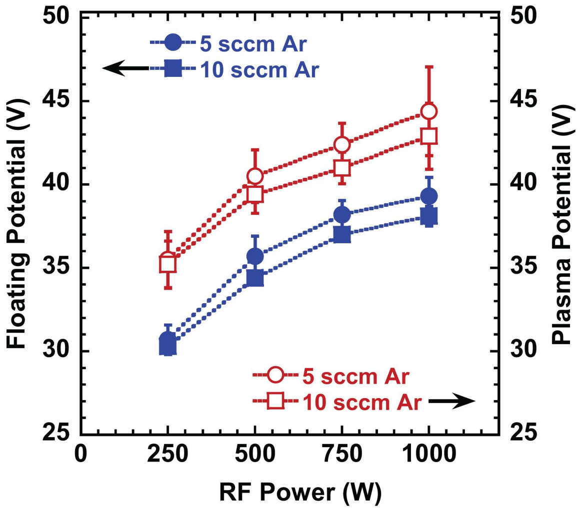

Figure 4.12: Effect of argon flow rate on floating and plasma potential for 75-sccm H_2O with 5-sccm and 10-sccm Ar operating with 30-A magnet current.

4.2.2 Langmuir Probe

Langmuir probe is used to determine plasma properties such as density, electron temperature, and floating and plasma potentials. It was first coined by Irving Langmuir [79,80] in 1926 and has been used widely by the plasma research community. The Langmuir probe in its basic form is a conducting tip that is electrically isolated from its probe holder. The Langmuir probe system together includes the conducting probe tip, an external power supply, and an ammeter. The ammeter measures the current to the probe and the power supply sets the bias voltage on the probe. Consequently, a current-voltage (IV) curve is obtained for each sweep.

A typical IV curve is shown in Figure 4.13. When the applied voltage is set at a value that results in a zero net current to the probe ($I^+ = I^-$), then the value of the applied voltage is known as the floating potential. The region where the applied voltage is below the floating potential is the ion collection region. In this region, positive ions are attracted

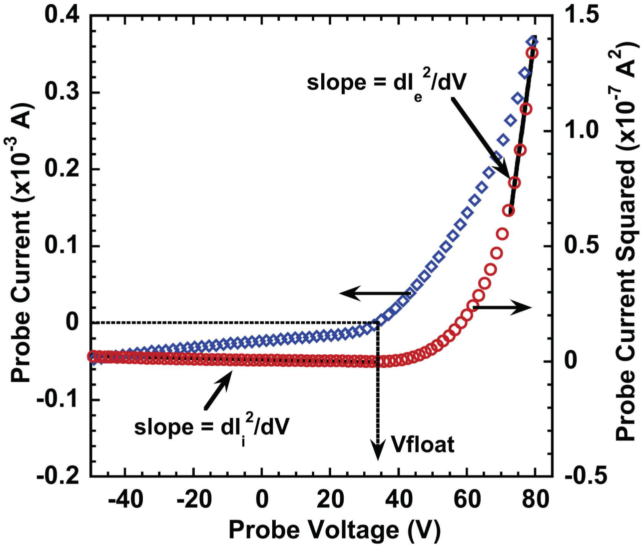

Figure 4.13: (◇) A typical Langmuir probe curve for water vapor plasma operating with 75-sccm H_2O and 10-sccm Ar at 500-W RF power and 30-A magnet current. (○) Probe current squared versus voltage for the same plasma, indicating the slopes in the ion and electron saturation regions taken to calculate ion and electron densities, respectively.

to the probe while electrons and negative ions are repelled. At a sufficiently large negative applied potential, all the electrons are repelled and the probe only collects the available ion current as established by sheath conditions. This current is known as the ion saturation current. On the other hand, if the applied voltage is higher than the floating potential, the electrons and negative ions increase in number that can be collected at the probe. Similarly at a sufficiently large positive applied potential, only electrons are collected by the probe, and the collected current is referred to as the electron saturation current.

A commercial RF-compensated single Langmuir probe (LP) system from Hiden Corporation is used in this experiment to determine plasma density, floating potential, plasma potential, and electron temperature. This commercial system includes a data acquisition software package, RF compensation circuitry, a driver power supply and an ammeter. The LP collector is 0.12 mm in diameter and 3 mm in length. The probe was placed at the axis of symmetry and just downstream of the plasma source axially.

Langmuir probe analysis falls into two main categories (collisionless or collisional), depending on the ratio of the local electron and ion mean free paths and the Debye thickness (λ_D) [81]. This ratio represents the dimensionless Knudsen number:

$$Kn = \frac{\lambda_{i,e}}{\lambda_D} \tag{4.3}$$

where Kn is the Knudsen number, $\lambda_{i,e}$ is the local ion and electron mean free path, and λ_D is the Debye thickness.

For a background gas pressure between 50 and 500 mtorr, the neutral number density ranges between 10^{21} and 10^{22} m^{-3}. The maximum value for electron and ion density is below 10^{17} m^{-3}; therefore, collisions are likely to occur between a neutral and an electron or ion instead of between charged particles. The local mean free path of the electron and ion is:

$$\lambda_{i,e} = \frac{1}{\sqrt{2}\sigma n} \tag{4.4}$$

where σ is the collisional cross section ($\approx 8.8 \times 10^{-21}$ m^{-2}) and n is the neutral density.

The Debye length is calculated from:

$$\lambda_D = \sqrt{\frac{k_B T_e \epsilon_o}{ne^2}}, \tag{4.5}$$

Although the operating pressure for this investigation can be up to 500 mtorr, the local electron and ion mean free paths are found to range between 3.2 and 32 mm, which is sufficiently higher than the Debye length, which is approximately 0.4 mm. Therefore, the collisionless probe model is applied for LP analysis in this experiment.

Due to the presence of an applied magnetic field in the plasma, magnetic effects were examined for the Langmuir probe analysis. Even though the maximum peak of the magnetic field strength is 200 G and 400 G for an applied magnet current of 30 A and 60 A, the LP data are collected in the region downstream of the quartz tube. There, the magnetic field strength is reduced significantly to only 40 G and 80 G for 30-A and 60-A applied magnet current, respectively. In the presence of the magnetic field, both electrons and ions gyrate along the field lines. To determine if the magnetic field affects the current collected by the LP probe tip, the cyclotron radius of the electrons:

$$r_c = \frac{v_\perp}{|\omega_c|}, \tag{4.6}$$

are compared with the probe radius (0.06 mm) and the Debye length (Equation 4.5). To calculate the electron cyclotron radius, the magnitude of the perpendicular velocity ($v_\perp$) is approximated as the average electron speed:

$$\bar{v}_e = \sqrt{\frac{8eT_e}{\pi m}} \tag{4.7}$$

For electron temperature between 1 and 3 eV, electron density between 5×10^{15} and 10^{16} m^{-3}, and magnetic field 40 and 80 G, the electron cyclotron radius is between 0.4 mm and 1.5 mm. The Debye length is between 0.02 and 0.18 mm.

In general, the electron cyclotron radius is always greater than the probe radius and the Debye length. Therefore, the magnetic effects on the LP can be neglected.

Figure 4.13 shows a typical current versus voltage (IV) Langmuir probe curve and Figure 4.14 shows the same data in semi-log plot. The LP date files were imported and were analyzed in MATLAB. As shown, the floating potential is obtained directly from the IV trace, the value of the bias voltage where the net current to the probe is zero. The electron current is obtained from the IV characteristic data by subtracting the ion current from the measured current in the electron collection region. The effect is shown in Figure 4.14, where the linear region is further extended when the ion current is subtracted. The electron temperature is derived from the slope of the semi-log plot, and the plasma potential is taken to be the bias voltage where the two lines intersect in this semilog plot, as shown in Figure 4.14.

Within the collisionless model of the LP analysis, the ion density is calculated in two ways based on the ratio of the probe radius and the Debye length, r_P/λ_D. Figure 4.15 shows a flow chart of the LP analysis routine. First, a thin sheath ($r_P/\lambda_D > 10$) is assumed and the ion density is calculated as follows [81].

$$n_{i,sat} = \frac{I_{i,sat}}{0.61 A_s e}\sqrt{\frac{M_i}{eT_e}}, \tag{4.8}$$

where n_i is the ion density, e is the electron charge, A_s is the sheath surface area, $I_{i,sat}$ is the ion saturation current, and T_e is the electron temperature. In this work, an effective ion mass, M_i, is calculated from a weighted average of the product of mass (m_i) and partial

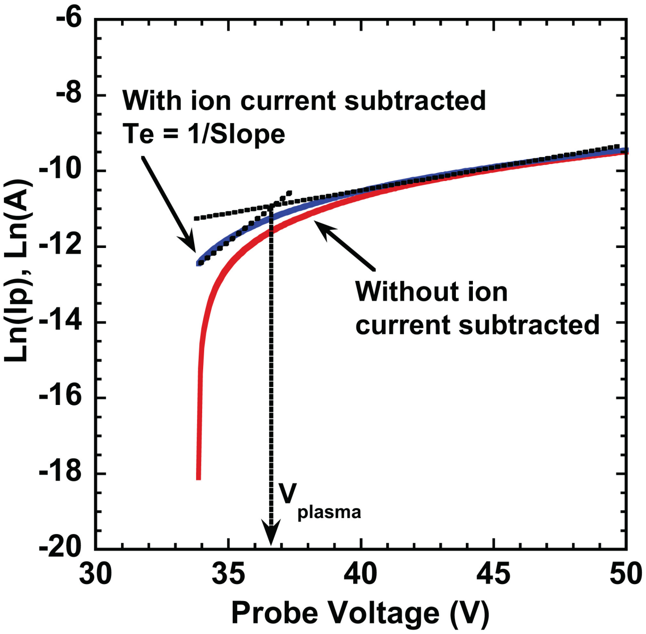

Figure 4.14: Semi-log plot of Langmuir probe trace showing the linear region where electron temperature is calculated and the point at which the plasma potential is derived.

pressure (p_i) obtained from RGA data.

$$M_i = \frac{\sum_i m_i p_i}{\sum_i p_i} \tag{4.9}$$

After an estimated ion density is obtained, the Debye length is calculated, and the effective probe area is calculated following the derivation in Hutchinson [82]. The new ion density is calculated based on the effective probe area and the Debye length is recalculated to account for the new ion density. As such, the effective probe area, ion density, and Debye length are interdependent. In Figure 4.15 the steps in calculating the ion density are outlined. A loop is applied for steps 7 through 9. After a converged solution is obtained for the ion density, the ratio of probe radius to Debye length, r_P/λ_D, is calculated. If the ratio is greater than 10, the previously assumed thin-sheath analysis is used and ion density

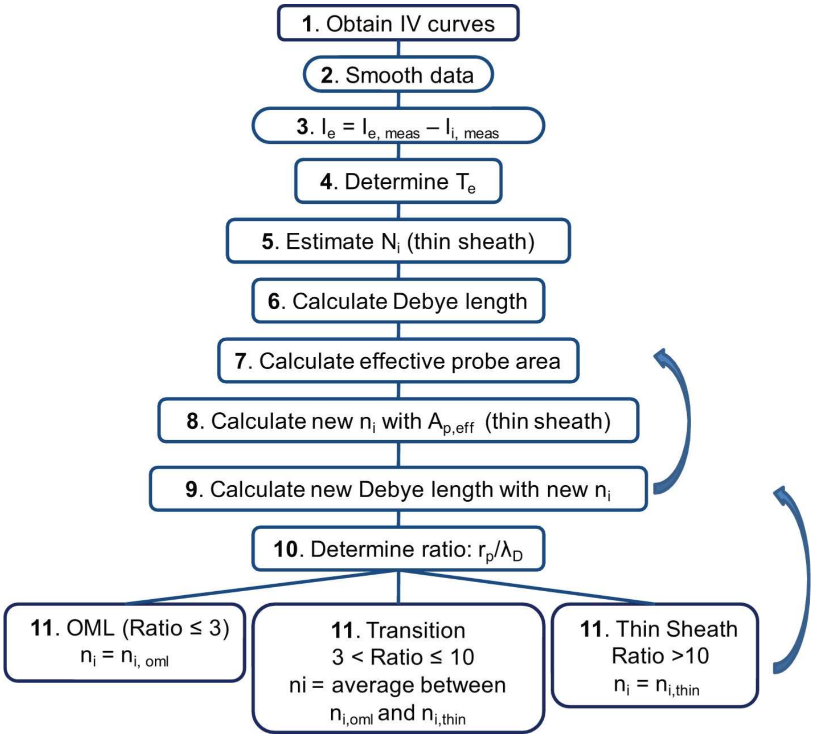

Figure 4.15: Flow chart for Langmuir probe analysis – ratio = r_p/λ_D

is the ion density obtained in step 9.

However, if the ratio is less than three, the ion number density is calculated using the orbital motion limited (OML) analysis model [81, 83–85]. In a thick sheath, orbital motions limit some of the particles that enter the sheath from hitting the probe. The current to the probe in this case is independent of the size of the sheath surrounding the probe. Laframboise derived a method to determine the ion number density in this regime assuming that the plasma is collisionless, stationary, and isotropic [83, 84]

$$n_i = \frac{\pi}{A_p}\sqrt{\frac{M_i}{2e^3}\left(\frac{dI_i^2}{dV}\right)} \tag{4.10}$$

In Equation 4.10, A_p is the surface area of the probe, and dI_i^2/dV is the slope of current squared versus the bias voltage for ions as shown in Figure 4.13.

If the ratio is between 3 and 10, a weighted average density between the two methods is used. Again, the Debye length and ion number density are interdependent, therefore a loop is applied for steps 9 through 11.

Despite this laborious effort to ensure that the ion density was calculated appropriately within the right regime, it was determined that only OML analysis was needed because the probe radius is sufficiently small that the ratio r_P/λ_D is always less than three.

For argon plasma, quasineutrality is assumed, hence $n_i \simeq n_e$. However, because of the presence of negative ions in the water plasma, quasineutrality in this case requires that $n_{i+} \simeq n_e + n_{i-}$, where n_{i+} and n_{i-} are positive and negative ions. The electron density is calculated separately, using Equation 4.11:

$$n_e = \frac{\pi}{A_p}\sqrt{\frac{m_e}{2e^3}\frac{dI_e^2}{dV}} \tag{4.11}$$

In Equation 4.11, dI_e^2/dV is the slope of current squared versus the bias voltage for the electrons as shown in Figure 4.13.

Results given in this dissertation are the mean values of a sample of measurements. Error bars represent one standard deviation among the spread in the measurements sampled. For the Langmuir probe data, the sample size includes four sets of 5 to 10 Langmuir probe traces. The measurement is taken in a random order of RF power. While the absolute error in the Langmuir probe diagnostics is 20–30% for electron temperature and 50–60% for plasma densities [82], the relative error from point to point is small, which allows for a

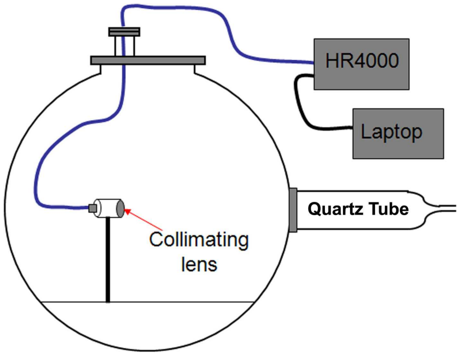

Figure 4.16: Diagram of the spectrometer setup, showing light is collected by the collimating lens and is transferred to the spectrometer via a fiber optic cable.

study of trends in plasma properties.

4.2.3 Spectrometer

In addition to the RGA, two spectrometers from Ocean Optics are used to obtain optical emission spectra from the plasma: USB2000 and HR4000. The USB2000 model spectrometer has a 25 μm entrance slit and a detector wavelength range of 200-850 nm. The HR4000 model spectrometer has a 5 μm entrance slit and a detector wavelength range of 400-850 nm. A collimating lens is used to focus light into a fiber optic cable that is connected to the spectrometer via a SMA connector. Figure 4.16 shows this setup in the vacuum chamber.

Chapter V

Experimental Results

A water vapor plasma as discussed in Chapter 3 is electronegative. To characterize the differences between an electronegative and an electropositive plasma, plasma properties of an argon plasma (electropositive) and a water plasma are presented in Section 5.1. Section 5.2 examines the effects of RF power and magnetic field strength on hydrogen production and plasma properties of the water plasma. The effects of water input flow rates on hydrogen production and plasma properties are presented in Section 5.3. Finally, Section 5.4 summarizes the experimental results in this chapter.

5.1 Argon and Water Vapor Plasma Comparison

The aim of this section is to introduce some key characteristics of a water plasma discharge by comparing its plasma properties with those of an argon discharge. The operating pressure for the comparisons presented in this section is approximately 300 mtorr. Plasma properties–plasma density, floating and plasma potential, and electron temperature–are presented for matching conditions of RF power and axial magnetic field strength.

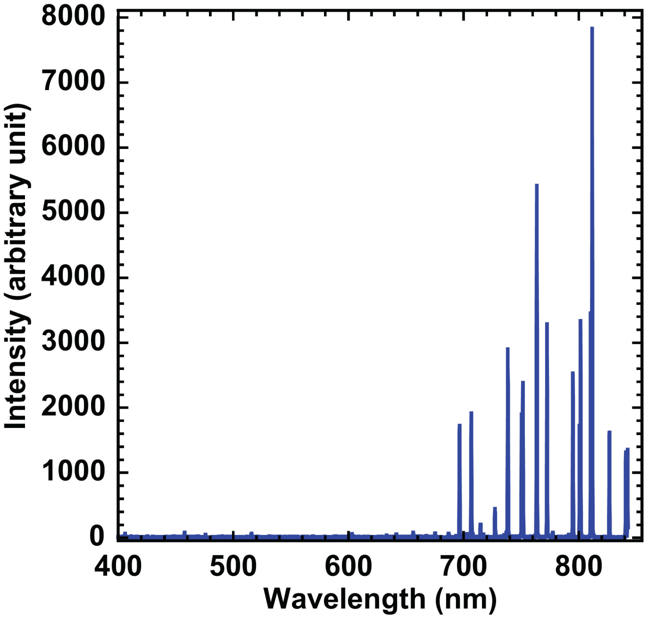

Figure 5.1: Optical emission spectrum of an argon discharge showing most of the argon neutral lines in the 400-850 nm wavelength range.

5.1.1 Optical Emission and Residual Gas Analyzer Spectra

Optical emission and residual gas analyzer spectra are used to identify the gas species inside the plasma discharge. Figures 5.1 and 5.2 show an optical emission spectrum from the plasma source operating on argon and on water vapor, respectively. An HR4000 spectrometer is used to obtain the spectrum shown in Figure 5.1. In order to detect the UV OH bands, an USB2000 spectrometer equipped with a detector that has a wider wavelength range was used and the spectrum is shown in Figure 5.2.

As illustrated, the optical emission spectrum of the argon plasma contains all of the expected prominent argon neutral lines as reported in the literature from NIST [86]: 696.5, 706.7, 738.4, 750.4, 751.5, 763.5, 772, 794, 800, 801, 810, 811, 826, 840, and 842 nm. A similar spectrum for a plasma discharge operating on water vapor shows a strong presence of hydrogen and hydroxyl. In particular, the first two lines in the Balmer series [86]–H_α at

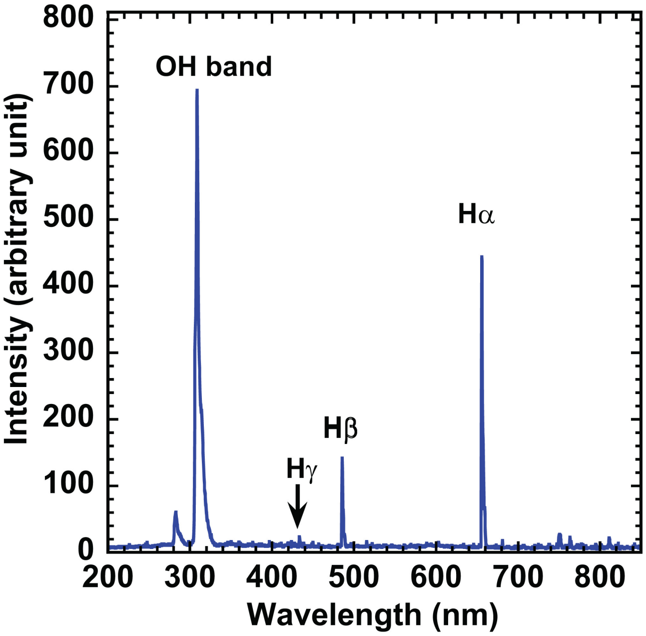

Figure 5.2: Optical emission spectrum of a water plasma discharge showing the hydrogen lines and the two OH bands.

656.3 nm and H_β at 486.1 nm–and two OH bands in the UV range [87]–281-303 nm and 305-330 nm–are clearly present.

The production of hydrogen and hydroxyl as shown in Figure 5.2 indicates that water molecules are being dissociated in the plasma discharge. Table 5.1 lists the major electron-water impact reactions. The cross-sections for these electron impact reactions with water are shown in Figure 5.3 as reported in a literature review by Itikawa and Mason in Reference 88. As shown, the dissociative mechanisms that dominate at the lower electron energies are dissociative attachments. Direct dissociation and dissociative ionization only occur at high electron energies greater than 10 eV.

The presence of excited atomic hydrogen lines and hydroxyl bands confirm that water molecules are being dissociated in the main plasma discharge. In addition to using optical spectrometers, an RGA is also employed to confirm the dissociation of water molecules in

Table 5.1: Electron impact reactions with H_2O

Momentum transfer	$H_2O + e \Rightarrow H_2O + e$
Vibrational Excitation	$H_2O + e \Rightarrow H_2O + e$
Dissociative Attachment	$H_2O + e \Rightarrow H^- + OH$
	$H_2O + e \Rightarrow O^- + H_2$
	$H_2O + e \Rightarrow OH^- + H$
Dissociation	$H_2O + e \Rightarrow H + OH + e$
	$H_2O + e \Rightarrow O + 2H + e$
Ionization	$H_2O + e \Rightarrow H_2O^+ + 2e$
	$H_2O + e \Rightarrow OH^+ + H + 2e$
	$H_2O + e \Rightarrow O^+ + H_2 + 2e$
	$H_2O + e \Rightarrow H_2^+ + O + 2e$
	$H_2O + e \Rightarrow H^+ + OH + 2e$

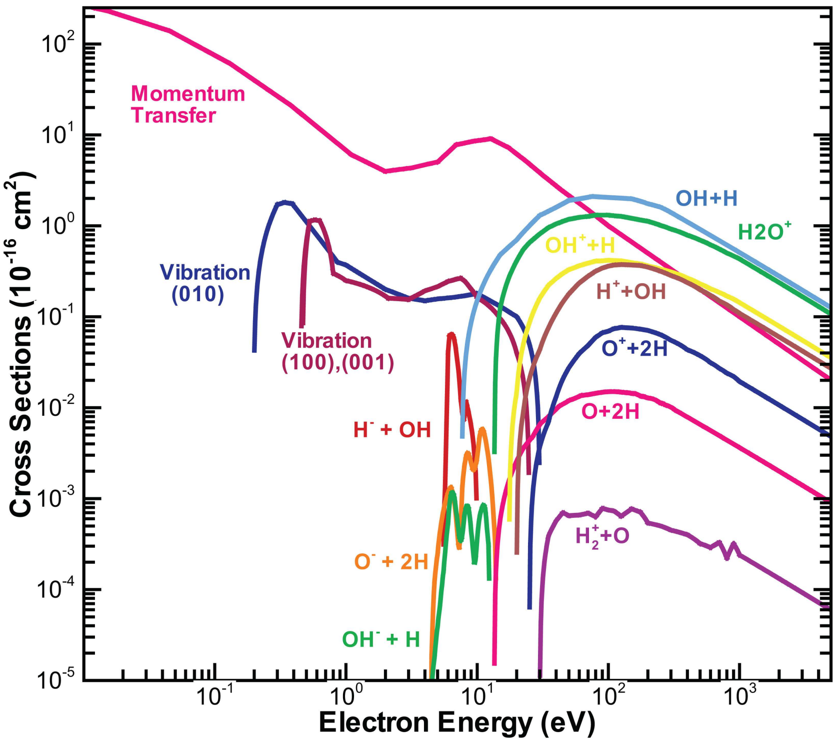

Figure 5.3: Cross-sections of electron impact with water molecules.

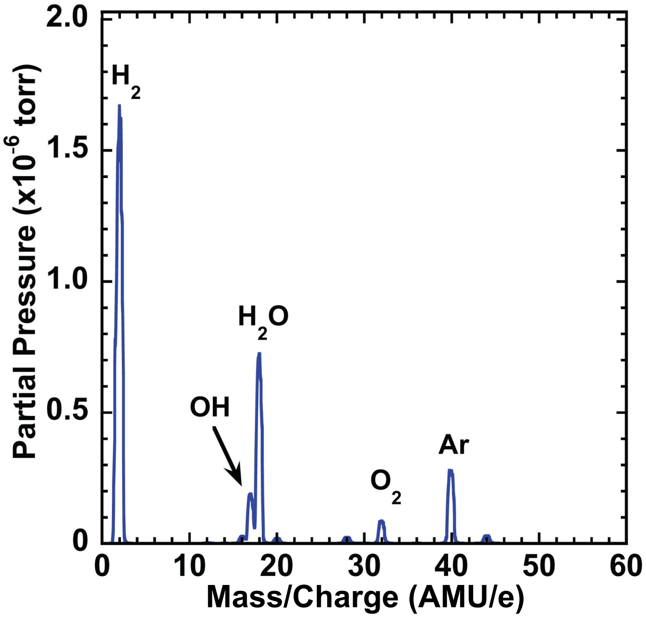

Figure 5.4: RGA spectrum of the water plasma indicating the presence of molecular hydrogen and oxygen, hydroxyl, and water. An argon peak is observed because a small amount of argon was added to the gas line for calibration purposes.

the discharge. For a discharge operating on only argon gas, there are two peaks: one dominant peak for singly-ionized argon at 40 AMU/e and one small peak for doubly-ionized argon at 20 AMU/e. For a plasma discharge operating on water vapor, the RGA spectrum contains several lines indicating the presence of molecular hydrogen (2 AMU/e) and oxygen (32 AMU/e), hydroxyl (17 AMU/e), and water (18 AMU/e), as shown in Figure 5.4. Further, when a small amount of argon is added to the gas line, a peak at 40 AMU/e is also observed. Therefore, RGA spectra further validate the dissociation of water molecules in the plasma discharge.

5.1.2 Plasma Densities

All plasma properties presented in this dissertation are obtained from Langmuir probe data collected downstream of the quartz tube and at the axis of symmetry for the source (r

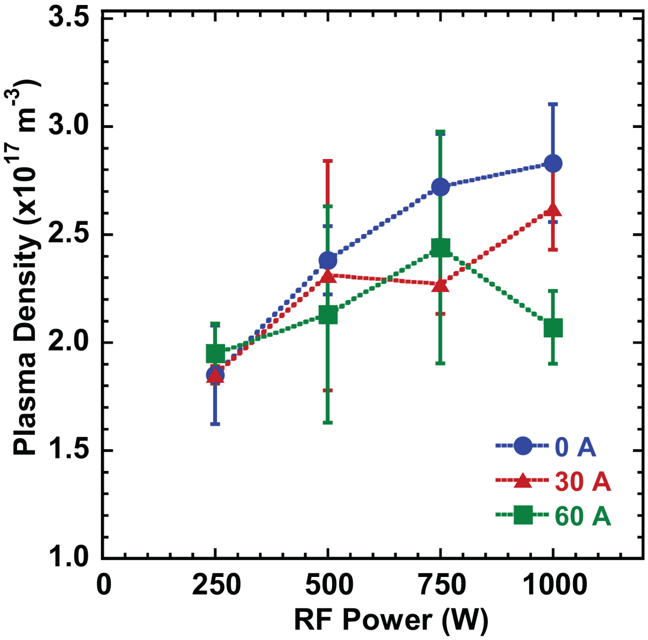

Figure 5.5: Plasma density of an argon discharge as a function of RF power for 0-A, 30-A, and 60-A applied magnet current.

= 0 location) as explained in Section 4.2.1. For an electropositive plasma such as argon, quasineutrality requires that the positive ion density equal to the electron density ($n_{i+} = n_e$). Figure 5.5 shows the ion density of the argon plasma as a function of RF power for 0-A, 30-A, and 60-A applied magnet current settings. The density is shown ranging from 1.8×10^{17} to 2.8×10^{17} m^{-3}. The error bars are shown, and they range from 0.04×10^{17} to 0.54×10^{17} m^{-3}, which correspond to 1% to 19% of the maximum value of the ion density. As shown, the error bars can be large at high RF power levels. However, the general trend shows that the ion density increases with RF power as expected for all applied magnet current settings. The result at 1000-W RF power level for the case of 60-A is an outlier to this trend, which is probably due to a mode change in the plasma.

Quasineutrality in the water discharge requires that the total positive ion density is equal to the sum of the negative ion density and the electron density ($n_{i+} = n_e + n_{i-}$).

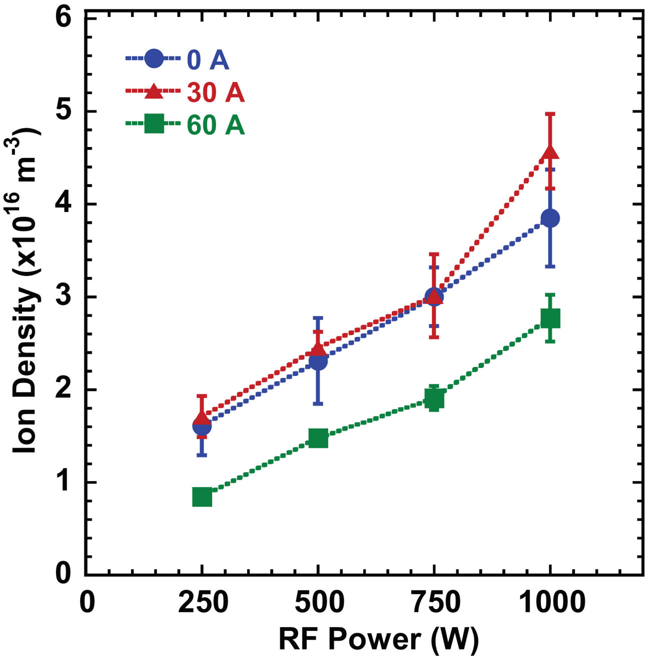

Figure 5.6: Ion density of the water plasma as a function of RF power for 0-A, 30-A, and 60-A applied magnet current.

In this discharge, dissociative electron attachment (Equation 3.7) and three-body electron attachment (Equation 3.8) are expected to be nontrivial due to the presence of high electron affinity species such as oxygen and hydroxyl that form negative ions. Thus, the ion density and the electron density are presented separately in Figures 5.6 and 5.7 for the water plasma. Under matching operating pressure, the ion density for the water vapor plasma is approximately one order of magnitude less than that of the argon plasma, ranging from 0.85×10^{16} to 4.6×10^{16} m^{-3}. The error bars range from 0.03×10^{16} to 0.52×10^{16} m^{-3}, which correspond to 0.1% to 11% of the maximum value of the ion density. The electron density of the water plasma is up to two orders of magnitude lower than the electron density of the argon plasma, ranging between 0.45×10^{15} m^{-3} and 7.9×10^{15} m^{-3}. The error bars range from 0.03×10^{15} to 2.37×10^{15} m^{-3}, which correspond to 0.3% to 30% of the maximum value of the electron density.

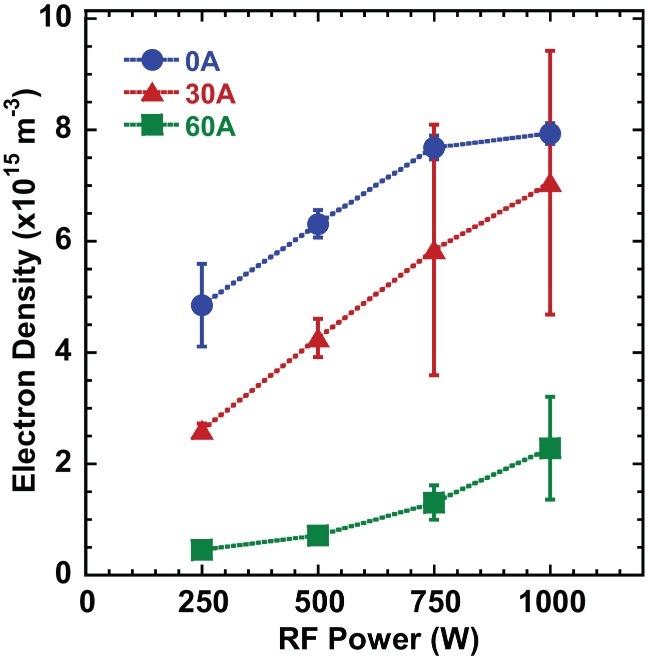

Figure 5.7: Electron density of the water plasma as a function of RF power for 0-A, 30-A, and 60-A applied magnet current.

As expected, the electron density of the water plasma is lower than that of the argon plasma because the water plasma has more collisional energy loss pathways for electrons. In the argon plasma, the collisional energy losses are electronic excitation and ionization. But for the water plasma, additional collisional energy losses include excitation of vibrational and rotational energy levels, and molecular dissociation. Therefore, if an equal amount of energy is deposited into the two discharges, there is less energy available for electrons to create ion-electron pairs in the water plasma than in the argon plasma. Additionally, in the water plasma, electrons are also consumed in dissociative electron attachment and three-body electron attachment processes to produce negative ions. Thus, the low electron density in the water plasma compared to that in the argon plasma are expected results.

In the water plasma, the magnetic field strength and RF power appreciably affect both ion and electron densities. For the ion density, there is an almost linear increase with RF power. Similarly, the electron density also increases with RF power in the water plasma. The observed increase in densities with RF power is expected for the argon plasma and the water plasma. As more energy is deposited into the discharge, the total ionization rate increases with density ($K_{iz} \propto n_e n_g < \sigma v >$).

On the other hand, the electron and ion densities decrease with applied axial magnetic field. For the water plasma, there is a negligible difference in ion densities for 0-A and 30-A applied magnet current settings, but a significant decrease from 30-A to 60-A applied magnet current. The electron density clearly decreases with applied magnet current. These trends can be explained by examining how RF power is coupled to the plasma source and the effects of the additional axial magnetic field on the mobility of the electrons and ions.

As discussed in Section 3.3.3, the electric and magnetic fields can only penetrate into the plasma within the skin depth layer in an inductive plasma discharge. The thickness of this skin depth layer is inversely proportional to the square root of the electron density (Equations 3.21 and 3.22). For a low electron density (*e.g.* 10^{15} m^{-3}), the skin depth layer thickness can be as large as 16 cm, which is the diameter of the discharge. On the other hand, for a higher electron density (*e.g.* 10^{17} m^{-3}), the skin depth thickness is only 1.7 cm. In a different previous experiment, at a lower pressure of a few mtorr and with argon as the operating gas, the ion number density could be as high as 2.5×10^{19} m^{-3}, where the helicon mode was detected [25]. It was also shown that the ion density ranges from 1×10^{18} m^{-3} to 5×10^{18} m^{-3} for the capacitive mode and from 1×10^{19} m^{-3} to 2×10^{19} m^{-3} for the inductive mode. Even though these high densities are not observed in the

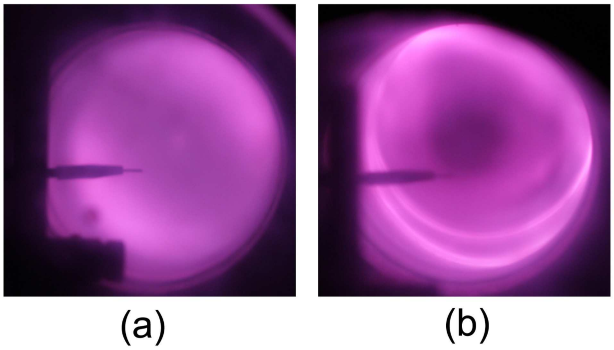
(a) (b)

Figure 5.8: Photographs of water plasma operating at (a) 0-A and (b) 30-A applied magnet current.

water plasma, the discharge is still expected to operate in either capactive or inductive mode based on the behavior of the discharge and the calculated skin depth thickness. Figure 5.8 shows two photographs of the discharge, without and with an applied magnetic field.

As shown in the photographs in Figure 5.8, the tip of the LP probe is at a fixed r = 0 position (plasma source centerline) downstream of the discharge. The density measurements presented here are local measurements–not line-integrated or volume-averaged densities. Without the magnetic field (Figure 5.8a), the discharge appears diffused making the local measurement more representative of a volume average. But if the electrons are confined to the annular region near the wall of the discharge (Figure 5.8b), this density does not represent the volume-averaged density.

The applied axial magnetic field affects the electrons in two ways. First, the magnetic field enhances electron confinement in the discharge because the electrons gyrate along the field lines. Second, the magnetic field reduces the mobility of the electron in the direction that is perpendicular to the magnetic field lines. The diffusion coefficient across the magnetic field is [81]:

$$D_{\perp} = \frac{D}{1 + \omega^2 \tau^2} \tag{5.1}$$

where D is the diffusion coefficient in the absence of a magnetic field, ω is the cyclotron frequency, and τ is the mean collision time. As an example, for a gas pressure of 300 mtorr, electron temperature of 2 eV, and ion temperature of 0.05 eV, and a magnetic field of 400 G, the diffusion coefficient across the magnetic field is reduced by 16000 times for electrons, but only by a factor of 23 for ions.

The reduction in the ion and the electron number densities in the water plasma in the presence of the magnetic field as shown in Figures 5.6 and 5.7 are then the results of a combination of the following: First, the applied axial magnetic field enhances the electron confinement, and the electrons created near the wall of the discharge cannot easily cross the field lines. Therefore, the measurements made outside confinement zones may not reflect the density increase. Additionally, because the electrons cannot easily diffuse into the bulk of the discharge due to its reduced mobility in the perpendicular direction, the electron density in the bulk discharge can actually be reduced. Second, the ions and neutrals are not affected by the presence of the applied magnetic field. Further, some of the electrons that diffuse into the bulk discharge are consumed through either three-body electron attachment or dissociative attachment processes. The combination of these effects is the likely cause of the trend shown in Figure 5.7, where electron density decreases with applied magnet current for any RF power level. As a result of this reduction in electrons in the core of the discharge, ion density is also reduced. Note that electrons are confined in the argon plasma in the presence of a magnetic field, but they are not consumed in attachment processes in the core of the discharge.

Bohm time gives an estimate of the electron diffusion time, and it is another parameter used to determine the effect of the magnetic field to the mobility of the electrons. Equation 5.2 shows how Bohm time is calculated:

$$\tau_B = \frac{R^2}{2D_B} \tag{5.2}$$

where τ_B, R, and D_B are the Bohm time, radius of the cylinder, and Bohm diffusion coefficient, respectively. Unlike the kinetic collisional diffusion coefficient, the Bohm diffusion coefficient is independent of the density:

$$D_B = \frac{1}{16}\frac{T_e}{B} \tag{5.3}$$

For T_e of 2 eV and B of 400 G, the Bohm time was calculated to be 0.1 second. Therefore, while the magnetic field confines the electrons, some of them do cross the field lines and enter the core of the discharge, with the diffusion time of 0.1 second.

5.1.3 Electron Temperature

The electron temperature of the water and argon plasmas are compared. Figures 5.9 and 5.10 show the electron temperature for argon and water plasmas, respectively. For the argon plasma, the electron temperature varies between 1.2 and 1.4 eV with error bars between 0.2 and 0.3 eV (14% to 21% of the maximum value). The electron temperature is

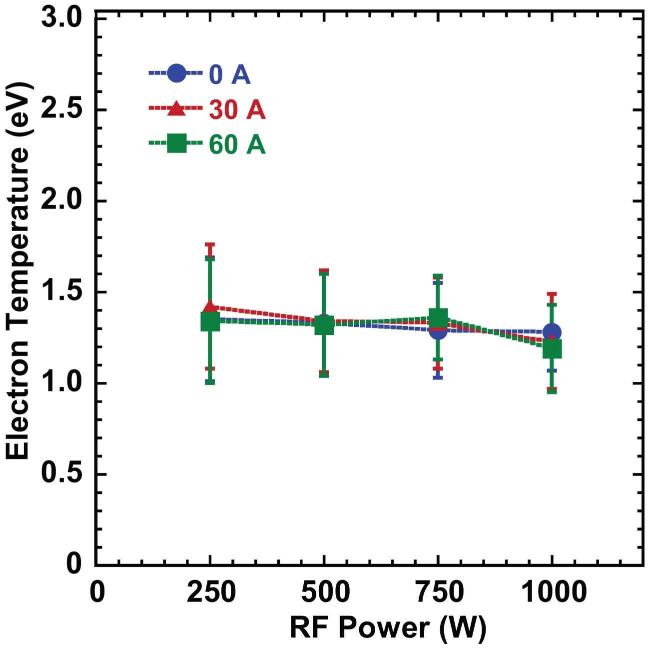

Figure 5.9: Electron temperature of the argon plasma as a function of RF power for 0-A, 30-A, and 60-A applied magnet current.

not affected by RF power or applied magnet current as expected. In general, the electron temperature is determined by particle conservation alone, and is independent of the plasma density and thus the input power [52]. Therefore, electron temperature is independent of RF power.

For the water plasma, the electron temperature has significantly larger error bars; and it ranges from 2.7 to 3.9 eV with error bars between 0.7 and 2.2 eV (18% to 56% of the maximum value). The large error bars are introduced in the process of smoothing the noisy IV traces. Further, the water plasma in general was less stable than the argon plasma. Due to these large error bars, no clear trend for electron temperature with RF power or applied magnet current is observed. It has been reported that the collisional energy loss per electron-ion pair created for a molecular gas is 2-10 times higher than an atomic gas when the electron temperature is below 7 eV [52]. Thus, in order to sustain a discharge operating

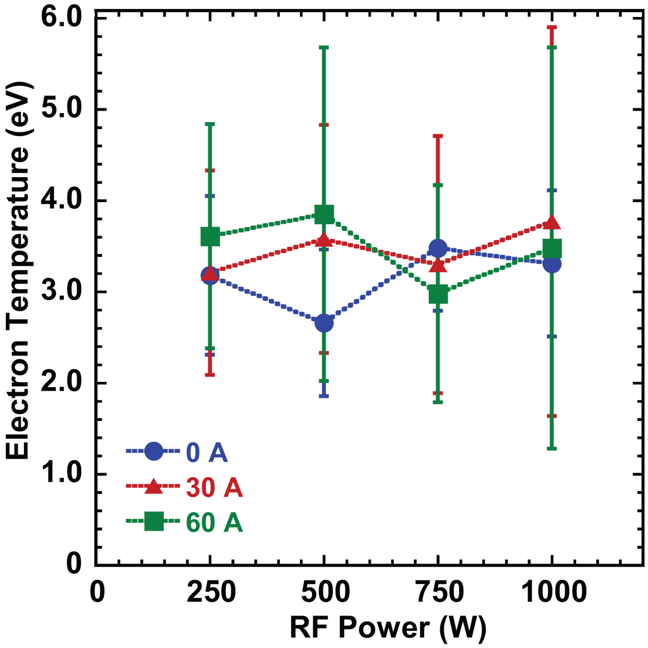

Figure 5.10: Electron temperature of the water plasma as a function of RF power for 0-A, 30-A, and 60-A applied magnet current.

on a molecular gas, the electron temperature must necessarily be higher in order to achieve adequate ionization, which may explain why the electron temperature for the water plasma is higher than that of the argon plasma. In addition, it is also possible that for a similar input power, the water plasma has a lower density, which results in a high capacitive field and corresponding high electron temperature.

5.1.4 Floating and Plasma Potentials

The floating potential is the potential applied to the Langmuir probe to achieve equal total positive and total negative currents to the probe ($I^+ = I^-$), where I^+ represents the positive ion current and I^- represents the electron current in an electropositive plasma or the sum of electron and negative ion currents in the electronegative plasma. Figures 5.11 and 5.12 show floating and plasma potentials for the argon and water plasma, respectively.

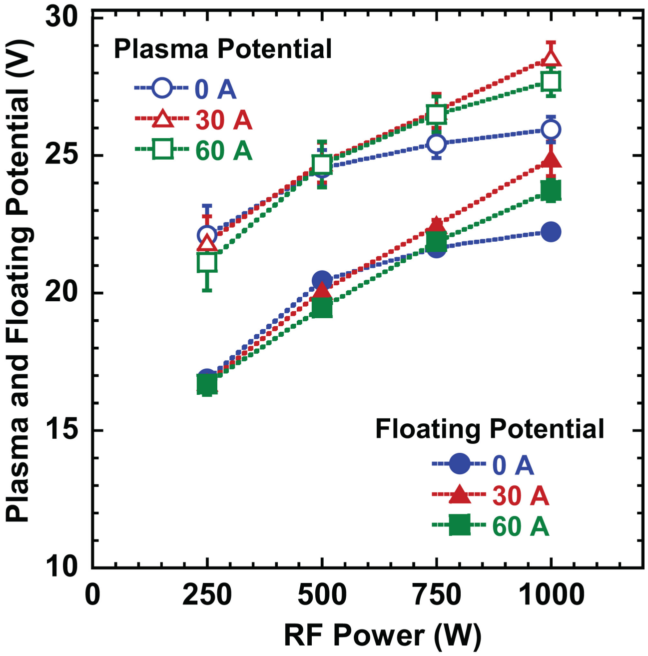

Figure 5.11: Floating and plasma potential of the argon plasma as a function of RF power for 0-A, 30-A, and 60-A applied magnet current.

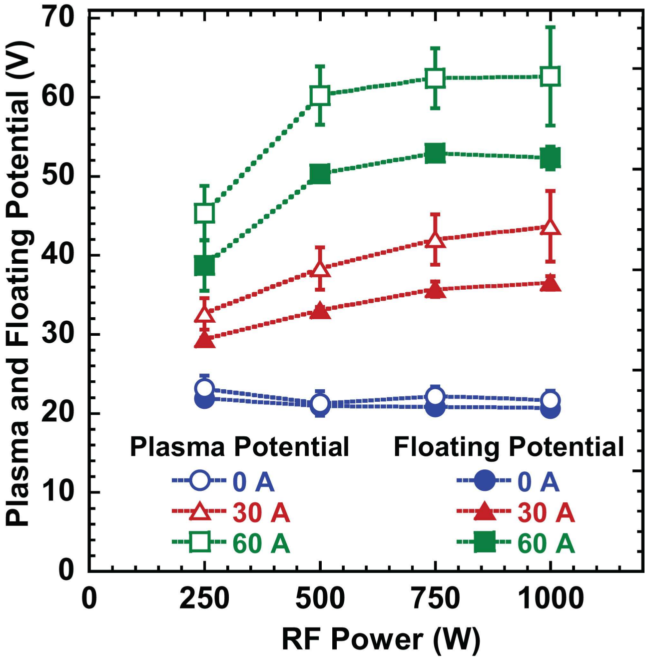

Figure 5.12: Floating and plasma potential of the water plasma as a function of RF power for 0-A, 30-A, and 60-A applied magnet current.

Floating and plasma potentials for the water plasma are higher than those of the argon plasma. For the argon plasma, the floating potential ranges from 17 to 25 V with error bars between 0.08 and 0.63 V. The floating potential increases with RF power, but is not strongly affected by the applied magnet current except at high RF power (1000 W). The plasma potential is consistently 4-5 V higher than the floating potential. For an electropositive plasma, the electron temperature is directly related to the difference between the plasma and floating potentials as shown in Equation 5.4. Therefore, the nearly constant difference between the plasma and floating potentials indicates that the electron temperature for the argon plasma is constant with RF power and magnetic field. This conclusion agrees with the constant electron temperature.

$$V_p - V_f = \frac{T_e}{2} ln \left(\sqrt{\frac{\pi m}{2M}} \right) \tag{5.4}$$

Equation 5.4 is derived for an electropositive plasma by setting the electron current equal to the ion current [52, 81]:

$$I_e = I_i \tag{5.5}$$

In Equation 5.5, the electron and ion currents are:

$$I_e = \frac{1}{4} e n_e \bar{v}_e A exp \left(\frac{V_B - Vp}{Te} \right) \tag{5.6}$$

$$I_i = en_s u_B A \tag{5.7}$$

where n_s is the density at the sheath ($n_s \approx 0.61 n_o$), u_B is the Bohm velocity, A is the area of the probe, and V_P is the plasma potential. V_B is the bias voltage of the probe and is equal to V_F when the condition in Equation 5.5 is satisfied. The relationship between plasma potential, floating potential, and electron temperature derived in Equation 5.4 is only applicable for an electropositive plasma. For an electronegative plasma, Equation 5.5 becomes:

$$I_{i+} = I_e + I_{i-} \tag{5.8}$$

where I_e, I_{i+}, I_{i-} are the electron current, the positive ion current, and the negative ion current. Following a similar derivation for the electropositive plasma, Equation 5.9 is established for the electronegative plasma [89].

$$u_B(1+\alpha_s) = \frac{1}{4}\bar{v}_e exp\left(\frac{V_F - V_p}{T_e}\right) + \frac{1}{4}\alpha_s u_{i-} exp\left(\frac{V_F - V_p}{T_{i-}}\right) \tag{5.9}$$

where $\alpha_s = n_{i-}/n_e$ is the electronegativity. Without electronegative species ($n_{i-} = 0$), Equation 5.9 reduces to Equation 5.4. The first term on the right-hand side of Equation 5.9 represents the electron current and the second term represents the negative ion currents. For a relatively low ion temperature, the second term on the right-hand side reduces to zero due to the exponential function of a large negative number. The equivalence of Equation

5.4 for an electronegative plasma is approximated as:

$$V_p - V_f \approx T_e ln \left(\frac{1}{1+\alpha_s} \sqrt{\frac{M_i}{2\pi m_e}} \right) \tag{5.10}$$

Equation 5.10 shows that the difference between the plasma and floating potential for an electronegative plasma is only a weak function of the electronegativity.

In the water plasma, the difference between the plasma and the floating potential is up to 10 V compared to 5 V in the case of the argon plasma. Higher electron temperature offers an explanation for the larger difference between the plasma and floating potential in the water plasma. For the water plasma, the effective ion mass is between 9 and 11 AMU. Note that the difference between the plasma and the floating potential is not a strong function of electronegativity or the relative ion mass.

The results for the water plasma show that the floating potential ranges from 21 to 53 V with error bars ranging from 0.2 to 3 V (0.4% to 6% of the maximum value). With the 60-A applied magnet current setting, the water plasma's floating potential is twice that of the argon plasma for RF power greater than 500 W. The exact physical phenomenon that causes the floating potential to increase in the water plasma has not been identified. However, one plausible explanation is as follows.

In addition to quasineutrality:

$$n_{i+} = n_{i-} + n_e, \tag{5.11}$$

the water plasma must also maintain ambipolar diffusion:

$$\Gamma_{i+} = \Gamma_{i-} + \Gamma_e \tag{5.12}$$

where Γ is the flux of particles. At high magnetic field, the electrons are confined to the production region near the wall of the discharge, but the negative and positive ions are moving freely into the core of the discharge. In order to maintain quasineutrality, the plasma potential then needs to increase to allow the electrons to flow to the core of the discharge. Due to the nature of the electronegative plasma, many of the electrons that make it to the core of the plasma are being consumed in attachment processes. The plasma potential increases with magnetic field because the electrons are more confined to the wall at higher magnetic field. Therefore, a higher plasma potential is needed in order to maintain quasineutrality in the core. The floating potential increases as a result of Equation 5.10.

5.1.5 Summary

OES and RGA spectra are presented and they validate the presence of the species from dissociated water molecules in the water vapor plasma discharge. An electropositive argon plasma was characterized and compared with the electronegative water plasma. In an argon plasma, the only collisional energy losses are ionization and excitation. On the other hand, the water plasma's collisional energy losses include excitation of vibrational and rotational energy levels, and molecular dissociation. Further, electrons are also lost in electron attachment and dissociative attachment processes. Therefore, the argon ion density ($n_i = n_e$) is higher than the electron density of the water plasma by up to two orders of magnitude. The electron temperature of the water plasma contains large error bars (up to 50%) that result from the error introduced when smoothing the IV traces. The average electron temperature is shown to be higher than that of the argon plasma by 1.5 eV.

5.2 Effects of Applied Axial Magnetic Field

Section 5.1 compares the differences in plasma properties of the plasma discharge operating on argon gas and on water vapor. This section investigates the effect of RF power and magnetic field strength on hydrogen production in the water plasma discharge. In addition, the electron and ion densities are also examined to offer physical explanation of the observed trends in the hydrogen production rate.

5.2.1 Hydrogen Production

The hydrogen production rate is reported for 0-A, 30-A, and 60-A applied magnet current settings as a function of RF power in Figures 5.13 and 5.14 for 75-sccm and 125-sccm water vapor input flow rate, respectively. The hydrogen production rate is determined from the method outlined in Section 4.2.1 via the RGA. Without an applied magnet current (0-A setting), the hydrogen production rate increases linearly with RF power. For the 30-A and 60-A applied magnet current settings, the hydrogen production rate increases from 250-W to 500-W RF power, but it saturates starting at 500 W. Despite this observed saturation as a function of RF power, the hydrogen production rate is clearly higher with an applied axial magnetic field than without it at all RF power levels. The effects of RF power and applied magnet current on the hydrogen production rate are similar for both 75-sccm and 125-sccm

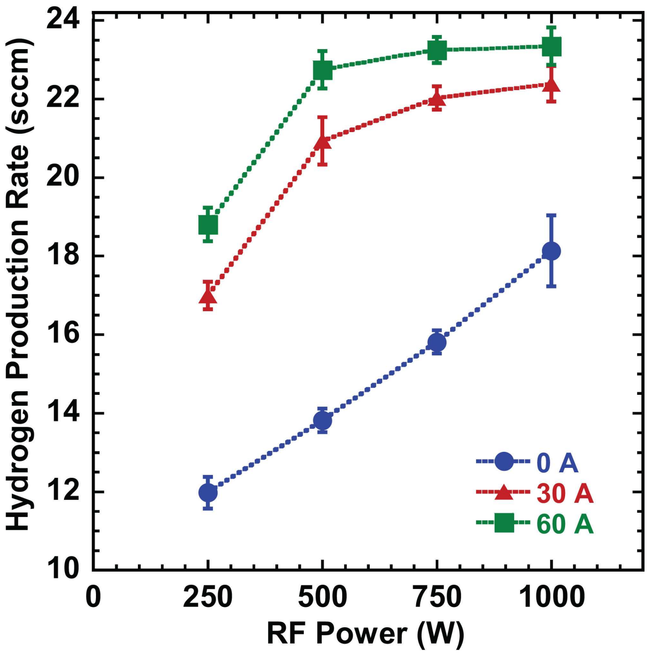

Figure 5.13: Hydrogen production rate as a function of RF power for 0-A, 30-A, and 60-A applied magnet current and 75-sccm water input flow rate.

water input flow rate. In fact, these effects are also observed in all other water input flow rates in this investigation.

The observed saturation of the hydrogen production rate with RF power in the presence of an applied axial magnetic field could be explained by examining the electron and ion densities of the discharge. As shown in Figure 5.8 and discussed in the previous section, the axial magnetic field confines electrons to the plasma production zones, which include the annular volume adjacent to the wall of the quartz tube, closest to the antenna. In this inductively-coupled plasma source, power is transferred from the electric fields to the plasma electrons within a skin depth layer near the plasma surface by Ohmic and stochastic heating in this annular region [52]. Therefore, much of the production of electrons is within this layer, whose thickness varies inversely with the square root of the electron density (Equations 3.21 or 3.22). As a function of RF power, the electron density increases

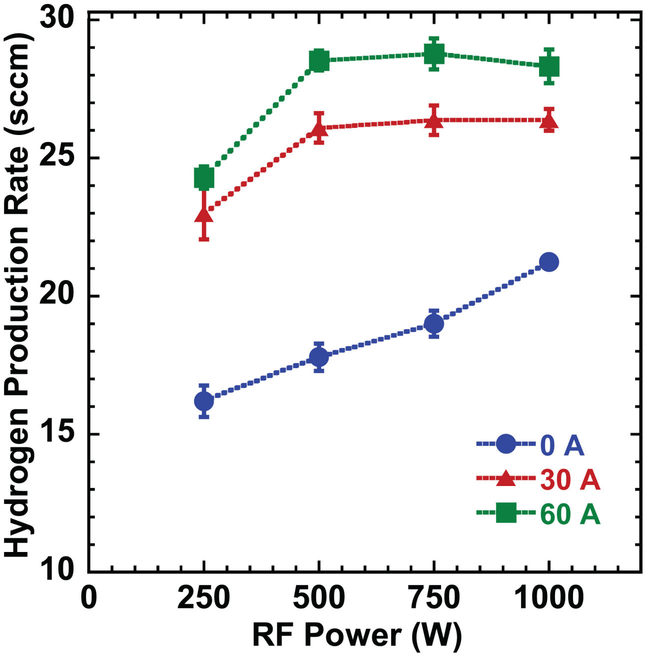

Figure 5.14: Hydrogen production rate as a function of RF power for 0-A, 30-A, and 60-A applied magnet current and 125-sccm water input flow rate.

with the skin depth thickness decreasing in response.

The magnetic field inhibits electrons from diffusing into the core of the discharge to initiate water-electron impact reactions. Despite an increase in electron density with RF power, electrons cannot easily cross the field lines. However, those electrons that are in the core of the discharge have a better confinement in the presence of the magnetic field. This improvement in electron confinement also leads to more electron attachment and dissociative attachment. This explains the increase in hydrogen production when the magnetic fields are present. However, with the magnetic field, hydrogen production saturates with RF power. Again, electron density is proportional to RF power, but the skin depth thickness is inversely proportional to the square root of the density. Therefore, even though the magnetic field enhances the electron production in the discharge, it also reduces the electrons' rate of diffusion into the discharge to initiate electron-water impact reactions.

Consequently, for a constant applied magnet current, the magnetic field generates two competing factors that affect the rate of hydrogen production. On the one hand, the magnetic field inhibits electrons that are primarily produced near the edge of the source from entering the core of the discharge. On the other hand, the magnetic field enhances electron confinement, thus increasing the probability of electron collisions. These two effects cancel each other, and this explains why hydrogen production saturates with RF power when there is a magnetic field. The fact that the rate of hydrogen production increases with applied magnet current suggests that the second effect–enhanced electron confinement–is stronger than the first effect at higher magnetic field strength. This behavior could also be due to enhanced ionization in the heating zone, the annular region closest to the antenna.

5.2.2 Electron and Ion Number Density

The ion and electron densities for the water plasma with 75-sccm water input flow rate are shown in Figures 5.6 and 5.7, respectively. The densities increase with RF power, but decrease with applied magnet current. As more energy is deposited into the plasma, electron production necessarily increases through various electron heating mechanisms including Ohmic and stochastic heatings. However, the densities in the core decrease as a function of magnet current. Note again that the results presented here are local measurements at r = 0 location downstream of the discharge. These results of densities decreasing with applied magnet current again suggest that the electrons are produced near the wall of the quartz tube and radial diffusion rate is reduced due to the presence of the axial magnetic field. This saturation effect is not seen as strongly with ions since they are not magnetized.

Rather they grow linearly with RF power. Presumably negative ions assist in maintaining quasineutrality. Negative ions production is suggested by the saturation of electron density but a linear growth in ion density. As shown previously, hydrogen production increases with applied magnet current. Dissociative attachment is speculated to be the main dissociation mechanism in the water plasma discharge:

$$H_2O + e \rightarrow OH^- + H \tag{5.13a}$$

$$H_2O + e \rightarrow OH + H^- \tag{5.13b}$$

$$H_2O + e \rightarrow O^- + H_2 \tag{5.13c}$$

The first two mechanisms (Equations 5.1a and 5.1b) are favored over the last mechanism (Equation 5.1c) because they require less energy [52].

5.2.3 Summary

In summary, the RGA results show that the hydrogen production rate increases with applied magnet current, but saturates with RF power after 500 W in most cases. Electron and ion densities, however, decrease with applied magnet current, but increase with RF power. In the presence of the magnetic field, electron confinement in the core of the discharge is enhanced. At the same time, diffusion of electrons produced near the antenna to the bulk discharge is limited because electrons cannot easily cross the field lines.

5.3 Effect of Water Input Flow Rate

Section 5.2 discusses the effect of the magnetic field on hydrogen production in the water plasma discharge. This section investigates the effect of the water input flow rate on the hydrogen production rate and the plasma properties of the water plasma discharge.

5.3.1 Hydrogen Production

To investigate the effects of water vapor input flow rate on the hydrogen production rate and the plasma properties, the water flow rate into the system is set at 25, 50, 75, 100, and 125 sccm. Figures 5.15 and 5.16 show the hydrogen production rate for these input water flow rates as a function of RF power for 0-A and 30-A magnet current setting, respectively. As noted in Section 5.2, the rate of hydrogen production increases linearly with RF power without an applied magnet current but saturates with RF power with an applied magnet current albeit at higher RF power levels. Figures 5.15 and 5.16 illustrate the consistency of these trends for all water input flow rates.

At 0-A applied magnet current and 250-W RF power, an abrupt increase in hydrogen production is observed between 25-sccm and 50-sccm water vapor input flow rates and between 75-sccm and 100-sccm water vapor input flow rates. For the other RF power levels–500, 750, and 1000 W–there is a clear jump in hydrogen production from 25-sccm to 50-sccm water vapor input flow rate, but no further increase is observed within the uncertainty of the measurement. At 30-A applied magnet current, adding more water vapor increases the rate of hydrogen production but this trend stops at 100-sccm water vapor flow rate. Hydrogen production for the case of 125-sccm water vapor is lower than that of

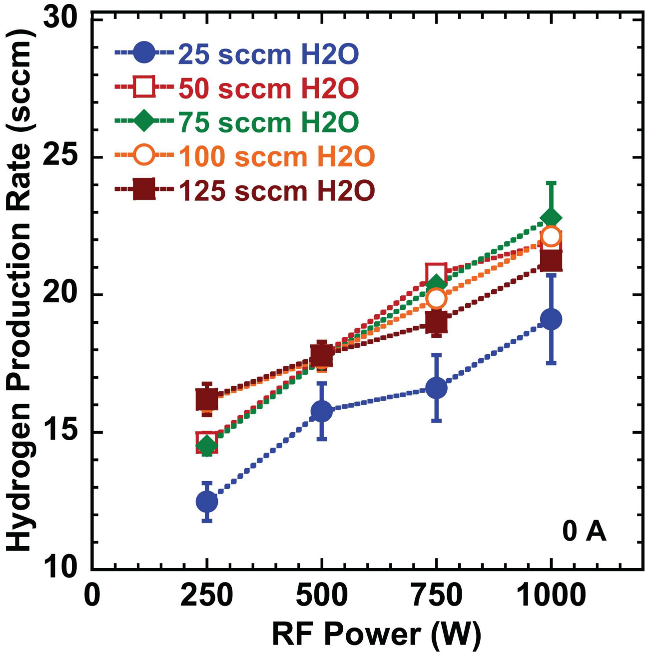

Figure 5.15: The rate of hydrogen production as a function of RF power for 25, 50, 75, 100, and 125-sccm water input flow rates, operating without an applied magnet current.

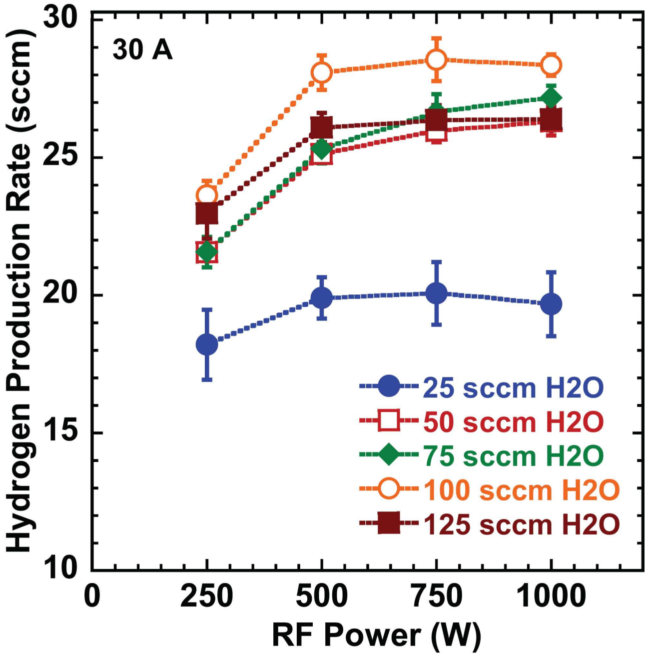

Figure 5.16: The rate of hydrogen production as a function of RF power for 25, 50, 75, 100, and 125-sccm water input flow rates, operating with 30-A applied magnet current.

100-sccm water vapor.

This may be explained as follows. For a given RF power level, a higher water vapor input flow rate means the energy available per molecule is reduced. There is an optimum energy per molecule to dissociate water molecules at a given flow rate (pressure). Therefore, hydrogen production rate initially increases with water input flow rate up to the optimum energy per molecule. Further addition of water vapor reduces the energy available per molecule to a value below the optimum value. Therefore, beyond 100 sccm, the energy available per molecule is not consistent with a higher production rate, hence hydrogen production rate decreases. Figure 5.17 shows the rate of hydrogen production as a function of water input flow rate. As illustrated, at 100 sccm water input flow rate, the hydrogen production is at a maximum for all RF power levels. It was expected that the maximum peak would shift to the right of the plot (towards a higher flow rate) for a higher RF power. However, this is not clearly demonstrated in Figure 5.17. The hydrogen production rate for 500, 750, and 1000-W RF power are nearly equal. For 500 W RF power and a hydrogen production rate of 28 sccm, the cost of energy to produce one H_2 is 266 eV. As a reference, the first theoretical dissociation energy ($H_2O \rightarrow H + OH$) for the water molecule is 5.17 eV per molecule and for the second ($OH \rightarrow H + O$) is 4.52 eV per molecule. This suggests that input energy is not efficiently going towards the dissociation of the water molecules, and also any further production of hydrogen is lost through recombination processes as the flow rate is increased.

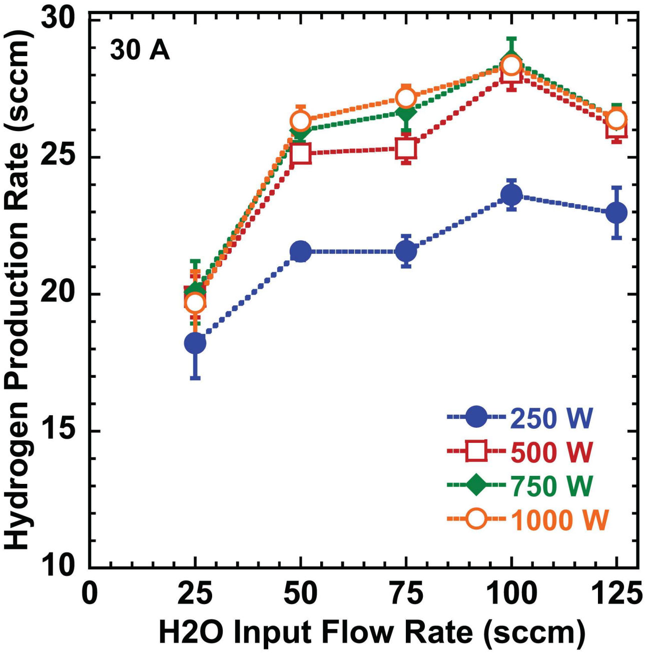

Figure 5.17: The rate of hydrogen production as a function of water input flow rate for 250 – 1000 W

5.3.2 Production of Other Gases

In this section, the production of other gases in the plasma discharge operating on water vapor is investigated. Figures 5.18, 5.19, and 5.20 show the rate of the un-dissociated water vapor and the production rate of hydrogen, oxygen, and hydroxyl for 25, 75, and 125-sccm water vapor input flow rate obtained from the RGA, respectively. Note that one sccm of H_2O carries one sccm of H_2 but only one-half sccm of O_2.

At 25-sccm water vapor input flow rate, the dominant species in the plasma source is in fact hydrogen, followed by water vapor, oxygen, and hydroxyl. However, at 75-sccm water vapor input flow rate, there is a slight increase in hydrogen production, but the dominant species in the plasma discharge is un-dissociated water molecule. This trend also continues in the case of 125-sccm water vapor. In all these three cases, hydrogen production increases

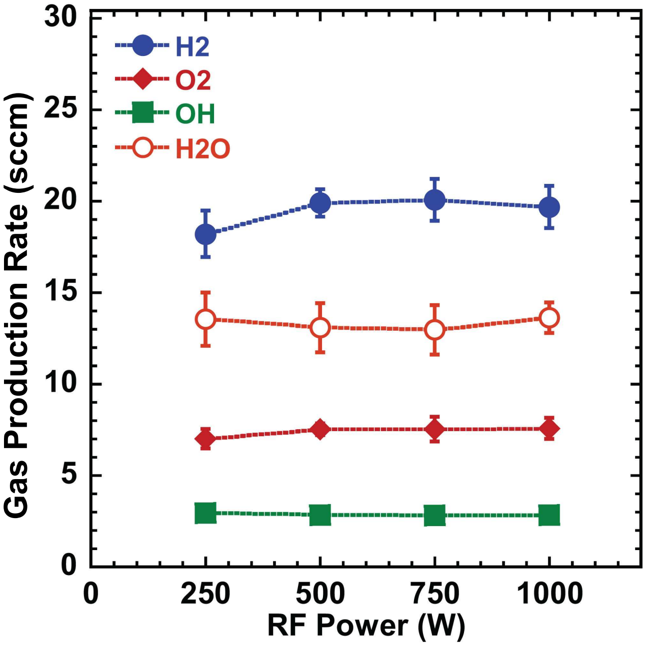

Figure 5.18: Production of hydrogen, oxygen, and hydroxyl in a plasma discharge operating on water vapor with 25-sccm water input flow rate and 30-A applied magnet current.

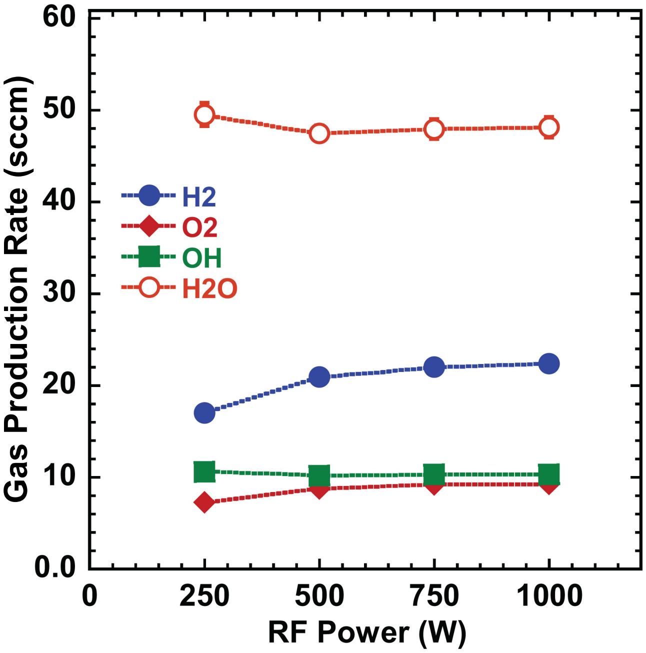

Figure 5.19: Production of hydrogen, oxygen, and hydroxyl in a plasma discharge operating on water vapor with 75-sccm water input flow rate and 30-A applied magnet current.

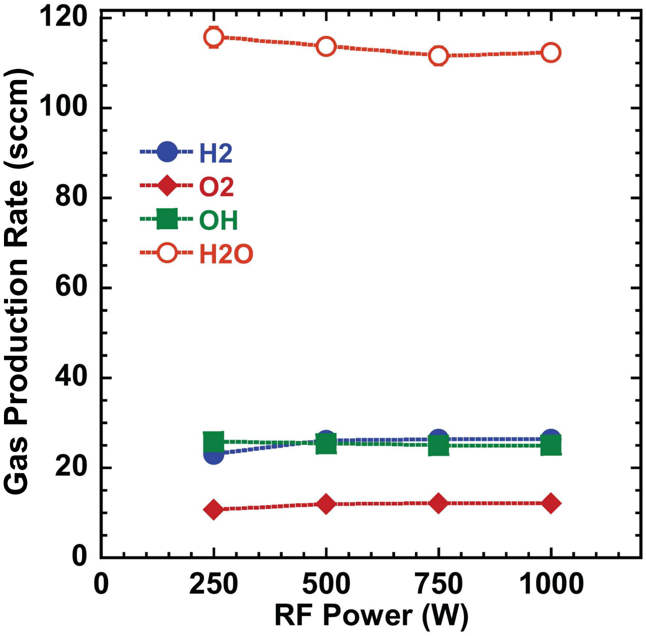

Figure 5.20: Production of hydrogen, oxygen, and hydroxyl in a plasma discharge operating on water vapor with 125-sccm water input flow rate and 30-A applied magnet current.

by 50%, from a maximum value of 20 sccm to 30 sccm for 25-sccm and 125-sccm water vapor, respectively. Similarly, there is also a small increase in the production of oxygen as a function of water input flow rate, with a maximum value of 8 sccm to 12 sccm. However, there is a significant percent increase in hydroxyl production, from 3 sccm to 25 sccm for 25-sccm and 125-sccm water flow rates, respectively.

This suggests that the first two dissociative mechanisms (Equations 5.13a and 5.13b) are favored over the last mechanism (Equation 5.13c). This result is consistent with the fact that the first two mechanisms require less energy than the last mechanism. As the water vapor flow rate increases, initially only one O-H bond in the water molecule is broken first via dissociative attachment. Therefore, as more water is added, there is more OH available in the plasma source. On the other hand, the atomic hydrogen from OH-H dissociation is very mobile due to its low mass, and therefore may have very little opportunity to combine with another atomic hydrogen to become a molecular hydrogen. But the atomic hydrogen produced in the OH-H dissociation is very likely combine to the surfaces of the chamber wall. Further, the fact that oxygen does not have a large percent increase with water flow rate suggests that any possible further dissociation of OH into O and H is not favored. The cross sections for these reactions are shown in Figure 5.3. The electron temperature is observed to decrease with increasing water input flow rate. This trend would tend to reduce reaction rates.

5.3.3 Electron and Ion Number Density

The electron density for varying water input flow rates is shown in Figures 5.21 and 5.22 as a function of RF power for 0-A and 30-A applied magnet current setting, respectively. In general, the electron density increases with RF power for a fixed water flow rate and decreases with water vapor input flow rate for a fixed RF power level. The increase in electron density with RF power is expected because as more energy is deposited into the discharge, the total ionization rate ($\propto n_g n_e < \sigma V >$) increases through the increase in electron density. As discussed previously, as more water vapor is introduced into the discharge at a fixed RF power, the energy per molecule is reduced. This explains the reduction in electron density with water input flow rate.

The ion density is shown in Figures 5.23 and 5.24 as a function of RF power for 0-A and 30-A applied magnet current setting, respectively. Similar to electron density, the ion density increases with RF power. This again is due to the increased total ionization rate

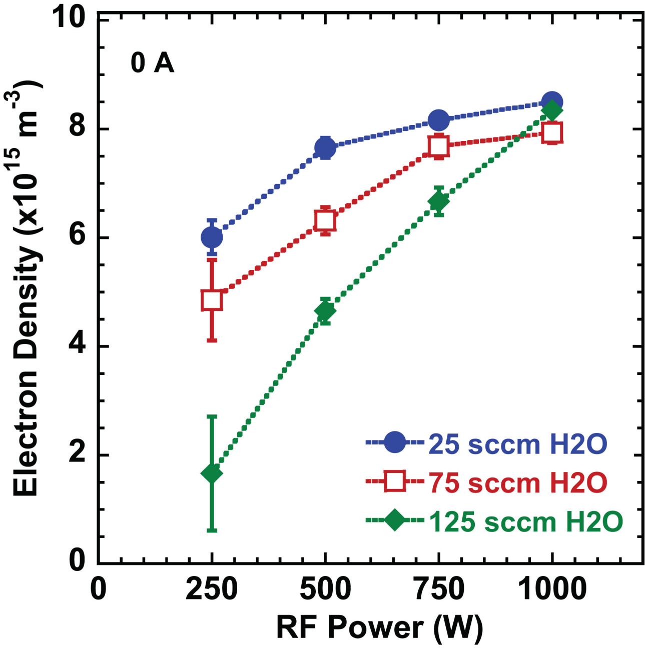

Figure 5.21: Electron density as a function of RF power for 25, 75, and 125-sccm water input flow rates without an applied magnet current.

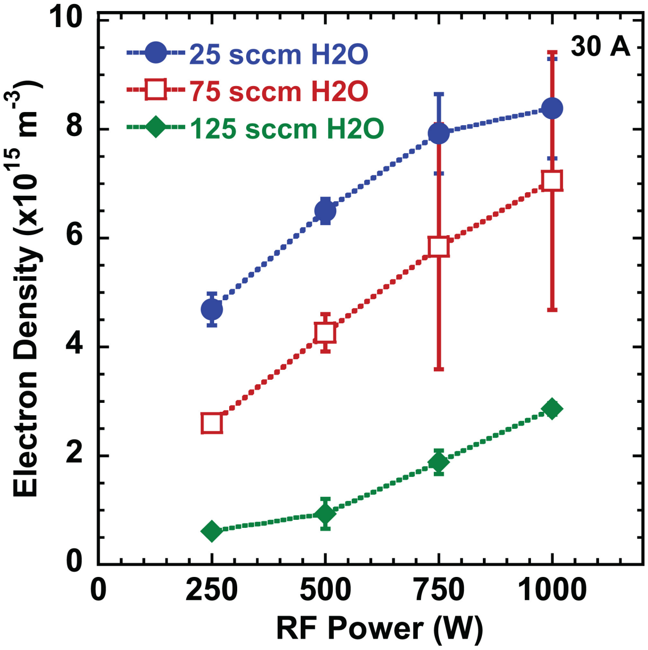

Figure 5.22: Electron density as a function of RF power for 25, 75, and 125-sccm water input flow rates with 30-A applied magnet current.

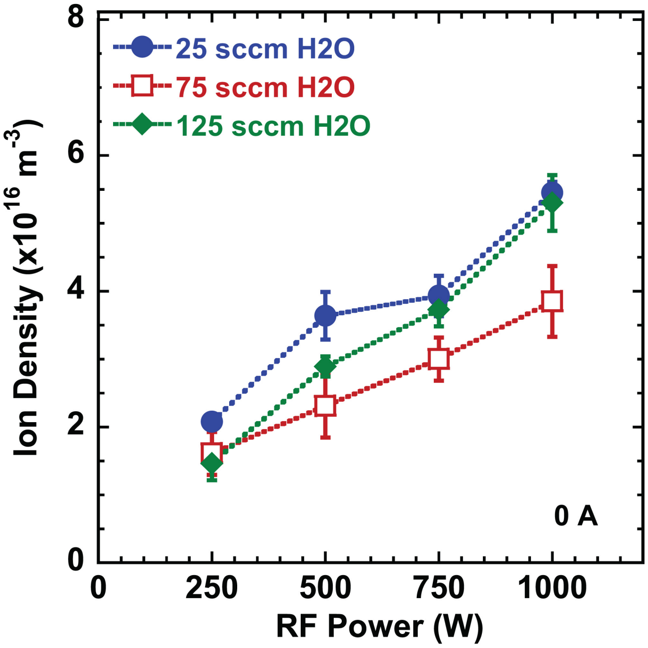

Figure 5.23: Ion density as a function of RF power for 25, 75, and 125-sccm water input flow rates without an applied magnet current.

resulting from an increase in deposited energy. Also similar to electron density, the ion density decreases with water input flow rates.

5.3.4 Optical Emission Spectra

Finally, optical emission spectra for variation in water vapor input flow rate are presented in Figures 5.25 and 5.26. The OH band is clearly identified in the UV range–281-303 nm and 305-330 nm. H_α at 656.3 nm and H_β at 486.1 nm are also observed. OH and H lines decrease as a function of water vapor flow rate. In particular, the hydrogen line at 656.3 nm significantly reduces from 25-sccm to 75-sccm water input flow rate. Both the OH band and the H lines decrease as water vapor input flow rate increases, indicating classic electron cooling. The trends showing a decrease in optical emission lines agree with the observed reduction in electron temperature with the water input flow rate.

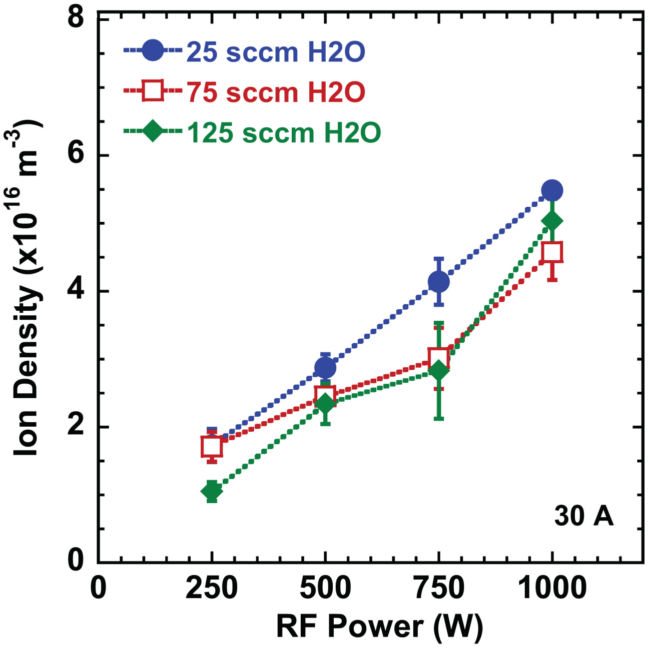

Figure 5.24: Electron density as a function of RF power for 25, 75, and 125-sccm water input flow rates with 30-A applied magnet current.

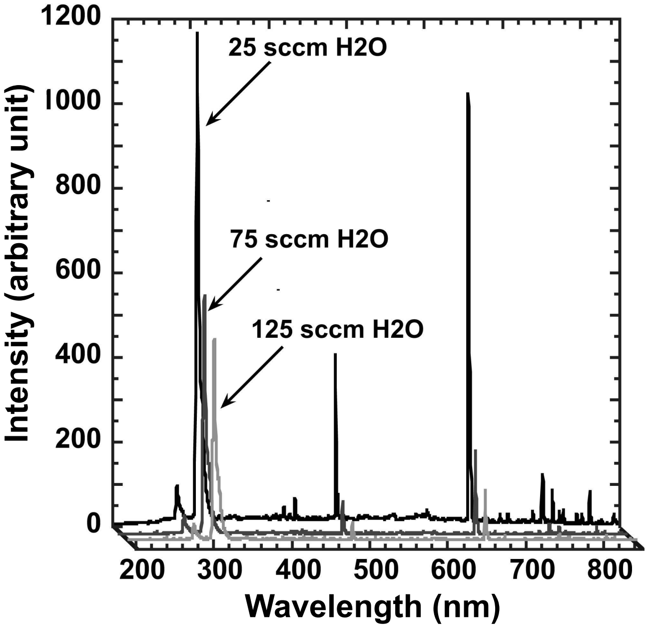

Figure 5.25: Optical emission spectra for 25, 75, and 125-sccm water input flow rates operating at 500-W RF power without an applied magnet current.

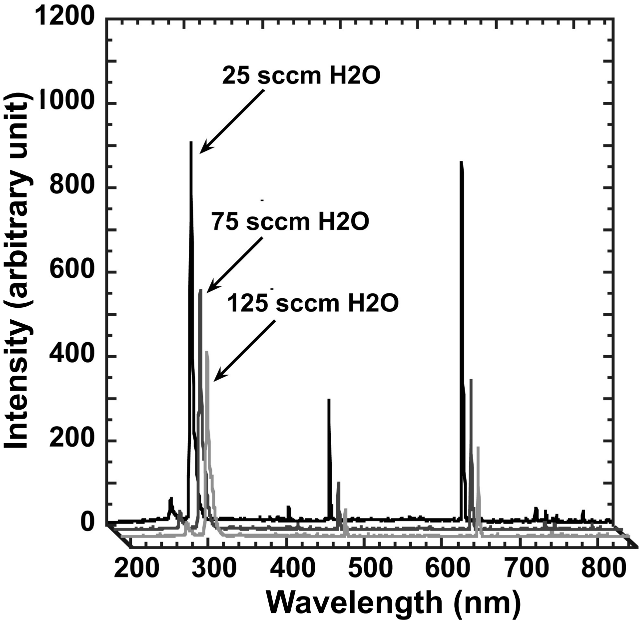

Figure 5.26: Optical emission spectra for 25, 75, and 125-sccm water input flow rates operating at 500-W RF power and 30-A applied magnet current.

5.3.5 Summary

It has been shown that at a fixed power, the water input flow rate affects hydrogen production rate. There is an optimum energy per molecule for dissociation. At a fixed RF power level, the rate of hydrogen production increases with water input flow rate up to 100 sccm and begins to reduce at 125 sccm. Although hydrogen and oxygen increase (by 50%) with water flow rate, the percent increase in hydroxyl is much higher in terms of percentage (by 800%). The absolute value for hydroxyl is influenced by the lack of an accurate calibration factor because hydroxyl was not used (see Section 4.2.1). Nevertheless, the trend shown here suggests that dissociative attachment processes are responsible for creating hydroxyl.

5.4 Conversion and Energy Efficiencies

The conversion and energy efficiencies to be discussed in this section are defined as:

$$\eta_{con} = \frac{\dot{m}_{H2,produced}}{\dot{m}_{H2O,input}} \tag{5.14}$$

$$\eta_{e} = \frac{\dot{m}_{H2} HHV_{H2}}{P_{in}} \tag{5.15}$$

where η_{con} is the conversion efficiency, η_e is the energy efficiency, HHV is the higher heating value of hydrogen (141.1 MJ/kg), and P_{in} is the power deposited in W.

Figures 5.27 and 5.28 show the conversion efficiency for the case with and without the applied magnetic field. The findings of this study show that the highest conversion efficiency is obtained at a lower water input flow rate. For 25-sccm water input flow rate, the conversion efficiency is 80%. The conversion efficiency decreases for a higher water input flow rate. For 75-sccm water input flow rate, the conversion efficiency is 30%, and for 125-sccm water input flow rate, the conversion efficiency reduces further to 22%.

While the conversion efficiency can be relatively high at a low water input flow rate, the energy efficiency is relatively low. Figures 5.29 and 5.30 show the energy efficiency for the case with and without the applied magnetic field. To convert sccm into kg/s, 1 sccm = 1.6×10^{-8} m^3/s, and for hydrogen at standard pressure (1 atm) and standard temperature (293 K), the density is 0.083 kg/m^3. Applying Equation 5.15, the energy efficiency for the case without and with magnetic field is shown in Figures 5.29 and 5.30. The maximum

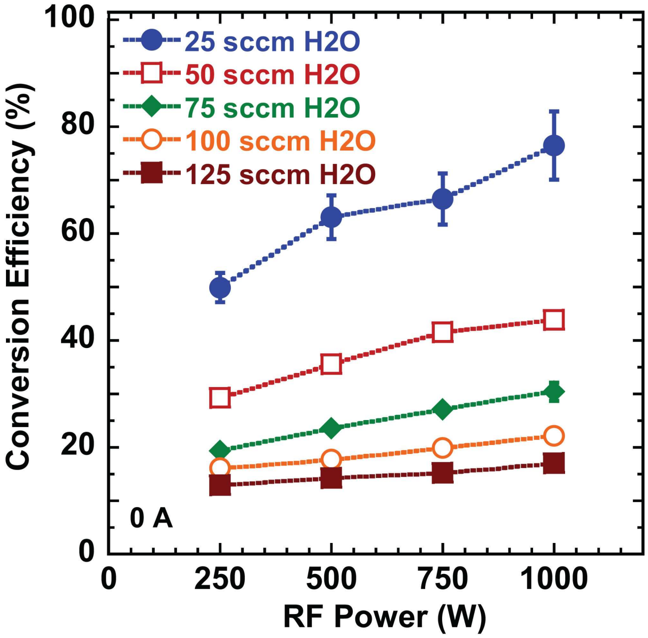

Figure 5.27: Conversion efficiency for the case without an applied magnetic field

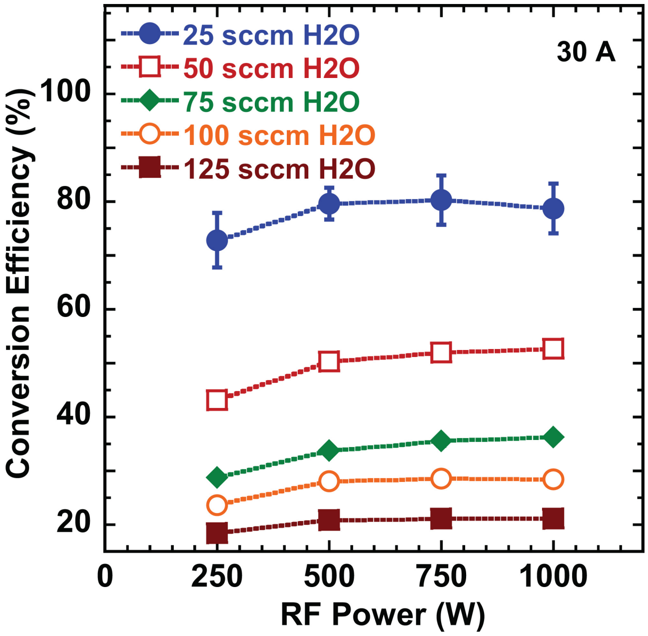

Figure 5.28: Conversion efficiency for the case with an applied magnetic field

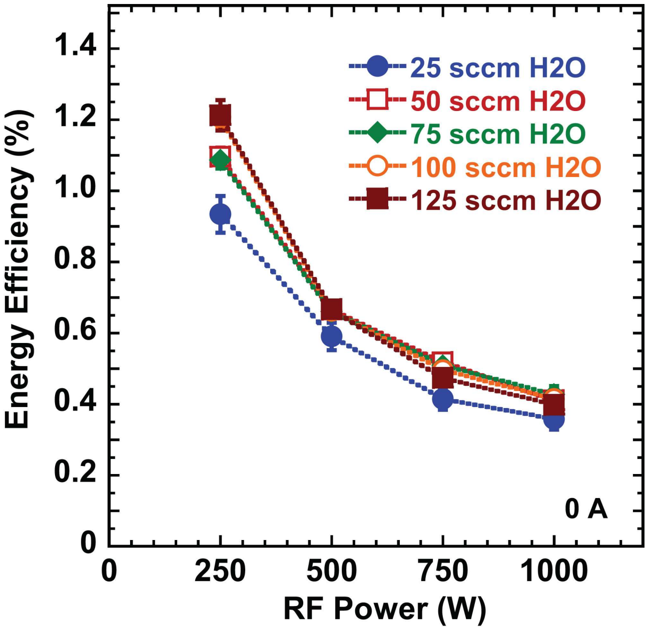

Figure 5.29: Energy efficiency for the case without an applied magnetic field

energy efficiency is obtained for the case with the higher water flow rate (125 sccm) and lowest RF power (250 W), and the efficiency is 1.7%. This is a very low value compared to the energy efficiency of electrolysis, 40-70% [45].

5.5 Summary of Experimental Results

Argon and water plasmas are compared and the effects of magnetic field strength and water vapor input flow rate on the hydrogen production rate are investigated in Sections 5.1–5.3. In this section, a summary of the results is given.

From the optical emission and residual gas analyzer spectra, it is shown that water molecules are dissociated in the plasma discharge operating on water vapor. With matching background pressure and operating conditions (RF power level and axial applied magnetic field strength), plasma properties of the discharge operating on argon are quite different

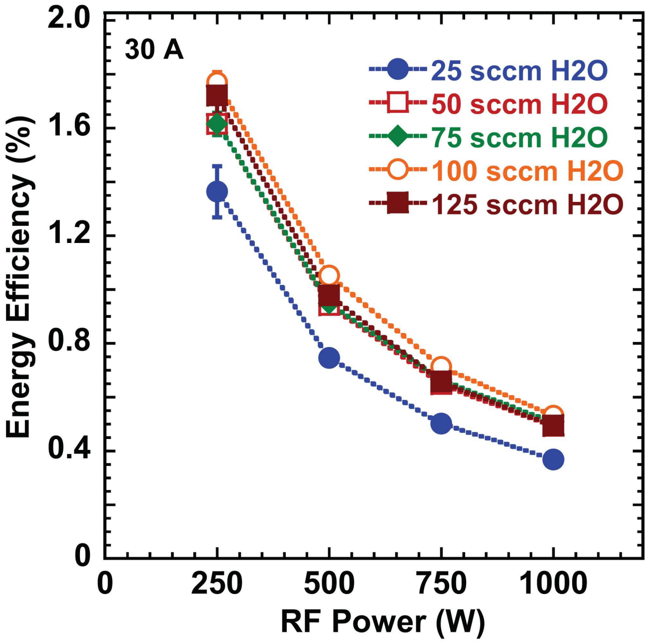

Figure 5.30: Energy efficiency for the case with an applied magnetic field

from those operating on water vapor. In particular, the argon plasma density is higher than that of the water plasma at similar RF power levels and background pressure. The ion density of the argon plasma ($n_i \approx n_e$ by quasineutrality) is up to two orders of magnitude higher than the electron density in the water discharge. The difference between the ion and electron densities in the water plasma is due to the presence of species with high electron affinity in the discharge.

The presence of the magnetic field is shown to affect the electron's diffusion from the production zones (in the annular region near the antenna) to the core of the discharge. As a function of magnetic field, the ion and electron densities at r = 0 location of the discharge reduce for both the argon and the water plasmas. However, for the water plasma, there are additional electron loss mechanisms in the core of the discharge, mainly via three-body collision attachment or dissociative attachment with species that have high positive electron affinities.

A relationship is obtained for both the electronegative and the electropositive plasma between the plasma potential, floating potential, and electron temperature. These relationships are derived by setting the total positive current equal to the total negative current, and they show that the difference between the plasma and the floating potential is only a weak function of the electronegativity and the relative ion mass. Therefore, the difference between the plasma and floating potential is more likely due to the increase in electron temperature. The plasma potential (and therefore the floating potential) of the water plasma is higher than that of the argon plasma. It is discussed that in order for the water plasma to maintain quasineutrality when the electron density is low (on the order of 10^{15} m^{-3} compared to the argon plasma's ion density at 10^{17} m^{-3}), the plasma potential of the water plasma must be higher than that of the argon plasma in order to set up the electric field needed to achieve ambipolar diffusion.

In general, when water flow rate increases, the hydroxyl production rate increases at a higher rate in terms of percent increase than hydrogen or oxygen production. Electron temperature decreases with increasing water flow rate, and OES spectra concurrently show the reduction in H emission lines and OH bands, suggesting electron cooling.

Finally, the conversion efficiency as high as 80% is measured. Conversion efficiency decreases as the water input flow rate increases. The maximum energy efficiency is relatively low (1.7%), which is lower than what has been achieved in conventional electrolysis, 40-70%.

Chapter VI

Kinetic Simulation Setup and Results

This chapter describes the zero-dimensional kinetic model Global_Kin that is used to estimate the upper limit theoretical conversion and energy efficiencies. Following the description of the model, the reactions considered in this model are presented in Section 6.2. In Section 6.3, the computational results are given. The electron number density and electron temperature are examined as a function of water input flow rate. A comparison between the theoretical and experimental efficiencies is presented.

6.1 Reactions

This model considers 28 species and 283 gas phase and electron impact reactions (see Appendix A). For the gas phase reactions, the production rate coefficients are given in Arrhenius form as shown in Equation 6.1.

$$k(T_g) = AT^b e^{\left(\frac{-E_A}{R_u T_g}\right)} \tag{6.1}$$

where A, b, and E_A are empirical parameters obtained from experiments for each gas phase reaction. E_A is the activation energy and R_u is the universal gas constant.

For the electron impact reactions, the reaction rate coefficients are obtained as shown in Equation 6.2:

$$k(T_e) = \int_0^{\infty} f(\epsilon)\left(\frac{2\epsilon}{m}\right)^{0.5} \sigma(\epsilon)d\epsilon \tag{6.2}$$

where ϵ is the electron energy and σ is the electron impact cross section.

In Global_Kin, a collection of Arrhenius parameters and cross sections are available in a database. Table 5.1 shows the reactions added to the data file to account for electron impact reactions with water.

The cross sections for elastic and inelastic electron collisions with water are compiled in a literature review by Itikawa and Mason in Reference 88. An interpolation tool is used to obtain a continuous curve for the cross sections in order to perform the integration as shown in Equation 6.2. The cross sections are shown in Figure 5.3.

6.2 Description of Global Kinetic Model

A global, zero-dimensional kinetic model called Global_Kin is used to study the dissociation of water molecules in a plasma source [90–93]. The plasma discharge is modeled as a cylinder with radius R and length L as shown in Figure 6.1. In this simulation, the water flow rate into the chamber and the gas pressure are kept constant for each simulation. Power is deposited into the discharge as a function of time. It is set to ramp up from zero to a pre-set level in 5 μs, and then it remains constant for the duration of the simulation that is typically of a few seconds. Therefore, the power level is essentially constant with time.

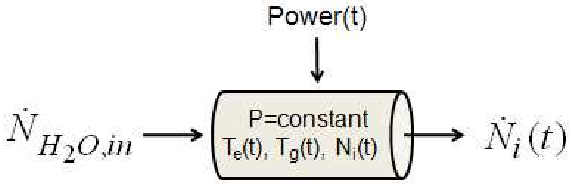

Figure 6.1: Schematic diagram of plasma discharge corresponding to computational model.

The code outputs gas temperature, electron temperature, and species density as a function of time.

The number density inside the chamber is dependent on both the gas temperature and pressure, following the ideal gas law shown in Equation 6.3.

$$P = Nk_BT_{gas} \tag{6.3}$$

Thus, when the gas temperature increases or when gas dissociation occurs, the gas must expand to maintain a constant pressure. A description of the model provided here follows the example of Stafford in Ref. 90.

In the zero-dimensional (0-D) kinetic model, Global_Kin assumes a homogeneous plasma where the concentration of species is spatially independent. Global_Kin has three modules: an offline Boltzmann solver module, a plasma chemistry and transport module, and an ordinary differential equation (ODE) solver module. The scheme of the simulation is shown in Figure 6.2. The code works in the following manner: The chemistry and transport module constructs continuity equations for neutral and charged species. The time rate of change of a neutral species as shown in Equation 6.4 is accounted for by diffusion to the wall, diffusion from the wall, reaction sources and gas expansion. The time rate of change of

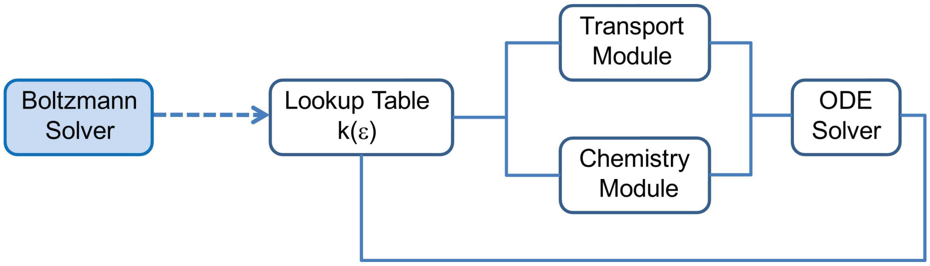

Figure 6.2: Simulation scheme of Global_Kin.

charged species as shown in Equation 6.5 is a result of ambipolar diffusion and reaction sources.

$$\frac{dN_i}{dt} = -\nabla \cdot \left(-\nabla \left(D_i N_i \right) + \sum_j \nabla \cdot \left(D_i N_j \right) \gamma_j f_{ij} \right) + S_i - \frac{N_i}{T_g} \frac{dT_g}{dt} \tag{6.4}$$

$$\frac{dN_i^{\pm}}{dt} = -\nabla \cdot \left[-\nabla \left(D_{a,i} N_i \right) \right] + S_i \tag{6.5}$$

In Equations 6.4 and 6.5, N_i is the density of neutral species i, $N_{\pm}$ is the density for charged species, γ_j is the wall reactive sticking coefficient of species j, D_i and $D_{a,i}$ are the diffusivity and the ambipolar diffusivity of species i in the mixture, f_{ji} is the returned fraction of species j as species i from the wall, S_i is the reaction source term for species i, and T_g is the gas temperature. The ambipolar diffusion coefficients for charged species are based on instantaneous ion and electron mobilities and diffusivities. The details of this model are further described in References 90, 91.

One simplification can be made in a 0-D model by substituting the diffusion length Λ for the partial derivatives is shown in Equation 6.6:

$$\frac{dN_i}{dt} = \frac{1}{\Lambda^2}\left(-D_i N_i + \sum_j D_i N_j \gamma_j f_{ij}\right) + S_i - \frac{N_i}{T_g}\frac{dT_g}{dt} \tag{6.6}$$

In Equation 6.6, ∇^2 is approximated as $1/\Lambda^2$.

The source term for the gas phase reactions and the electron impact reactions are described as follows:

$$S_i = \sum_j \left(a_{ij}^{RHS} - a_{ij}^{LHS}\right) k_j \prod_l N_l^{a_{ij}^{LHS}} \tag{6.7}$$

In Equation 6.7, a_{ij} is the stoichiometric coefficients of species i in reaction j on the right hand side and left hand side, and k_j is the reaction rate coefficient for reaction j. In the chemistry and transport module, the differential equations are set up to solve for the gas and electron temperature. The energy conservation equation (Equation 6.8) for the heavy species includes contribution to gas heating from elastic and inelastic collisions with electrons, gas phase reaction sources, and conduction to the walls, and the transfer of internal energy to kinetic energy as the gas expands and flow velocity increases.

$$\begin{aligned}\frac{d}{dt}(N c_p T_g) = \sum_i \frac{3}{2} n_e \nu_{mi}\left(\frac{2m_e}{M_i}\right) k_B (T_e - T_g) + \sum_j n_e k_j N_j \Delta\epsilon_j \\ - \sum_j \Delta H_j + \frac{\kappa}{\Lambda^2}(T_w - T_g) - \frac{d}{dt}\left(\frac{1}{2} M_w N v_x^2\right)\end{aligned} \tag{6.8}$$

In Equation 6.8, N is the total gas density, c_p is the mixture averaged heat capacity, n_e is the electron number density, ν_{mi} is the momentum transfer collision frequency between electrons and species i, m_e is the electron mass, M_i is the mass of species i, k_B is the Boltzmann constant, T_e is the average electron temperature, k_j and $\Delta\epsilon_j$ are the rate constant and the energy contribution from inelastic process j, ΔH_j is the heat of reaction of process j, κ is the thermal diffusivity, and M_w is the mixture averaged molecular weight.

For electron heating, the energy conservation (Equation 6.9) accounts for Joule heating and energy transfer in elastic and inelastic collisions with heavy species:

$$\frac{d}{dt}\left(\frac{3}{2}n_e k_B T_e\right) = P_d - \sum_i \frac{3}{2}n_e \nu_{mi}\left(\frac{2m_e}{M_i}\right) k_B(T_e - T_g) + \sum_l n_e k_l N_l \Delta\epsilon_l \tag{6.9}$$

In Equation 6.9, P_d is the time-averaged power deposition into the electrons over many rf cycles. This model assumes that the power deposited into the system all goes into accelerating the electrons. When the electrons collide into other particles, they impart some of the energy into thermal energy–also known as Joule heating. Note that this model does not account for other types of heating such as stochastic heating or any wave-particle interaction. However, there is not a global kinetic model of plasma chemistry that can account for other modes of heating. Results from Global_Kin should still be a good first order of magnitude estimate when accounting for global kinetics.

As discussed in Section 6.1, the reaction rate coefficients for electron impact reactions require an integral of the EEDF and the cross sections (Equation 6.2). The cross sections are obtained from the literature. For the EEDF, it is obtained from the offline Boltzmann solver. The Boltzmann module solves the Boltzmann equation (Equation 6.10) for the

EEDF.

$$\frac{\partial f}{\partial t} + \vec{V} \cdot \nabla_{\vec{r}} f + \frac{\vec{F}}{m} \cdot \nabla_{\vec{v}} f = \left(\frac{\partial f}{\partial t}\right)_{col} \tag{6.10}$$

A table is generated for the average electron energy, transport coefficients, and the rate coefficient constants, k, for a range of electric field/density (E/N). The EEDF changes with the composition of the gas mixture, and therefore the Boltzmann solver is invoked at specified intervals during the simulation to account for this change. After the transport coefficient and rate coefficients are calculated and tabulated for a range of E/N, the ODE equations (Equations 6.4 - 6.9) are integrated using the stiff ODE solver developed at Lawrence Livermore National Laboratory [94].

6.3 Simulation Results

This section presents the simulation results. First, the model conditions are matched with those in the experiment: RF power is varied between 500 and 1000 W for a range of water vapor flow rates (25, 50, 75, 100, and 125 sccm). The operating pressure is set to match those measured in the experiment. A study of energy efficiency is then carried out independently as a function of background pressure and water vapor input flow rate. Note that this simulation does not account for any magnetic field effect; the plasma is assumed to be isotropic.

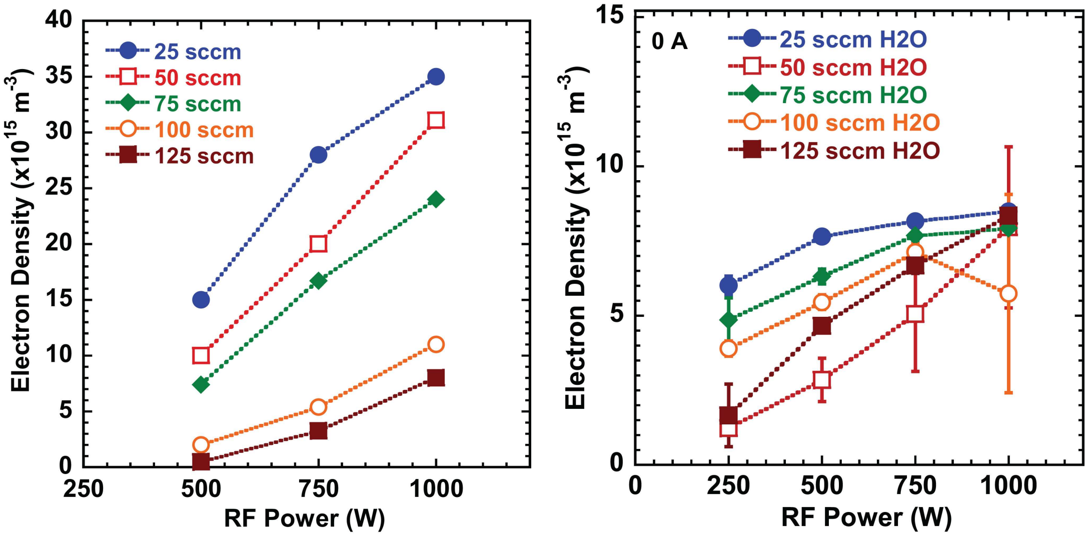

(a) Computational results.

(b) Experimental results.

Figure 6.3: (a) Computational and (b) experimental results for electron density as a function of RF power for 25, 50, 75, 100, and 125-sccm water input flow rates without an applied magnet current.

6.3.1 Effects of Flow Rate on Electron Number Density

Figure 6.3(a) shows the calculated electron density as a function of RF power for 25, 50, 75, 100, and 125-sccm water input flow rate. The electron density is shown to range from 1×10^{15} to 35×10^{15} m^{-3}, within the same order of magnitude as that determined in the experiment, reproduced in Figure 6.3(b). The results clearly show that the electron density increases with RF power and decreases with water input flow rate. Again, at a fixed power level, a decrease in flow rate increases the energy available per molecule, therefore causing more dissociation and ionization. This agrees qualitatively with the experimental results.

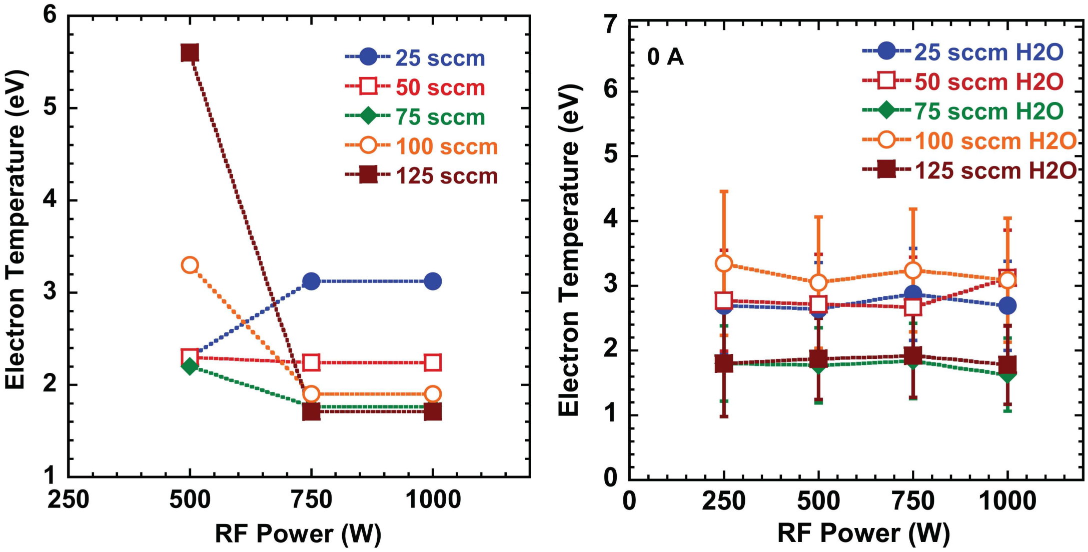

(a) Computational results.

(b) Experimental results.

Figure 6.4: (a) Computational and (b) experimental results for electron temperature as a function of RF power for 25, 50, 75, 100, and 125-sccm water input flow rates without an applied magnet current.

6.3.2 Effects of Flow Rate on Electron Temperature

Figure 6.4(a) shows the electron temperature for the same set of operating conditions as described in Section 6.3.1. The electron temperature ranges from 2 to 3 eV, which closely matches the experimental results, reproduced from Chapter 5 in Figure 6.4(b). Similar to the experimental results, the electron temperature is not affected by RF power. The result for 125 sccm at 500-W RF power is high relative to the other conditions because at low RF power and high water flow rate, the electron temperature needs to be relatively high in order to have adequate ionization to sustain the discharge.

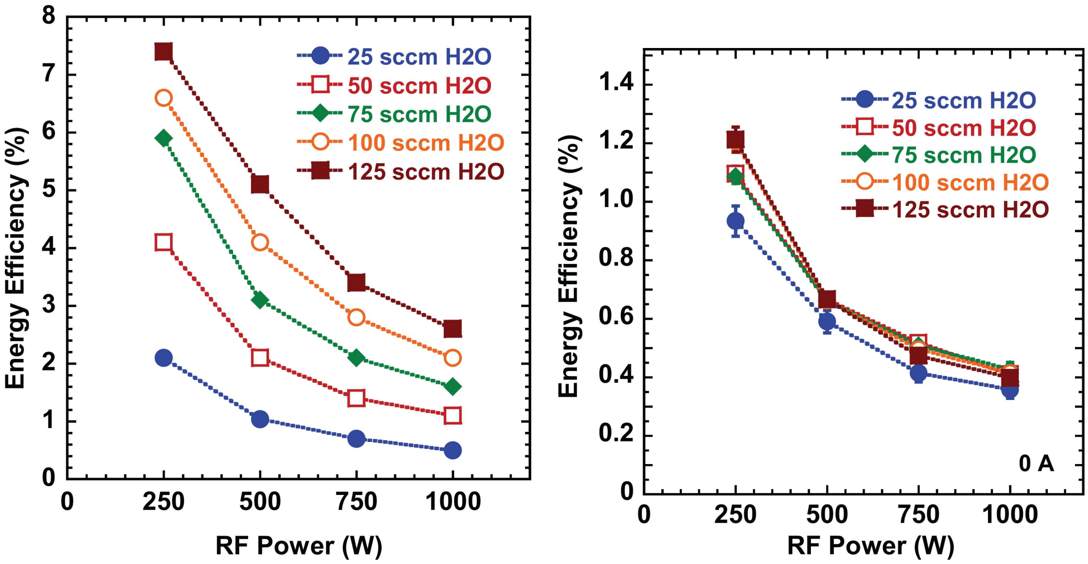

(a) Computational results.

(b) Experimental results.

Figure 6.5: (a) Computational and (b) experimental results for energy efficiency as a function of RF power for 25, 50, 75, 100, and 125-sccm water input flow rates without an applied magnet current.

6.3.3 Effects of Flow Rate on Energy and Conversion Efficiencies

Figure 6.5(a) shows the energy efficiency as defined in Equation 5.15. It illustrates that the energy efficiency increases with water vapor input flow rate and decreases with RF power. Again, the background pressure for each corresponding flow rate is set to match the experimental value. In general, the energy efficiency decreases with increasing fractional dissociation as power goes into producing fragments. Therefore, the trend observed here is physical. It also suggests that in order to increase the energy efficiency of hydrogen production in a plasma discharge, throughput is an important parameter. For 125 sccm water flow rate, the maximum energy efficiency is 7.5% if 250-W RF power is applied.

Figure 6.5(b) shows the corresponding energy efficiency obtained experimentally. The trend is similar to that observed in the simulation results: the energy efficiency increases with flow rate and decreases with RF power. The maximum experimental energy efficiency for 125 sccm flow rate at 250 W is 1.2%, which is relatively lower than what is predicted by the simulation. The experimental energy efficiency is lower than the computational energy efficiency mainly because the experimental efficiency is determined using the results from the RGA, and there are loss mechanisms in the hydrogen gas as it traveled from the production zone (in the plasma discharge) to the detector (RGA chamber). For example, hydrogen can easily be absorped to the metal surfaces of the chamber. Therefore, it is expected that the rate of hydrogen production is higher than what the RGA measured. Further, the simulation did not account for all the possible inherit loss mechanisms (*e.g.* wall loss), therefore, the simulation result only gives an upper limit value. In reality, the energy efficiency is a value between what was measured experimentally and what was calculated computationally.

The theoretical conversion efficiency for 125 sccm is 80%. The conversion efficiency obtained from the experiment is 24% for 125 sccm water flow rate and 80% for 25 sccm water flow rate.

6.3.4 Effects of Background Pressure on Energy Efficiency

The computational results presented thus far are for conditions that match those available in the experiment. And they show that the maximum energy efficiency is 7.5%. Next, the operating pressure and the water input flow rate are independently studied to determine their effects on the energy efficiency.

Figures 6.6 shows the energy efficiency as a function of water input flow rate for 50-500

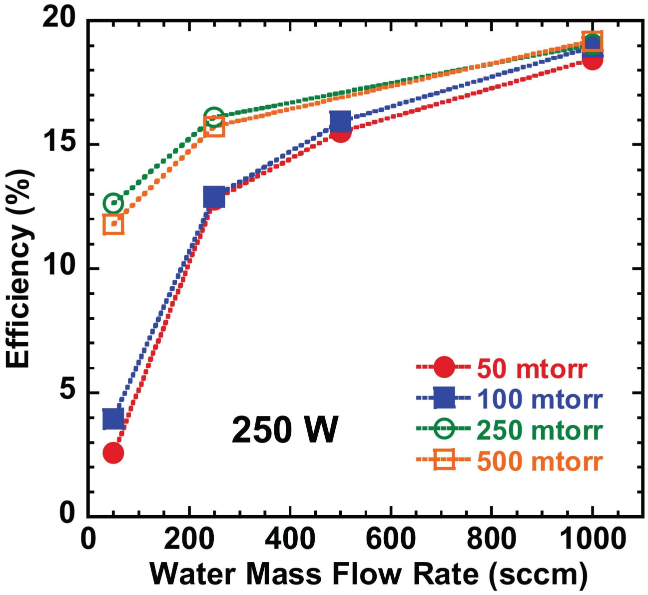

Figure 6.6: Energy efficiency for operation with 250-W RF power as a function of water vapor input flow rate for 50, 100, 250, and 500 mtorr.

mtorr pressure range and for 250-W RF power. The energy efficiency is shown to increase with pressure. At higher pressure, diffusion losses for electrons and ions are lowered, and therefore, the plasma is produced more efficiently. It is also shown that the energy efficiency increases with water input flow rate, similar to Figure 6.5(a). Finally, these results show that the energy efficiency is optimized if the plasma discharge can operate at a significantly higher water input flow rate and a higher pressure. The theoretical conversion efficiency at 1000 sccm water input flow rate is 25%. A dielectric barrier discharge or plasma torch may provide higher energy efficiencies than the current system employed in the experimental investigation.

6.4 Summary

In summary, when the operating conditions match those in the experimental investigation, the simulated electron temperature closely matches the experimental results. The simulated electron density is greater than experimental results by a factor between two and four. However, it is shown that in order to increase the energy efficiency, the ability to operate and sustain the plasma discharge at higher flow rates is needed. In a large range of background pressure (50-500 mtorr), the energy efficiency increases with water input flow rate. Thus, the water input flow rate is a critical parameter to optimize the energy efficiency in this method of hydrogen production.

Chapter VII

Conclusions and Future Work

7.1 Conclusions

The aim of this dissertation research project was to evaluate the feasibility of hydrogen production through a method of dissociating water vapor in a radio-frequency plasma source and to study the basic behaviors in a water plasma discharge. The expected shortage of future energy resources and climate change have motivated development of innovative techniques to satisfy energy demand while minimizing emissions. To this end, hydrogen as an alternative non-carbon transportation energy source is an attractive option. The technical challenge, however, is to extract hydrogen from water at a low cost and a high efficiency. This work investigated the feasibility of producing hydrogen in a radio-frequency plasma discharge operating on water vapor. Additionally, water plasma has many applications in other research areas. The information on basic behaviors of a water plasma discharge will provide fruitful insights for other researchers. The following summarizes works that have be done and outlines the main conclusions.

7.1.1 Water Plasma Source Development

To carry out this investigation, a radio-frequency plasma discharge was designed to operate on water vapor. A water delivery system was constructed to allow for an accurate measurement and control of the water input flow rate. To characterize the discharge, a Langmuir probe and optical emission spectrometers were used. In addition, a RGA was calibrated to estimate the rate of hydrogen production. In order to operate the RGA, a differential pump system was designed and constructed.

7.1.2 Electronegative and Electropositive Plasmas Comparison

The water plasma has been identified as an electronegative plasma due to the presence of species that have high positive electron affinities such as O_2 and OH. To understand how the water plasma behaves differently from an electropositive plasma, a comparison of plasma properties of the water and argon plasmas is made. The argon and water plasmas operated at the same background pressures and operating conditions and the following summarizes the comparison:

- Based on the LP results obtained at the $r = 0$ location downstream of the discharge, the argon plasma's ion density is higher than the ion density (by up to one order of magnitude) and the electron density (up to two orders of magnitude) of the water plasma.
- The electron temperature of the argon plasma is one eV higher than that of the water plasma.

- The floating and plasma potential of the argon plasma is lower than those of the water plasma.

7.1.3 Water Plasma Properties and Hydrogen Production Characterization

The plasma discharge was operated on water vapor and through the optical emission and RGA spectra, it was confirmed that dissociation of water molecules in the discharge was achieved. The effects of RF power, magnetic field strength, and water input flow rate on the rate of hydrogen production and plasma properties were investigated.

- In the absence of the applied magnetic field, the hydrogen production rate increases linearly with RF power.

- In the presence of the axial magnetic field, the hydrogen production rate increases with RF power from 250 W to 500 W, but begins to saturate in most cases after 500 W.

- At a fixed RF power level, the rate of hydrogen production initially increases with water vapor input flow rate up to 100 sccm, but begins to decrease after that.

- As the water vapor input flow rate increases, the rate of hydrogen and oxygen production increases (up to 50%), and the rate of hydroxyl production increases more significantly in terms of percentage (up to 800%).

- Local measurements at the axis of symmetry for the plasma discharge (r = 0 location) downstream of the discharge show that electron density increases with RF power but decreases with applied axial magnetic field for a fixed water input flow rate. For a fixed power level, the electron density decreases with water input flow rate.

- The floating and plasma potential increases with applied magnetic field and with water input flow rate.
- The electron temperature is not affected by the RF power or the applied axial magnetic field.
- The difference between the plasma potential and the floating potential is a weak function of the electronegativity and the relative ion mass in the water plasma.

7.1.4 Water Plasma Behaviors

For the main results summarized in Sections 7.1.2 and 7.1.3, the following offers some explanations for the observed trends and describes the behavior of the water plasma.

In the argon plasma, collisional energy losses include electronic excitation and ionization. For the water plasma, these also include excitation of rotational and vibrational energy levels, and molecular dissociation. Therefore, the available energy-per-molecule in a water plasma is lower than that of the argon plasma. This explains why the water plasma has lower plasma densities. In addition, in the presence of the applied axial magnetic field, the positive and negative ions are free to diffuse from the production zone in the annular region near the antenna into the core of the discharge. However, electrons are confined to the production region because their mobility in the direction perpendicular to the field lines is significantly reduced. For those electrons that are able to diffuse into the discharge, they are likely to be consumed through three-body electron attachment or dissociative attachment processes in the core, due to the presence of species with high electron affinities in that region.

The plasma potential of the water plasma is higher than that of the argon plasma, and this is possibly due to the water plasma having a lower electron density. Quasineutrality is maintained even in the water plasma. The positive ion density is balanced with the sum of the negative ion density and electron density. Because the electron density is low in the water plasma, the plasma potential must increase to set up the electric field needed to bring the electrons to the core to maintain quasineutrality.

In the absence of the applied axial magnetic field, for a fixed water input flow rate, the increase in RF power effectively increases the energy available per molecule. Therefore, it is seen that the rate of hydrogen production increases linearly with RF power. However, in the presence of the applied axial magnetic field, the electrons cannot easily diffuse into the core of the discharge because their radial mobility coefficient is significantly reduced. Therefore, electron-impact reactions with water molecules are limited to the annular region near the antenna. As RF power increases, the electron density increases, but in the presence of the magnetic field, the electrons are confined to the small annular region. Consequently, electron-impact reactions with water molecules in the core of the discharge are reduced, which may explain the saturation of the hydrogen production rate with RF power observed when there is an applied axial magnetic field.

7.1.5 Computational Work

The experimental work offered insights on the properties and behaviors of a plasma discharge operating on water. Based on the current setup, the energy efficiency for hydrogen production is less than 1.7%. However, the experimental setup is not optimized for achieving high efficiency. In particular, in the current experimental setup, one cannot independently control the water input flow rate and the background pressure. This and other limitations, along with the desire to estimate the theoretical efficiency of hydrogen production using a plasma discharge–where the dissociation is mostly dominant by electron-impact reactions–motivated the computational investigation.

Using a zero-dimensional global kinetics model Global_Kin, it was shown that the trends in electron density and temperature from the computational results closely match those in the experimental work when operating conditions are similar. The computational investigation shows that energy efficiency is optimized by increasing water input flow rate. Hence, the study of the effect of water input flow rate–in the ranges outside those available in the experiment–along with operating pressures was performed. It was determined that the energy efficiency is highest when water input flow rate and pressure are the highest. The maximum theoretical energy efficiency achieved was almost 20% with a flow rate of 1000 sccm, and the maximum theoretical conversion efficiency achieved was 80% with a flow rate of 125 sccm.

In conclusion, this experimental work shows that although it is feasible to dissociate water molecules for hydrogen production via electron impact reactions, the energy efficiency is too low to make this an economic choice compared with the current technologies through electrolysis. However, through this work, properties and behaviors of a water plasma discharge can provide helpful insights for future research which may take advantage of some of the properties of the water plasma.

7.2 Suggestions for Future Work

This dissertation work has shown that hydrogen production in an RF plasma source is feasible, but the current system is not optimized for energy efficiency. Both experimental and computational results point to the need to increase the water input flow rate. The following outlines suggestions for future work, for both the current plasma source setup and ideas for the development of a different system.

7.2.1 Current Experimental Setup

To further this current work to understand the behavior of the water plasma in a low-pressure regime, a radial profile of electron density inside the discharge is valuable. However, because the electron density is too high in the annular region closest to the antenna, a Langmuir probe is not recommended. In addition, the presence of the physical probe would affect the measurement. Therefore, alternative methods of measuring electron density through the method of interferometry or other non-intrusive methods are recommended. Further, to increase the energy efficiency, one can also study the effect of a seed gas on the dissociation rate. A metastable atom can help in the dissociation process of the water molecules in the discharge. If a helicon-type plasma source is used, a concentric geometry with the gap distance equal the skin depth layer thickness is recommended. This geometry would maximize the heating zone.

The existing plasma discharge setup can only operate at relatively low pressures, below 500 mtorr. However, the current vacuum pump is limited to only 35 m^3/hr on N_2. Therefore, a different pumping system with a higher pumping speed will allow one to experimentally investigate the regime where the flow rates are high but the pressures are low. Finally, the hydrogen and oxygen gas produced in the existing system are being pumped out of the system through a vacuum pump. However, a design of the hydrogen-oxygen separation system is needed.

7.2.2 New System Development

The previous section suggests some future work that can be done to the current system to provide more information on the plasma properties or to allow the existing system to operate in the different regimes. However, as both experimental and theoretical results have shown, in order to increase the energy efficiency of this method, the water input flow rates must drastically increase. As such, operating the water plasma source at higher pressures are desirable. Therefore, the current design of the low-pressure plasma source is not recommended. Therefore, an entirely new system is suggested. For example, dielectric barrier discharges or some types of plasma torch are recommended because these are known to behave very well at high pressures and high flow rates. In addition, for reasons that are to be discussed in the next section, a removal of the entire pumping system (atmospheric operation) is desired.

7.2.3 Other Applications

This work began by examining the feasibility of breaking up the O-H bonds in the water molecules. The motivation is to produce hydrogen to address the energy and climate challenges, and to provide basic characterization of the water plasma discharges. However, in its current stage, the conversion and energy efficiencies are relatively low compared to what can be obtained from electrolysis that the proposed method cannot be competitive with electrolysis, despite some disadvantages in electrolysis.

Even though the energy efficiencies are still an issue for hydrogen production, this work reveals that dissociation of other molecules via electron-impact is possible and can be of benefits in other applications. In particular, work has begun at PEPL to investigate the feasibility of dissociating carbon dioxide gases in the plasma discharge [95]. Similar to the application of hydrogen production, the ability to operate with high flow rate and high pressure is recommended for this application of CO_2 dissociation.

Moreover, this experimental work has demonstrated that the RF plasma source can break up water molecules to produce highly useful radicals such as O and OH. Therefore, if the cost of the overall system can be reduced (*e.g.* removing the vacuum pump system), the water plasma discharge can be used in medical applications: *i.e.* sterilization of medical instruments.

Appendix A

GlobalKin Data File

```
!
! Species
!
E              :  0.00 ; -1 ] 0.    [   0.  $ 5.46E-4 # 1.00 { 0.00 } E    !
O2             :  0.00 ;  0 ] 3.467 [ 106.7 $  31.999 # 0.00 { 0.00 } O2   !
O2V            :  0.20 ;  0 ] 3.467 [ 106.7 $  31.999 # 0.20 { 1.00 } O2   !
O2*            :  0.98 ;  0 ] 3.467 [ 106.7 $  31.999 # 1.E-5 { 1.00 } O2  ! R9
O2*1S          :  1.63 ;  0 ] 3.467 [ 106.7 $  31.999 # 0.02 { 1.00 } O2   ! R9
O2^            : 12.14 ;  1 ] 3.467 [ 106.7 $  31.999 # 1.00 { 1.00 } O2   !
O2-            : -.498 ; -1 ] 3.467 [ 106.7 $  31.999 # 1.00 { 1.00 } O2   !
O              :  2.58 ;  0 ] 3.050 [ 106.7 $  15.999 # 0.02 { 0.50 } O2   !
O*             :  4.54 ;  0 ] 3.050 [ 106.7 $  15.999 # 1.0  { 1.00 } O    ! R9
O1S            :  6.78 ;  0 ] 3.050 [ 106.7 $  15.999 # 1.0  { 1.00 } O    ! R9
O^             : 16.26 ;  1 ] 3.050 [ 106.7 $  15.999 # 1.00 { 1.00 } O    !
O-             : 1.056 ; -1 ] 3.050 [ 106.7 $  15.999 # 1.00 { 1.00 } O    !
O3             :  1.47 ;  0 ] 3.467 [ 106.7 $  48.0   # 0.00 { 0.00 } O3   !
O3-            : -.504 ; -1 ] 3.467 [ 106.7 $  48.0   # 1.00 { 1.00 } O3   !
H2O            : -2.51 ;  0 ] 2.641 [ 809.1 $  18.015 # 0.00 { 0.00 }      !
H2O^           :  10.2 ;  1 ] 2.641 [ 809.1 $  18.015 # 1.00 { 1.00 } H2O  !
H3O^           :  6.25 ;  1 ] 0.    [   0.  $  19.023 # 1.00 { 1.00 } H2O  !
OH             :  .387 ;  0 ] 3.147 [  79.8 $  17.007 # 0.00 { 0.00 }      !
OH-            :  -1.5 ; -1 ] 3.147 [  79.8 $  17.007 # 1.00 { 1.00 } OH   !
OH^            :  13.5 ;  1 ] 3.147 [  79.8 $  17.007 # 1.00 { 1.00 } OH   !
HO2            :  .130 ;  0 ] 0.    [   0.  $  33.007 # 0.00 { 0.00 }      !
H              :  2.26 ;  0 ] 2.708 [  37.0 $   1.008 # 0.02 { 0.01 } H2   !
H-             :  1.44 ; -1 ] 2.708 [  37.0 $   1.008 # 1.00 { 1.00 } H    !
H^             :  15.9 ;  1 ] 2.710 [  37.0 $   1.008 # 1.00 { 1.00 } H    !
H2             :  0.00 ;  0 ] 2.827 [  59.7 $   2.016 # 0.00 { 0.00 }      !
H2^            :  15.5 ;  1 ] 0.    [   0.  $   2.016 # 1.00 { 1.00 } H2   !
H2O2           :  -1.4 ;  0 ] 0.    [   0.  $  33.999 # 0.00 { 0.00 }      !
O2^*H2O        :  0.00 ;  1 ] 0.    [   0.  $  50.014 # 1.00 { 1.00 } O2   !
H3O^*H2O       :  0.00 ;  1 ] 0.    [   0.  $  37.038 # 1.00 { 1.00 } H2O  !
XWAT           :  0.00 ;  1 ] 0.    [   0.  $  55.053 # 1.00 { 1.00 } H2O  !
X1WAT          :  0.00 ;  0 ] 0.    [   0.  $  54.045 # 0.00 { 0.00 }      !
M              :  0.00 ;  0 ] 0.    [   0.  $   1.000 # 0.00 { 0.00 }      !
TE             :  0.00 ;  0 ] 0.    [   0.  $   1.000 # 0.00 { 0.00 }      !
TGAS           :  0.00 ;  0 ] 0.    [   0.  $   1.000 # 0.00 { 0.00 }      !
EDEP           :  0.00 ;  0 ] 0.    [   0.  $   1.000 # 0.00 { 0.00 }      !
PDEP           :  0.00 ;  0 ] 0.    [   0.  $   1.000 # 0.00 { 0.00 }      !
PEBDEP         :  0.00 ;  0 ] 0.    [   0.  $   1.000 # 0.00 { 0.00 }      !
SPEED          :  0.00 ;  0 ] 0.    [   0.  $   1.000 # 0.00 { 0.00 }      !
POSITION       :  0.00 ;  0 ] 0.    [   0.  $   1.000 # 0.00 { 0.00 }      !
MIS            :  0.00 ;  0 ] 0.    [   0.  $   1.000 # 0.00 { 0.00 }      !
*
!
! Electron impact reactions
!
E + O2 > O2 + E          : 0.00E+00 [ 0.00 ]  0.0  !  -400 $0&   0. #  0. %
E + O2 > O- + O          : 0.00E+00 [ 0.00 ]  0.0  !  -401 $0&   0. #  0. %
E + O2 > O2V + E         : 0.00E+00 [ 0.00 ]  0.0  !  -403 $0&   0. #  0. %
E + O2 > O2V + E         : 0.00E+00 [ 0.00 ]  0.0  !  -404 $0&   0. #  0. %
E + O2 > O2V + E         : 0.00E+00 [ 0.00 ]  0.0  !  -405 $0&   0. #  0. %
E + O2 > O2V + E         : 0.00E+00 [ 0.00 ]  0.0  !  -406 $0&   0. #  0. %
E + O2 > O2* + E         : 0.00E+00 [ 0.00 ]  0.0  !  -407 $0&   0. #  0. %
E + O2 > O2*1S + E       : 0.00E+00 [ 0.00 ]  0.0  !  -408 $0&   0. #  0. %
E + O2 > O + O + E       : 0.00E+00 [ 0.00 ]  0.0  !  -411 $0&   0. #  0. %
E + O2 > O* + O + E      : 0.00E+00 [ 0.00 ]  0.0  !  -412 $0&   0. #  0. %
E + O2 > O2^ + E + E     : 0.00E+00 [ 0.00 ]  0.0  !  -415 $0&   0. #  0. %
E + O2 > O^ + O + E + E  : 0.00E+00 [ 0.00 ]  0.0  !  -417 $0&   0. #  0. %
!
```

```
E + O2V > O2V + E        : 0.00E+00 [ 0.00 ]  0.0  ! -2093 $0&   0. #  0. %
E + O2V > O- + O         : 0.00E+00 [ 0.00 ]  0.0  ! -2094 $0&   0. #  0. %
E + O2V > O2 + E         : 0.00E+00 [ 0.00 ]  0.0  ! -2096 $0&   0. #  0. %
E + O2V > O2* + E        : 0.00E+00 [ 0.00 ]  0.0  ! -2097 $0&   0. #  0. %
E + O2V > O2*1S + E      : 0.00E+00 [ 0.00 ]  0.0  ! -2098 $0&   0. #  0. %
E + O2V > O + O + E      : 0.00E+00 [ 0.00 ]  0.0  ! -2099 $0&   0. #  0. %
E + O2V > O* + O + E     : 0.00E+00 [ 0.00 ]  0.0  ! -2100 $0&   0  #  0. %
E + O2V > O2^ + E + E    : 0.00E+00 [ 0.00 ]  0.0  ! -2103 $0&   0. #  0. %
E + O2V > O^ + O + E + E : 0.00E+00 [ 0.00 ]  0.0  ! -2105 $0&   0. #  0. %
!
E + O2* > O2* + E        : 0.00E+00 [ 0.00 ]  0.0  ! -2057 $0&   0. #  0. %
E + O2* > O- + O         : 0.00E+00 [ 0.00 ]  0.0  ! -2058 $0&   0. #  0. %
E + O2* > O2V + E        : 0.00E+00 [ 0.00 ]  0.0  ! -2097 $1&   0. #  0. %
E + O2* > O2*1S + E      : 0.00E+00 [ 0.00 ]  0.0  ! -2066 $0&   0. #  0. %
E + O2* > O2 + E         : 0.00E+00 [ 0.00 ]  0.0  ! -2067 $0&   0. #  0. %
E + O2* > O + O + E      : 0.00E+00 [ 0.00 ]  0.0  ! -2068 $0&   0. #  0. %
E + O2* > O* + O + E     : 0.00E+00 [ 0.00 ]  0.0  ! -2069 $0&   0  #  0. %
E + O2* > O2^ + E + E    : 0.00E+00 [ 0.00 ]  0.0  ! -2072 $0&   0. #  0. %
E + O2* > O^ + O + E + E : 0.00E+00 [ 0.00 ]  0.0  ! -2074 $0&   0. #  0. %
!
E + O2*1S > O2*1S + E    : 0.00E+00 [ 0.00 ]  0.0  ! -2075 $0&   0. #  0. %
E + O2*1S > O- + O       : 0.00E+00 [ 0.00 ]  0.0  ! -2076 $0&   0. #  0. %
E + O2*1S > O2V + E      : 0.00E+00 [ 0.00 ]  0.0  ! -2098 $1&   0. #  0. %
E + O2*1S > O2* + E      : 0.00E+00 [ 0.00 ]  0.0  ! -2084 $0&   0. #  0. %
E + O2*1S > O2 + E       : 0.00E+00 [ 0.00 ]  0.0  ! -2085 $0&   0. #  0. %
E + O2*1S > O + O + E    : 0.00E+00 [ 0.00 ]  0.0  ! -2086 $0&   0. #  0. %
E + O2*1S > O* + O + E   : 0.00E+00 [ 0.00 ]  0.0  ! -2087 $0&   0  #  0. %
E + O2*1S > O2^ + E + E  : 0.00E+00 [ 0.00 ]  0.0  ! -2090 $0&   0. #  0. %
E + O2*1S > O^ + O + E + E : 0.0E+00 [ 0.0 ]  0.0  ! -2092 $0&   0. #  0. %
!
! Add reactions for major species in place of M
!
!E + O2 + M > O2- + M      : 3.60E-31 [ -0.5 ]  0.0  !    10 $0&   0. #  0. %
E + O2 + O2 > O2- + O2     : 3.60E-31 [ -0.5 ]  0.0  !    10 $0&   0. #  0. %
E + O2 + O2V > O2- + O2V   : 3.60E-31 [ -0.5 ]  0.0  !    10 $0&   0. #  0. %
E + O2 + O2* > O2- + O2*   : 3.60E-31 [ -0.5 ]  0.0  !    10 $0&   0. #  0. %
E + O2 + O3 > O2- + O3     : 3.60E-31 [ -0.5 ]  0.0  !    10 $0&   0. #  0. %
E + O2 + O > O2- + O       : 3.60E-31 [ -0.5 ]  0.0  !    10 $0&   0. #  0. %
E + O2 + H2O > O2- + H2O   : 3.60E-31 [ -0.5 ]  0.0  !    10 $0&   0. #  0. %
E + O2 + OH  > O2- + OH    : 3.60E-31 [ -0.5 ]  0.0  !    10 $0&   0. #  0. %
E + O2 + H   > O2- + H     : 3.60E-31 [ -0.5 ]  0.0  !    10 $0&   0. #  0. %
!
E + O2V + O2 > O2- + O2    : 3.60E-31 [ -0.5 ]  0.0  !    10 $0&   0. #  0. %
E + O2V + O2V > O2- + O2V  : 3.60E-31 [ -0.5 ]  0.0  !    10 $0&   0. #  0. %
E + O2V + O2* > O2- + O2*  : 3.60E-31 [ -0.5 ]  0.0  !    10 $0&   0. #  0. %
E + O2V + O3 > O2- + O3    : 3.60E-31 [ -0.5 ]  0.0  !    10 $0&   0. #  0. %
E + O2V + O > O2- + O      : 3.60E-31 [ -0.5 ]  0.0  !    10 $0&   0. #  0. %
E + O2V + H2O > O2- + H2O  : 3.60E-31 [ -0.5 ]  0.0  !    10 $0&   0. #  0. %
E + O2V + OH  > O2- + OH   : 3.60E-31 [ -0.5 ]  0.0  !    10 $0&   0. #  0. %
E + O2V + H   > O2- + H    : 3.60E-31 [ -0.5 ]  0.0  !    10 $0&   0. #  0. %
!
E + O2^ > O + O          : 1.20E-08 [ -0.7 ]  0.0  !    10 $0& 999. #  0. % R9
E + O2^ > O* + O         : 8.88E-09 [ -0.7 ]  0.0  !    10 $0& 999. #  0. % R9
!
E + O3 > O3 + E          : 0.00E+00 [ 0.00 ]  0.0  ! -1977 $0&   0. #  0. %
E + O3 > O- + O2         : 0.00E+00 [ 0.00 ]  0.0  ! -1978 $0&   0. #  0. %
E + O3 > O2- + O         : 0.00E+00 [ 0.00 ]  0.0  ! -1979 $0&   0. #  0. %
!
E + O > O + E            : 0.00E+00 [ 0.00 ]  0.0  !  -934 $0&   0. #  0. %
E + O > O* + E           : 0.00E+00 [ 0.00 ]  0.0  !  -935 $0&   0. #  0. %
```

```
E + O > O1S + E          : 0.00E+00 [ 0.00 ]  0.0  !  -936 $0&   0. #  0. %
E + O > O^ + E + E       : 0.00E+00 [ 0.00 ]  0.0  !  -941 $0&   0. #  0. %
!
E + O* > O* + E          : 0.00E+00 [ 0.00 ]  0.0  !  -942 $0&   0. #  0. %
E + O* > O + E           : 0.00E+00 [ 0.00 ]  0.0  !  -943 $0&   0. #  0. %
E + O* > O^ + E + E      : 0.00E+00 [ 0.00 ]  0.0  !  -944 $0&   0. #  0. %
!
E + O1S > O + E          : 0.00E+00 [ 0.00 ]  0.0  !  -936 $1&   0. #  0. %
E + O1S > O^ + E + E     : 6.60e-09 [ 0.6  ]  9.43 !    10 $0&   0. # 9.43 % R8a
E + O- > O + E + E       : 1.95E-12 [ 0.5  ]  3.4  !    10 $0&   0. # 3.4 % R8
E + O^ > O*              : 5.30e-13 [ -0.5 ]  0.0  !    10 $0&   0. #  0. % R3
E + E + O^ > O* + E      : 5.12e-27 [ -4.5 ]  0.0  !    10 $0&   0. #  0. % R3
!
O- + O2^ > O + O2        : 2.00E-07 [ -1.0 ]  0.0  !    20 $0& 999. #  0. % R9
O- + O2^ > O + O + O2    : 1.00E-07 [ 0.00 ]  0.0  !    20 $0& 999. #  0. % R9
O- + O^ > O + O          : 2.00E-07 [ -1.0 ]  0.0  !    20 $0& 999. #  0. % R9
O2- + O2^ > O2 + O2      : 2.00E-07 [ -1.0 ]  0.0  !    20 $0& 999. #  0. % R9
O2- + O2^ > O2 + O + O   : 1.00E-07 [ 0.00 ]  0.0  !    20 $0& 999. #  0. % R9
O2- + O^ > O2 + O        : 2.00E-07 [ -1.0 ]  0.0  !    20 $0& 999. #  0. % R9
O3- + O2^ > O3 + O2      : 2.00E-07 [ -1.0 ]  0.0  !    20 $0& 999. #  0. % R9
O3- + O2^ > O3 + O + O   : 1.00E-07 [ 0.00 ]  0.0  !    20 $0& 999. #  0. % R9
O3- + O^ > O3 + O        : 2.00E-07 [ -1.0 ]  0.0  !    20 $0& 999. #  0. % R9
!
! Add reactions for major species in place of M
!
!O- + O2^ + M > O + O2 + M : 2.0E-25 [ -2.5 ]  0.0 !    20 $0& 999. #  0. % R9
!O- + O^ + M > O + O + M   : 2.0E-25 [ -2.5 ]  0.0 !    20 $0& 999. #  0. % R9
!O- + HE^ + M > O + HE + M : 2.0E-25 [ -2.5 ]  0.0 !    20 $0& 999. #  0. % R9
O- + O2^ + O2 > O + O2 + O2   : 2.E-25 [ -2.5 ]  0.0 !  20 $0& 999. #  0. % R9
O- + O^  + O2 > O + O + O2    : 2.E-25 [ -2.5 ]  0.0 !  20 $0& 999. #  0. % R9
O- + O2^ + O2V > O + O2 + O2V : 2.E-25 [ -2.5 ]  0.0 !   20 $0& 999. #  0. % R9
O- + O^  + O2V > O + O + O2V  : 2.E-25 [ -2.5 ]  0.0 !   20 $0& 999. #  0. % R9
O- + O2^ + O2* > O + O2 + O2* : 2.E-25 [ -2.5 ]  0.0 !   20 $0& 999. #  0. % R9
O- + O^  + O2* > O + O + O2*  : 2.E-25 [ -2.5 ]  0.0 !   20 $0& 999. #  0. % R9
O- + O2^ + O3 > O + O2 + O3   : 2.E-25 [ -2.5 ]  0.0 ! 20 $0& 999. #  0. % R9
O- + O^  + O3 > O + O + O3    : 2.E-25 [ -2.5 ]  0.0 ! 20 $0& 999. #  0. % R9
O- + O2^ + O > O + O2 + O     : 2.E-25 [ -2.5 ]  0.0 ! 20 $0& 999. #  0. % R9
O- + O^  + O > O + O + O      : 2.E-25 [ -2.5 ]  0.0 ! 20 $0& 999. #  0. % R9
!
O- + O > O2 + E          : 2.00e-10 [ 0.50 ]  0.0  !    20 $0&   0. #  0. % R4
O- + O2* > O3 + E        : 3.00e-10 [ 0.50 ]  0.0  !    20 $0&   0. #  0. % R4
O- + O2*1S > O + O2 + E  : 6.90e-10 [ 0.50 ]  0.0  !    20 $0&   0. #  0. % R9
O- + O2 > O3 + E         : 5.00e-15 [ 0.50 ]  0.0  !    20 $0&   0. #  0. % R9
O- + O2V > O3 + E        : 5.00e-15 [ 0.50 ]  0.0  !    20 $0&   0. #  0. % EST
O- + O3 > O2 + O2 + E    : 3.01e-10 [ 0.50 ]  0.0  !    20 $0&   0. #  0. % R4
O- + O3 > O3- + O        : 1.99e-10 [ 0.50 ]  0.0  !    20 $0&   0. #  0. % R4
O- + O3 > O2- + O2       : 1.02e-11 [ 0.50 ]  0.0  !    20 $0&   0. #  0. % R4
O2- + O > O- + O2        : 1.50E-10 [ 0.50 ]  0.0  !    20 $0& 999. #  0. % R4
O2- + O > O3 + E         : 1.50E-10 [ 0.50 ]  0.0  !    20 $0& 999. #  0. % R4
O2- + O2* > E + O2 + O2  : 2.00E-10 [ 0.50 ]  0.0  !    20 $0&   0. #  0. % R4
O2- + O3 > O3- + O2      : 6.00E-10 [ 0.50 ]  0.0  !    20 $0&   0. #  0. % R4
O3- + O > O2- + O2       : 2.50E-10 [ 0.50 ]  0.0  !    20 $0&   0. #  0. % R4
O + O^ > O + O^          : 1.00E-09 [ 0.50 ]  0.0  !    20 $0&   0. #  0. %
!
! Add reactions for major species in place of M
!
!O + O^ + M > O2^ + M    : 1.00E-29 [ 0.50 ]  0.0  !    20 $0&   0.  #  0. % R9
O + O^ + O2 > O2^ + O2   : 1.00E-29 [ 0.50 ]  0.0  !    20 $0& 999.  #  0. % R9
O + O^ + O2V > O2^ + O2V : 1.00E-29 [ 0.50 ]  0.0  !    20 $0& 999.  #  0. % R9
O + O^ + O2* > O2^ + O2* : 1.00E-29 [ 0.50 ]  0.0  !    20 $0& 999.  #  0. % R9
```

```
O + O^ + O3 > O2^ + O3    : 1.00E-29 [ 0.50 ]  0.0  !    20 $0& 999.  #  0. % R9
O + O^ + O > O2^ + O      : 1.00E-29 [ 0.50 ]  0.0  !    20 $0& 999.  #  0. % R9
O + O^ + H2O > O2^ + H2O : 1.00E-29 [ 0.50 ]  0.0  !    20 $0& 999.  #  0. % R9
O + O^ + OH  > O2^ + OH   : 1.00E-29 [ 0.50 ]  0.0  !    20 $0& 999.  #  0. % R9
O + O^ + H   > O2^ + H    : 1.00E-29 [ 0.50 ]  0.0  !    20 $0& 999.  #  0. % R9
!
O2 + O2^ > O2 + O2^       : 1.00E-09 [ 0.50 ]  0.0  !    20 $0&   0. #  0. %
O^ + O2 > O2^ + O         : 2.00E-11 [-0.40 ]  0.0  !    20 $0&   0. #  0. % R4
O^ + O3 > O2^ + O2        : 1.00E-10 [ 0.00 ]  0.0  !    20 $0&   0. #  0. % R9
O* + O > O + O            : 8.00E-12 [ 0.00 ]  0.0  !    20 $0& 999. #  0. % R9
O* + O2 > O + O2*1S       : 2.56E-11 [ 0.00 ] -67.0 !    20 $0& 999. #  0. % R1
O* + O2 > O + O2*         : 0.16E-11 [ 0.00 ] -67.0 !    20 $0& 999. #  0. % R1
O* + O2 > O + O2          : 0.48E-11 [ 0.00 ] -67.0 !    20 $0& 999. #  0. % R1
O* + O3 > O2 + O + O      : 1.20E-10 [ 0.00 ]  0.0  !    20 $0& 999. #  0. % R6
O* + O3 > O2 + O2         : 1.20E-10 [ 0.00 ]  0.0  !    20 $0& 999. #  0. % R7
O1S + O2 > O* + O2        : 3.20E-12 [ 0.00 ]  850. !    20 $0& 999. #  0. % R7
O1S + O2 > O + O2         : 1.60E-12 [ 0.00 ]  850. !    20 $0& 999. #  0. % R7
O1S + O2V > O* + O2V      : 3.20E-12 [ 0.00 ]  850. !    20 $0& 999. #  0. % EST
O1S + O2V > O + O2V       : 1.60E-12 [ 0.00 ]  850. !    20 $0& 999. #  0. % EST
O1S + O2* > O + O2        : 1.10E-10 [ 0.00 ]  0.0  !    20 $0& 999. #  0. % R9a
O1S + O2* > O* + O2*1S    : 2.90E-11 [ 0.00 ]  0.0  !    20 $0& 999. #  0. % R9
O1S + O2* > O + O + O     : 3.20E-11 [ 0.00 ]  0.0  !    20 $0& 999. #  0. % R9
O1S + O > O* + O          : 1.67E-11 [ 0.00 ]  300. !    20 $0& 999. #  0. % R7
O1S + O > O + O           : 3.33E-11 [ 0.00 ]  300. !    20 $0& 999. #  0. % R7
O1S + O3 > O2 + O2        : 5.80E-10 [ 0.00 ]  0.0  !    20 $0& 999. #  0. % R7a
O2* + O > O2 + O          : 2.00E-16 [ 0.00 ]  0.0  !    20 $0& 999. #  0. % R7
O2* + O2 > O2 + O2        : 3.00E-18 [ 0.00 ]  200. !    20 $0& 999. #  0. % R1
O2* + O2V > O2 + O2V      : 3.00E-18 [ 0.00 ]  200. !    20 $0& 999. #  0. % EST
O2* + O2* > O2 + O2       : 0.90E-16 [ 0.00 ]  560. !    20 $0& 999. #  0. % R7b
O2* + O2* > O2*1S + O2    : 0.90E-16 [ 0.00 ]  560. !    20 $0& 999. #  0. % R7b
O2* + O2* + O2 > O3 + O3 : 0.00E-31 [ 0.00 ]  560. !    20 $0& 999. #  0. % R9,10
O2* + O2 > O + O3         : 2.95E-21 [ 0.50 ]  0.0  !    20 $0& 999. #  0. %
O2* + O2V > O + O3        : 2.95E-21 [ 0.50 ]  0.0  !    20 $0& 999. #  0. % EST
O2* + O3 > O2 + O2 + O    : 5.20E-11 [ 0.00 ] 2840. !    20 $0& 999. #  0. %
O2*1S + O2*1S > O2* + O2 : 3.60E-17 [ 0.50 ]  0.0  !    20 $0& 999. #  0. % est
O2*1S + O2 > O2* + O2     : 3.60E-17 [ 0.50 ]  0.0  !    20 $0& 999. #  0. % R1
O2*1S + O2 > O2 + O2      : 0.40E-17 [ 0.50 ]  0.0  !    20 $0& 999. #  0. % R1
O2*1S + O2V > O2* + O2V   : 3.60E-17 [ 0.50 ]  0.0  !    20 $0& 999. #  0. % EST
O2*1S + O2V > O2 + O2V    : 0.40E-17 [ 0.50 ]  0.0  !    20 $0& 999. #  0. % EST
O2*1S + O > O2* + O       : 7.20E-14 [ 0.50 ]  0.0  !    20 $0& 999. #  0. % R1
O2*1S + O > O2 + O        : 0.80E-14 [ 0.50 ]  0.0  !    20 $0& 999. #  0. % R1
O2*1S + O3 > O + O2 + O2 : 7.33E-12 [ 0.50 ]  0.0  !    20 $0& 999. #  0. % R5
O2*1S + O3 > O2* + O3     : 7.33E-12 [ 0.50 ]  0.0  !    20 $0& 999. #  0. % R5
O2*1S + O3 > O2 + O3      : 7.33E-12 [ 0.50 ]  0.0  !    20 $0& 999. #  0. % R5
O2V + O > O2 + O          : 1.00E-14 [ 0.50 ]  0.0  !    20 $0& 999. #  0. % R1est
O2V + O2 > O2 + O2        : 1.00E-14 [ 0.50 ]  0.0  !    20 $0& 999. #  0. % R1est
O2V + O2V > O2 + O2V      : 1.00E-14 [ 0.50 ]  0.0  !    20 $0& 999. #  0. % R1est
O2V + O2* > O2 + O2*      : 1.00E-14 [ 0.50 ]  0.0  !    20 $0& 999. #  0. % R1est
O2V + O3 > O2 + O3        : 1.00E-14 [ 0.50 ]  0.0  !    20 $0& 999. #  0. % R1est
O + O + O2 > O2 + O2      : 2.56E-34 [ -0.63 ] 0.0  !    20 $0& 999. #  0. % R9
O + O + O2V > O2 + O2V    : 2.56E-34 [ -0.63 ] 0.0  !    20 $0& 999. #  0. % EST
O + O + O > O2 + O        : 9.21E-34 [ -0.63 ] 0.0  !    20 $0& 999. #  0. % R9
O + O + H2O > O2 + H2O    : 1.18E-33 [  0.00 ] 0.0  !    20 $0& 999. #  0. % NIST,R
O + O + OH  > O2 + OH     : 1.18E-33 [  0.00 ] 0.0  !    20 $0& 999. #  0. % NIST,R
O + O + H   > O2 + H      : 1.18E-33 [  0.00 ] 0.0  !    20 $0& 999. #  0. % NIST,R
O + O + O2 > O2* + O2     : 1.93E-35 [ -0.63 ] 0.0  !    20 $0& 999. #  0. % R9
O + O + O2V > O2* + O2V   : 1.93E-35 [ -0.63 ] 0.0  !    20 $0& 999. #  0. % EST
O + O + O > O2* + O       : 6.93E-35 [ -0.63 ] 0.0  !    20 $0& 999. #  0. % R9
!
O + O + H2O > O2* + H2O   : 1.00E-34 [  0.00 ] 0.0  !    20 $0& 999. #  0. % NIST,R
```

```
O + O + OH  > O2* + OH   : 1.00E-34 [  0.00 ] 0.0  !    20 $0& 999. #  0. % NIST,R
O + O + H   > O2* + H    : 1.00E-34 [  0.00 ] 0.0  !    20 $0& 999. #  0. % NIST,R
O + O2 + O2 > O3 + O2    : 6.00E-34 [ -2.8 ]  0.0  !    20 $0& 999. #  0. % R1
O + O2 + O2V > O3 + O2V  : 6.00E-34 [ -2.8 ]  0.0  !    20 $0& 999. #  0. % EST
O + O2 + H2O > O3 + H2O  : 3.40E-34 [ -1.2 ]  0.0  !    20 $0& 999. #  0. % NIST
O + O2 + OH > O3 + OH    : 3.40E-34 [ -1.2 ]  0.0  !    20 $0& 999. #  0. % NIST
O + O2 + H > O3 + H      : 3.40E-34 [ -1.2 ]  0.0  !    20 $0& 999. #  0. % NIST
O + O2 + O > O3 + O      : 3.40E-34 [ -1.2 ]  0.0  !    20 $0& 999. #  0. % EST
O + O3 > O2 + O2         : 8.00E-12 [ 0.00 ] 2060. !    20 $0& 999. #  0. % R1
!
! Add reverse reactions to three-body reactions
!
O2 + O2 > O + O + O2     : 5.92E-08 [ -1.00 ] 29700. !  20 $0& 999. #  0. % NIST
O2 + O2V > O + O + O2    : 5.92E-08 [ -1.00 ] 29700. !  20 $0& 999. #  0. % EST
O2* + O2 > O + O + O2    : 1.18E-07 [ -1.00 ] 29700. !  20 $0& 999. #  0. % EST
O2* + O2V > O + O + O2V  : 1.18E-07 [ -1.00 ] 29700. !  20 $0& 999. #  0. % EST
O2 + O  > O + O + O      : 4.93E-07 [ -1.00 ] 29700. !  20 $0& 999. #  0. % NIST
O2* + O  > O + O + O     : 9.86E-07 [ -1.00 ] 29700. !  20 $0& 999. #  0. % EST
O2 + O2 > O3 + O         : 1.11E-11 [  0.00 ] 24950. !  20 $0& 999. #  0. % NIST
!
! Add reactions for major species in place of M
!
!O3 + M > O2 + O + M      : 1.56E-09 [ 0.00 ] 11490. !   20 $0& 999. #  0. %
O3 + O2 > O2 + O + O2     : 1.56E-09 [ 0.00 ] 11490. !   20 $0& 999. #  0. %
O3 + O2V > O2 + O + O2V   : 1.56E-09 [ 0.00 ] 11490. !   20 $0& 999. #  0. %
O3 + O2* > O2 + O + O2*   : 1.56E-09 [ 0.00 ] 11490. !   20 $0& 999. #  0. %
O3 + O3 > O2 + O + O3     : 1.56E-09 [ 0.00 ] 11490. !   20 $0& 999. #  0. %
O3 + O > O2 + O + O       : 1.56E-09 [ 0.00 ] 11490. !   20 $0& 999. #  0. %
!
!E + O3 > E + O2 + O*    : 0.00E-00 [ 0.00 ]  0.0  !     1 $0& 999. #  0. %
!
!*** START - ADDED BY NGUYEN - SEPT 29, 2008 - START ***
! MOMENTUM TRANSFER
E + H2O > E + H2O            :  0.00E+00  [  0.00 ] 0.000E+00 ! -1040 $0& 0. #  0.
! VIBRATION (1-3)
E + H2O > E + H2O            :  0.00E+00  [  0.00 ] 0.000E+00 ! -1041 $0& 0. #  0.
E + H2O > E + H2O            :  0.00E+00  [  0.00 ] 0.000E+00 ! -1042 $0& 0. #  0.
E + H2O > E + H2O            :  0.00E+00  [  0.00 ] 0.000E+00 ! -1043 $0& 0. #  0.
! DISSOCIATIVE ATTACHMENT (1-3)
E + H2O > H- + OH            :  0.00E+00  [  0.00 ] 0.000E+00 ! -1044 $0& 23 #  0.
E + H2O > O- + H + H         :  0.00E+00  [  0.00 ] 0.000E+00 ! -2314 $0& 23 #  0.
E + H2O > OH- + H            :  0.00E+00  [  0.00 ] 0.000E+00 ! -2315 $0& 23 #  0.
! DISSOCIATION (1-2)
E + H2O > OH + H + E         :  0.00E+00  [  0.00 ] 0.000E+00 ! -1045 $0& 21 #  0.
E + H2O > O + H + H + E       :  0.00E+00  [  0.00 ] 0.000E+00 ! -1046 $0& 21 #  0
%
! IONIZATION (1-5)
E + H2O > H2O^ + E + E       :  0.00E+00  [  0.00 ] 0.000E+00 ! -1047 $0& 19 #  0.
E + H2O > OH^ + H + E + E    :  0.00E+00  [  0.00 ] 0.000E+00 ! -2316 $0& 23 #  0.
E + H2O > O^ + H + H + E + E :  0.00E+00  [  0.00 ] 0.000E+00 ! -2317 $0& 23 #  0.
E + H2O > H2^ + O + E + E    :  0.00E+00  [  0.00 ] 0.000E+00 ! -2318 $0& 23 #  0.
E + H2O > H^ + OH + E + E    :  0.00E+00  [  0.00 ] 0.000E+00 ! -2319 $0& 23 #  0.
!*** END - NGUYEN - SEPT 29, 2008 - END ***
!
E + H2 > H + H + E           :  0.00E+00  [  0.00 ] 0.000E+00 !   -17 $0&  19 #  0.
E + H2 > H2^ + E + E         :  0.00E+00  [  0.00 ] 0.000E+00 !   -18 $0&  19 #  0.
E + H2^ > H + H              :  2.00E-07  [ -0.50 ] 0.000E+00 !    10 $0& 232 #  0.
H + OH + M > H2O + M         :  4.30E-31  [  0.00 ] 0.000E+00 !     4 $0&  30 #  0.
H + O2 + M > HO2 + M         :  6.14E-32  [ -1.60 ] 0.000E+00 !   684 $0&  51 #  0.
H + H + M > H2 + M           :  4.80E-33  [  0.00 ] 0.000E+00 !     4 $0&  52 #  0.
```

```
H + HO2 > OH + OH             :  2.80E-10  [  0.00 ] 4.400E+02 !  211 $0&  55 #  0.
H + O3 > OH + O2              :  1.40E-10  [  0.00 ] 4.800E+02 !  169 $0&  57 #  0.
O* + H2O > O + H2O            :  1.20E-11  [  0.00 ] 0.000E+00 !    1 $0&  78 #  0.
O + O2 + H2O > O3 + H2O       :  0.00E+00  [  0.00 ] 0.000E+00 !    4 $0&  79 #  0.
O* + H2O > OH + OH            :  2.20E-10  [  0.00 ] 0.000E+00 !    1 $0&  80 #  0.
O + HO2 > OH + O2             :  2.90E-11  [  0.00 ] 2.000E+02 !  174 $0&  81 #  0.
OH + OH > O + H2O             :  1.03E-12  [  1.40 ]-2.000E+02 !  207 $0&  89 #  0.
OH + HO2 > H2O + O2           :  8.00E-11  [  0.00 ] 0.000E+00 !    1 $0&  96 #  0.
H2O^ + H2O > H3O^ + OH        :  1.70E-09  [  0.00 ] 0.000E+00 !    1 $0&  97 #  0.
H2O^ + O2 > O2^ + H2O         :  4.30E-10  [  0.00 ] 0.000E+00 !    1 $0&  99 #  0.
OH + O3 > HO2 + O2            :  1.90E-12  [  0.00 ] 1.000E+03 !  162 $0& 100 #  0.
HO2 + O3 > OH + O2 + O2       :  1.40E-14  [  0.00 ] 6.000E+02 !  160 $0& 106 #  0.
O + OH > H + O2               :  2.30E-11  [  0.00 ]-1.100E+02 !  167 $0& 116 #  0.
OH + OH + O2 > H2O2 + O2      :  6.90E-31  [ -0.80 ] 0.000E+00 !  164 $0& 118 #  0.
OH + H2O2 > H2O + HO2         :  2.90E-12  [  0.00 ] 1.600E+02 !  163 $0& 120 #  0.
H + HO2 > H2 + O2             :  1.10E-10  [  0.00 ] 1.070E+03 !  210 $0& 122 #  0.
O2^^*H2O + H2O > H3O^ + OH + O2 : 1.2E-09   [  0.00 ] 0.000E+00 !    1 $0& 128 #  0.
H3O^ + H2O + M > H3O^^*H2O + M  : 5.0E-27   [  0.00 ] 0.000E+00 !    4 $0& 129 #  0.
H3O^^*H2O + H2O > XWAT        :  1.00E-09  [  0.00 ] 0.000E+00 !    1 $0& 131 #  0.
XWAT + E > H + X1WAT          :  2.00E-07  [ -0.50 ] 0.000E+00 !   10 $0& 133 #  0.
O2^ + H2O + M > O2^^*H2O + M  :  2.50E-28  [  0.00 ] 0.000E+00 !    4 $0& 201 #  0.
OH + H2 > H2O + H             :  7.70E-12  [  0.00 ] 2.100E+03 !  165 $0& 208 #  0.
O* + H2O > H2 + O2            :  2.30E-12  [  0.00 ] 0.000E+00 !    1 $0& 209 #  0.
O* + H2 > OH + H              :  1.10E-10  [  0.00 ] 0.000E+00 !    1 $0& 210 #  0.
O + H2O2 > OH + HO2           :  1.40E-12  [  0.00 ] 2.000E+03 !  166 $0& 211 #  0.
O + H2 > OH + H               :  1.60E-11  [  0.00 ] 4.570E+03 !  168 $0& 212 #  0.
H + HO2 > H2O + O             :  9.40E-13  [  0.00 ] 0.000E+00 !    1 $0& 213 #  0.
HO2 + HO2 + M > H2O2 + O2 + M : 1.90E-33  [  0.00 ]-9.800E+02 !  176 $0& 215 #  0.
H2O^ + E > OH + H             :  6.60E-06  [ -0.50 ] 0.000E+00 !   10 $0& 221 #  0.
H2O^ + E > O + H + H          :  2.88E-06  [ -0.50 ] 0.000E+00 !   10 $0& 222 #  0.
H2O^ + E > O + H2             :  2.52E-06  [ -0.50 ] 0.000E+00 !   10 $0& 223 #  0.
H2O^ + O2- > H2O + O2         :  2.00E-06  [  0.00 ] 0.000E+00 !    6 $0& 227 #  0.
H3O^ + E > H2O + H            :  2.00E-07  [ -0.50 ] 0.000E+00 !   10 $0& 228 #  0.
H3O^ + O2- > H2O + H + O2     :  2.00E-06  [  0.00 ] 0.000E+00 !    6 $0& 231 #  0.
O2^^*H2O + O2- > O2 + O2 + H2O : 2.00E-06  [  0.00 ] 0.000E+00 !    6 $0& 246 #  0.
O2^^*H2O + E > O2 + H2O       :  2.00E-07  [ -0.50 ] 0.000E+00 !   10 $0& 248 #  0.
H3O^^*H2O + E> H + H2O + H2O  :  2.00E-07  [ -0.50 ] 0.000E+00 !   10 $0& 250 #  0.
H3O^^*H2O + O2- > H + H2O + H2O +O2 : 2.0E-06  [ 0.0 ] 0.0E+00 !    6 $0& 253 #  0.
XWAT + O2- > H + X1WAT + O2   :  2.00E-06  [  0.00 ] 0.000E+00 !    6 $0& 254 #  0.
O + H + M > OH + M            :  1.62E-32  [  0.00 ] 0.000E+00 !    4 $0& 280 #  0.
H + H2O2 > H2O + OH           :  4.00E-11  [  0.00 ] 2.000E+03 !  214 $0& 281 #  0.
H + H2O2 > HO2 + H2           :  8.00E-11  [  0.00 ] 4.000E+03 !  213 $0& 293 #  0.
H2 + O2 > H + HO2             :  2.40E-10  [  0.00 ] 2.850E+04 !  202 $0& 295 #  0.
H + O2 > OH + O               :  1.65E-09  [ -0.90 ] 8.750E+03 !  203 $0& 296 #  0.
OH + M > O + H + M            :  4.00E-09  [  0.00 ] 5.000E+04 !  204 $0& 297 #  0.
OH + O2 > O + HO2             :  3.70E-11  [  0.00 ] 2.650E+04 !  205 $0& 298 #  0.
OH + H > O + H2               :  5.21E-11  [  0.67 ] 5.180E+02 !  206 $0& 299 #  0.
HO2 + M > H + O2 + M          :  2.39E-08  [ -1.18 ] 2.436E+04 !  208 $0& 300 #  0.
HO2 + H2 > H2O2 + H           :  5.00E-11  [  0.00 ] 1.310E+04 !  209 $0& 301 #  0.
H2O2 + O2 > HO2 + HO2         :  9.00E-11  [  0.00 ] 2.000E+04 !  212 $0& 302 #  0.
H2O + H > H2 + OH             :  5.24E-12  [  1.90 ] 9.265E+03 !  215 $0& 303 #  0.
H2O + O > OH + OH             :  1.26E-11  [  1.30 ] 8.605E+03 !  216 $0& 304 #  0.
O- + H2^ > O + H2             :  3.00E-06  [  0.00 ] 0.000E+00 !    6 $0& 331 #  0.
O2- + H2^ > O2 + H2           :  3.00E-06  [  0.00 ] 0.000E+00 !    6 $0& 331 #  0.
H- + H2^ > H + H2             :  3.00E-06  [  0.00 ] 0.000E+00 !    6 $0& 331 #  0.
H- + H2O^ > H + H2O           :  3.00E-06  [  0.00 ] 0.000E+00 !    6 $0& 332 #  0.
O- + H2O^ > O + H2O           :  3.00E-06  [  0.00 ] 0.000E+00 !    6 $0& 333 #  0.
H- + H3O^ > H2 + H2O          :  3.00E-06  [  0.00 ] 0.000E+00 !    6 $0& 334 #  0.
O- + H3O^ > OH + H2O          :  3.00E-06  [  0.00 ] 0.000E+00 !    6 $0& 335 #  0.
H- + O2^ + M > HO2 + M        :  1.20E-25  [  0.00 ] 0.000E+00 !    4 $0& 336 #  0.
O- + O2^ > O + O2             :  3.00E-06  [  0.00 ] 0.000E+00 !    6 $0& 337 #  0.
H- + O^ + M > OH + M          :  1.20E-25  [  0.00 ] 0.000E+00 !    4 $0& 344 #  0.
O- + O^ + M > O2 + M          :  1.20E-25  [  0.00 ] 0.000E+00 !    4 $0& 345 #  0.
H- + O2^^*H2O > HO2 + H2O     :  3.00E-06  [  0.00 ] 0.000E+00 !    6 $0& 352 #  0.
O- + O2^^*H2O > O + O2 + H2O  :  3.00E-06  [  0.00 ] 0.000E+00 !    6 $0& 353 #  0.
H- + H3O^^*H2O > H2 + H2O + H2O :  3.00E-06  [  0.00 ] 0.0E+00 !    6 $0& 354 #  0.
O- + H3O^^*H2O > OH + H2O + H2O :  3.00E-06  [  0.00 ] 0.0E+00 !    6 $0& 355 #  0.
H- + XWAT > H2 + X1WAT        :  3.00E-06  [  0.00 ] 0.000E+00 !    6 $0& 358 #  0.
O- + XWAT > OH + X1WAT        :  3.00E-06  [  0.00 ] 0.000E+00 !    6 $0& 359 #  0.
X1WAT > H2O + H2O + H2O       :  1.00E+07  [  0.00 ] 0.000E+00 !    2 $0& 379 #  0.
O + OH + M > HO2 + M          :  2.76E-31  [  0.00 ] 0.000E+00 !  647 $0& 749 #  0.
```

Bibliography

[1] IPCC, *Climate Change 2007: The Physical Science Basis. Contribution of Working Group I to the Fourth Assessment Report of the Intergovernmental Panel on Climate Change*. Cambridge University Press, 2007. IPCC-2007: WG1-AR4.

[2] Energy Information Administration, “International energy outlook 2007,” Tech. Rep. DOE/EIA-0484(2007), Energy Information Administration, Office of Integrated Analysis and Forecasting, U.S. Department of Energy, 2007.

[3] US Bureau of the Census, “Total midyear population of the world: 1950-2050,” tech. rep., US Bureau of the Census, 2003.

[4] U. S. Department of Energy, “Hydrogen production.” `http://www1.eere.energy.gov/hydrogenandfuelcells/production/natural_gas.html`, July 2009.

[5] J. H. Chaffin, S. M. Bobbio, H. I. Inyang, and L. Kaanagbara, “Hydrogen production by plasma electrolysis,” *Journal of Energy Engineering*, pp. 104–108, 2006.

[6] Z. C. Yan, C. Li, and W. H. Lin, “Hydrogen generation by glow discharge plasma electrolysis of methanol solution,” *International Journal of Hydrogen Energy*, vol. 34, 2008.

[7] H. Kabashima, H. Einaga, and S. Futamura, “Hydrogen generation from water, methane, and methanol with nonthermal plasma,” *IEEE Transactions on Industry Applications*, vol. 39, no. 2, 2003.

[8] J. Scherzer and A. J. Gruia, *Hydrocracking Science and Technology*. Marcel Dekker, Inc., 1996.

[9] E. Worrell, D. Phylipsen, D. Einstein, and N. Martin, “Energy use and energy intensity of the u.s. chemical industry,” Tech. Rep. LBNL-44314, Energy Analysis Department, Environmental Energy Technologies Division, Lawrence Berkeley National Laboratory, 2000.

[10] E. S. Jang, M. Y. Jung, and D. B. Min, “Hydrogenation of low trans and high conjugated fatty acids,” *Comprehensive Revies in Food Science and Food Safety*, vol. 1, pp. 22–30, 2005.

[11] J. S. Clements, M. Sato, and R. H. Davis, “Preliminary investigation of prebreakdown phenomena and chemical reactions using a pulsed high-voltage discharge in water,” *IEEE Transactions on Industry Applications*, vol. IA-23, no. 2, pp. 224 – 35, 1987.

[12] A. T. Sugiarto and M. Sato, "Pulsed plasma processing of organic compounds in aqueous solution," *Thin Solid Films*, vol. 386, no. 2, pp. 295–299, 2001.

[13] T. Maehara, H. Toyota, M. Kuramoto, A. Iwamae, A. Tadokoro, S. Mukasa, H. Yamashita, A. Kawashima, and S. Nomura, "Radio frequency plasma in water," *Japanese Journal of Applied Physics*, vol. 45, no. 11, pp. 8864–8868, 2006.

[14] A. A. Ivannikov, V. M. Lelevkin, A. V. Tokarev, and V. A. Yudanov, "Atmospheric-presure glow discharge treatment of water," *High Energy Chemistry*, vol. 37, no. 2, pp. 115–118, 2003.

[15] A. V. Samokhin, N. V. Alekseev, T. F. Korovkina, E. V. Troitskaya, and Y. V. Tsvetkov, "Oxidizing purification of water using thermal plasma," *Theoretical Foundations of Chemical Engineering*, vol. 41, no. 5, pp. 613–619, 2007.

[16] R. A. Rudder, G. C. Hudson, J. B. Posthill, R. E. Thomas, R. C. Hendry, and D. P. Malta, "Chemical vapor deposition of diamond films from water vapor rf-plasma discharges," *Appl. Phys. Lett.*, vol. 60, no. 3, pp. 329–331, 1992.

[17] R. K. Singh, D. Gilbert, R. Tellshow, P. H. Holloway, R. Ochoa, J. H. Simmons, and R. Koba, "Low-pressure, low-temperature, and remote-plasma deposition of diamond thin films from water-methanol mixtures," *Appl. Phys. Lett.*, vol. 61, no. 24, pp. 2863–2865, 1992.

[18] B. Sun, M. Sato, and J. S. Clements, "Oxidative processes occurring when pulsed high voltage discharges degrade phenol in aqueous solution," *Environmental Science and Technology*, vol. 34, no. 3, pp. 509 – 513, 2000.

[19] B. Sun, M. Sato, and J. S. Clements, "Use of a pulsed high-voltage discharge for removal of organic compounds in aqueous solution," *Journal of Physics D: Applied Physics*, vol. 32, no. 15, pp. 1908 – 1915, 1999.

[20] J. S. Oh, K. Kawamura, B. K. Pramanik, and A. Hatta, "Investigation of water-vapor plasma excited by microwaves as ultraviolet light source," *IEEE Transactions on Plamsa Science*, vol. 37, no. 1, pp. 107–112, 2009.

[21] G. Fridman, G. Friedman, A. Gutsol, A. Shekhter, V. N. Vasilets, and A. Fridman, "Applied plasma medicine," *Plasma Processes and Polymers*, vol. 5, pp. 503–533, 2008.

[22] M. M. Balkey, *Optimization of a Helicon Plasma Source for Maximum Density with Minimal Ion Heating*. PhD thesis, West Virginia University, 1999.

[23] R. W. Boswell and D. Vender, "An experimental study of breakdown in a pulsed helicon plasma," *Plasma Sources Science and Technology*, vol. 25, pp. 534–540, 1995.

[24] O. Sutherland, C. Charles, N. Plihon, and R. Boswell, "Experimental evidence of a double layer in a large volume helicon reactor," *Physical Review Letters*, vol. 95, 2005.

[25] K. M. Lemmer, *Use of a Helicon Source for Development of a Re-Entry Blackout Amelioration System*. PhD thesis, University of Michigan, 2009.

[26] British Petroleum, "Quantifying energy - bp statistical review of world energy june 2006," tech. rep., British Petroleum, 2006.

[27] University Corporation for Atmospheric Research, "Windows to the universe - earth statistics." `http://www.windows.ucar.edu/tour/link=/earth/statistics.html`, July 2009.

[28] NASA Jet Propulsion Laboratory, "Solar system - venus." `http://www.jpl.nasa.gov/solar_system/planets/mars_index.html`, July 2009.

[29] NASA Jet Propulsion Laboratory, "Solar system - venus." `http://www.jpl.nasa.gov/solar_system/planets/venus_index.html`, July 2009.

[30] J. T. Kiehl and K. E. Trenberth, "Earth's annual global mean energy budget," *Bulletin of the American Meteorological Society*, vol. 78, no. 2, pp. 197 – 208, 1997.

[31] T. Dowling and A. P. Showman, "Earth as a planet: Atmosphere and oceans," in *Encyclopedia of the solar system* (L.-A. McFadden, P. R. Weissman, and T. V. Johnson, eds.), pp. 169–187, Academic Press, second ed., 2007.

[32] G. Marland, T. A. Boden, and R. J. Andres, "Global, regional, and national co2 emissions. in trends: A compendium of data on global change," tech. rep., Carbon Dioxide Information Analysis Center, Oak Ridge National Laboratory, U.S. Department of Energy, Oak Ridge, Tenn., U.S.A., 2008.

[33] S. R. Turns, *An Introduction to Combustion*. McGraw Hill, second ed., 2000.

[34] L. D. S. Yadav, *Organic Spectroscopy*. Springer, 2005.

[35] Energy Information Adminsitration, "Annual energy review 2007," Tech. Rep. DOE/EIA-0384(2007), Energy Information Administration, Office Energy Statistics from the US Government, June 2008.

[36] Energy Information Administration, "Emissions of greenhouse gases report," Tech. Rep. DOE/EIA-0573(2006), Energy Information Administration, Office Energy Statistics from the US Government, 2007.

[37] Energy Information Administration, "Renewable energy consumption and electricity preliminary 2007 statistics," tech. rep., International Information Adminstration, Office of Coal, Nuclear, Electric and Alternate Fuels, U.S. Department of Energy, 2008.

[38] D. Dorling, M. Newman, and A. Barford, *The Atlas of the Real World*. Thames and Hudson, 2008.

[39] Energy Information Administration, "Annual energy review 2008," Tech. Rep. DOE/EIA-0384(2008), Energy Information Administration, Office of Integrated Analysis and Forecasting, U.S. Department of Energy, 2009.

[40] "Worldwide look at reserves and production," *Oil and Gas Journal*, vol. 103, no. 47, pp. 24–25, 2005.

[41] J. Deutch, J. R. Schlesinger, D. G. Victor, G. T. Allison, N. R. Augustine, R. A. Belfer, S. W. Bosworth, H. L. Croft, C. J. DiBona, and J. P. Einhorn, "National security consequences of u.s. oil dependency," tech. rep., Council on Foreign Relations, 2006.

[42] Energy Information Adminstration, "The impact of increased use of hydrogen on petroleum consumption and carbon dioxide emissions," Tech. Rep. SR/OIAF-CNEAF/2008-04, Energy Information Administration, Office Energy Statistics from the US Government, August 2008.

[43] B. Ewan and R. Allen, "A figure of merit assessment of the routes to hydrogen," *International Journal of Hydrogen Energy*, vol. 30, pp. 809–819, 2005.

[44] J. Ivy, "Summary of electrolytic hydrogen production," Tech. Rep. NREL/MP-560-36734, National Renewable Energy Laboratory, September 2004.

[45] J. Holladay, J. Hu, D. King, and Y. Wang, "An overview of hydrogen production," *Catalysis Today*, vol. 139, pp. 244–260, 2009.

[46] K. Pant and R. B. Gupta, "Fundamentals and use of hydrogen as a fuel," in *Hydrogen Fuel: Production, Transport, and Storage* (R. B. Gupta, ed.), pp. 4–29, CRC Press, 2009.

[47] N. Muradov, "Production of hydrogen from hydrocarbons," in *Hydrogen Fuel: Production, Transport, and Storage* (R. B. Gupta, ed.), pp. 34–86, CRC Press, 2009.

[48] K. McHugh, S. Eisele, and J. Nestell, "Hydrogen production methods," Tech. Rep. MPR-WP-0001, MPR Associates, Inc., 2005.

[49] K. Cox and J. Wiliamson, *Hydrogen: its technology and implications*. CRC Press, 1977.

[50] F. Barbir, "Pem electrolysis for production of hydrogen from renewable energy sources," *Solar Energy*, vol. 78, pp. 661–669, 2005.

[51] A. D. Little, "Guidance for transportation technologies," Tech. Rep. 35340-00, Arthur D. Little, Inc., February 2002.

[52] M. A. Lieberman and A. J. Lichtenberg, *Principles of Plasma Discharges and Materials Processing*. John Wiley and Sons, Inc., 2005.

[53] A. Fridman, *Plasma Chemistry*. Cambridge University Press, 2008.

[54] A. Fridman and L. A. Kennedy, *Plasma Physics and Engineering*. Taylor and Francis Books, Inc., 2004.

[55] P. Atkins and J. de Paula, *Elements of Physical Chemistry*. W. H. Freeman, fifth ed., 2009.

[56] M. Silberberg, *Chemistry: The Molecular Nature of Matter and Change*. McGraw Hill, second ed., 2000.

[57] A. Engel, *Ionized Gases*. Oxford University Press, 1955.

[58] T. D. Mark and G. H. Dunn, *Electron Impact Ionization*. Springer-Verlag, 1985.

[59] Y. P. Raizer, *Gas Discharge Physics*. Springer-Verlag, 1991.

[60] R. Goldston and P. Rutherford, *Introduction to plasma physics*. CRC Press, 1995.

[61] Y. Itikawa, *Molecular Processes in Plasmas*. Springer, 2007.

[62] R. W. Boswell, *A Study of Waves in Gaseous Plasmas*. PhD thesis, Flinders University of South Australia, 1974.

[63] R. W. Boswell, "Plasma production using a standing helicon wave," *Physics Letters A*, vol. 33A, no. 7, pp. 457–8, 1970.

[64] R. W. Boswell, "Plasma ionization by helicon waves," *Plasma Physics and Controlled Fusion*, vol. 33, no. 4, pp. 339–364, 1991.

[65] R. W. Boswell and F. F. Chen, "Helicons - the early years," *IEEE Transactions on Plasma Science*, vol. 25, 1997.

[66] F. F. Chen and R. W. Boswell, "Helicons - the past decade," *IEEE Transactions on Plasma Science*, vol. 25, 1997.

[67] D. D. Blackwell, T. G. Madziwa, D. Arnush, and F. F. Chen, "Evidence for trivelpiece-gould modes in a helicon discharge," *Physical Review Letters*, vol. 88, 2002.

[68] F. F. Chen, "Experiments on helicon plasma sources," *Journal of Vacuum Science and Technology A*, vol. 10, pp. 1389–1401, 1992.

[69] A. W. Degeling, C. O. Jung, R. W. Boswell, and A. R. Ellingboe, "Plasma production from helicon waves," *Physics of Plasmas*, vol. 3, pp. 2788–2796, 1996.

[70] L. Porte, S. M. Yun, D. Arnush, and F. F. Chen, "Superiority of half-wavelength helicon antenna," *Plasma Sources Science and Technology*, vol. 12, pp. 287–293, 2003.

[71] M. Kong, M. Laroussi, and A. Fridman, "Plasma medicine - opportunities and challenges for science and healthcare." Conference presentation at 36th International Conference on Plasma Science in San Diego, CA, June 2009.

[72] L. Bromberg, D. Cohn, A. Rabinovich, and N. Alexeev, "Plasma catalytic reforming of methane," *International Journal of Hydrogen Energy*, vol. 24, pp. 1131–1137, 1999.

[73] G. Petitpas, J. D. Rollier, A. Darmon, J. Gonzalez-Aguilar, R. Metkemeijer, and L. Fulcheri, “A comparative study of non-thermal plasma assisted reforming technologies,” *International Journal of Hydrogen Energy*, 2007.

[74] V. K. Givotov, A. A. Fridman, M. F. Krotov, E. G. Krasheninnikov, and B. I. Patrushev, “Plasmochemical methods of hydrogen production,” *Int. J. Hydrogen Energy*, vol. 6, no. 5, pp. 441–449, 1981.

[75] R. I. Asisov, A. K. Vakar, A. F. Gutsol, V. K. Givotov, E. G. Krasheninnikov, and M. F. Krotov, “Plasmachemical methods of energy carrier production,” *Int. J. Hydrogen Energy*, vol. 10, no. 7, pp. 475–477, 1985.

[76] BOC Edwards, *XDS Dry Pump*, 2007.

[77] Stanford Research Systems, *Models RGA100, RGA200, and RGA300 Residual Gas Analyzer*, 2005.

[78] BOC Edwards, *E2M28 and E2M30 Rotary Vacuum Pumps*, 2003.

[79] I. Langmuir, “The interaction of electron and positive ion space charges in cathode sheaths,” *Physical Review*, vol. 33, no. 6, pp. 954–989, 1929.

[80] I. L. H. M. Mott-Smith, “The theory of collectors in gaseous discharges,” *Physical Review*, vol. 28, no. 4, pp. 727–763, 1926.

[81] F. F. Chen, “Electric probes,” in *Plasma Diagnostic Techniques* (R. H. Huddlestone and S. L. Leonard, eds.), pp. 113–200, Academic Press, 1965.

[82] I. H. Hutchinson, *Principles of Plasma Diagnostics*. Cambridge University Press, 2002.

[83] J. Laframboise and L. Parker, “Probe design for the orbit-limited current collection,” *Journal of Fluids*, vol. 6, pp. 629–636, 1973.

[84] J. Laframboise and J. Rubinstein, “Theory of a cylindrical probe in a collisionless magnetoplasma,” *Journal of Fluids*, vol. 19, pp. 1900–1908, 1976.

[85] I. D. Sudit and R. C. Woods, “A study of the accuracy of various langmuir probe theories,” *J. Appl. Phys.*, vol. 76, no. 8, pp. 4487–4497, 1994.

[86] National Institute of Standards and Technology - Physics Laboratory, “Nist atomic spectra database.” `http://physics.nist.gov/PhysRefData/ASD/lines_form.html`, July 2009.

[87] R. Stocker, “Excitation-emission-spectra.” `http://www.combustion-database.com/AES/aes_home.htm`, July 2009. Institute of Thermal Power Systems.

[88] Y. Itikawa and N. Mason, “Cross sections for electron collisions with water molecules,” *J. Phys. Chem. Ref. Data*, vol. 34, no. 1, pp. 1–22, 2005.

[89] Y. Lee, J. Oh, and J. Shin, “Dynamic model and electrical characteristics for rf-biased electronegative plasma sheath,” *IEEE Transaction on Plasma Science*, vol. 30, no. 3, pp. 1320–1330, 2002.

[90] D. S. Stafford, “O2(1delta) production in he/o2 mixtures in flowing low pressure plasmas,” *Journal of Applied Physics*, vol. 96, no. 5, pp. 2451–2465, 2004.

[91] D. S. Stafford, “Modeling of singlet-delta oxygen yields in flowing electric discharges,” Master’s thesis, University of Illinois at Urbana-Champaign, 2004.

[92] R. Dorai and M. J. Kushner, “Consequences of propene and propane on plasma remediation of nox,” *Journal of Applied Physics*, vol. 88, no. 6, pp. 3739–3747, 2000.

[93] R. Dorai, “Modeling of plasma remediation of nox using global kinetic models accounting for hydrocarbons,” Master’s thesis, University of Illinois at Urbana-Champaign, 2000.

[94] P. N. Brown, G. D. Byrne, and A. C. Hindmarsh, “Vode, a variable-coefficient ode solver,” *SIAM Journal on Scientific and Statistical Computing*, vol. 10, no. 5, pp. 1038–1051, 1989.

[95] L. Spencer, S. V. T. Nguyen, and A. D. Gallimore, “Dissociation of co_2 in a radio-frequency plasma source,” in *CAPPSA 2009 - 4th International Congress on Cold Atmospheric Pressure Plasmas: Sources and Applications*, (Ghent, Belgium), June 2009.